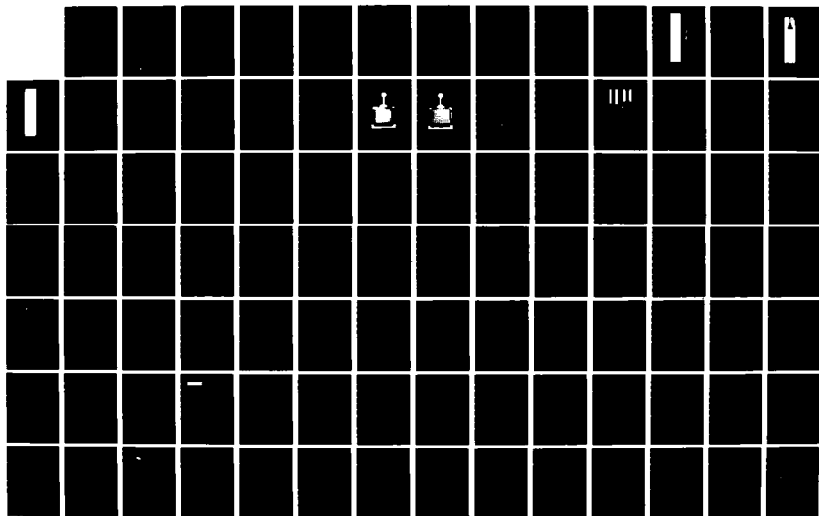
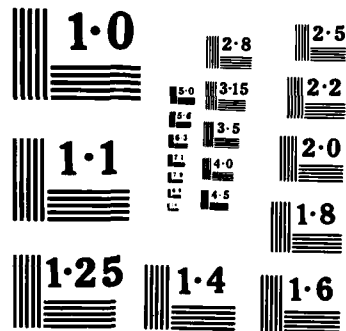


**UNCLASSIFIED**

DAJA45-83-C-0054

NL





NATIONAL BUREAU OF STANDARDS  
MICROCOPY RESOLUTION TEST CHART

AD-A158 313

DTIC FILE COPY

AD

INVESTIGATIONS AND COMPARISONS OF NEW TYPES OF  
MILLIMETRE-WAVE PLANAR ARRAYS USING MICROSTRIP  
AND DIELECTRIC STRUCTURES.

Final Technical Report

by

J.R. JAMES and C.M. HALL

April 1985

United States Army

RESEARCH & STANDARDIZATION GROUP (EUROPE)

London England

CONTRACT NUMBER .DAJA.45-83-C-0054..

Royal Military College of Science  
Shrivenham, Nr Swindon, England

Approved for Public Release; distribution unlimited

DTIC  
ELECTE  
AUG 21 1985  
E

852-8 20 057

UNCLASSIFIED

SECURITY CLASSIFICATION OF THIS PAGE (When Data Entered)

REPORT DOCUMENTATION PAGE		READ INSTRUCTIONS BEFORE COMPLETING FORM
1. REPORT NUMBER	2. GOVT ACCESSION NO.	RECIPIENT'S CATALOG NUMBER
4. TITLE (and Subtitle) Investigations and Comparisons of New Types of Millimetre-Wave Planar Arrays Using Microstrip and Dielectric Structures		5. TYPE OF REPORT & PERIOD COVERED Final Technical Report Aug 83 - Apr 85
7. AUTHOR(s)  J.R. James and C.M. Hall		6. PERFORMING ORG. REPORT NUMBER
9. PERFORMING ORGANIZATION NAME AND ADDRESS Royal Military College of Science Shrivenham, Nr Swindon, England		8. CONTRACT OR GRANT NUMBER(s) DAJA45-83-C-0054
11. CONTROLLING OFFICE NAME AND ADDRESS USARDSG-UK Box 65, FPO NY 09510-1500		10. PROGRAM ELEMENT, PROJECT, TASK AREA & WORK UNIT NUMBERS 61102A 1T161102BH57-03
14. MONITORING AGENCY NAME & ADDRESS (If different from Controlling Office)		12. REPORT DATE February 1985
		13. NUMBER OF PAGE: 111
		15. SECURITY CLASS. (of this report) Unclassified
		15a. DECLASSIFICATION DOWNGRADING SCHEDULE
16. DISTRIBUTION STATEMENT (of this Report) Approved for Public Release; distribution unlimited		
17. DISTRIBUTION STATEMENT (of the abstract entered in Block 20, if different from Report)		
18. SUPPLEMENTARY NOTES		
19. KEY WORDS (Continue on reverse side if necessary and identify by block number)  Millimetre-wave antennas, Planar antenna arrays, Microstrip		
20. ABSTRACT (Continue on reverse side if necessary and identify by block number) The combination of microstrip and dielectric structures has been found to offer possibilities for improvements upon purely microstrip planar antennas which are limited particularly at millimetre wavelengths by dissipative losses and by radiation from complex feed networks. All the structures considered retain microstrip radiating elements and in the first case a dielectric feed line was used in a travelling-wave array which enabled feeder losses to be reduced. However field compatibility problems with all-dielectric		

DD FORM 1 JAN 73 1473

EDITION OF 1 NOV 65 IS OBSOLETE

UNCLASSIFIED

SECURITY CLASSIFICATION OF THIS PAGE (When Data Entered)

UNCLASSIFIED

SECURITY CLASSIFICATION OF THIS PAGE (When Data Entered)

20. Contd.

feeder networks caused excessive radiation losses. The same compatibility problems with conventional rectangular waveguide prevent the full potential of this array from being realized but is still preferable to all-dielectric feeder networks.

The retention of microstrip feed networks allows much improved integration possibilities and this was realized by combining a microstrip patch with an overlaid dielectric sphere. When combined in the form of parallel connected arrays with a sparse feed network the result is much lower levels of corrupting radiation than have previously been achieved and the provision of space within the aperture for electronic components such as phase shifters. Used in arrays or as single element antennas this novel structure allows the designer additional design freedom.

In separate studies the issues of bandwidth and cross-polar radiation are investigated and combined with the above lead to useful conclusions and recommendations on the possibilities for integrated millimetre-wave antennas.

UNCLASSIFIED

SECURITY CLASSIFICATION OF THIS PAGE (When Data Entered)

# TABLE OF CONTENTS

PAGE

1	INTRODUCTION	1
2	COMPARISON OF MICROSTRIP AND DIELECTRIC STRUCTURES	2
2.1	Comparison of performance	2
2.2	Launchers compatible with dielectric circuits	5
2.3	Hybrid antenna arrays	5
2.4	Dielectric corporate feeds for dielectric arrays	5
2.5	Summary comments	8
3	BANDWIDTH LIMITATIONS	8
4	MICROSTRIP ANTENNA CROSS-POLARIZATION PROPERTIES	10
5	ARRAYS AND SMALL ANTENNAS USING A DIELECTRIC SPHERE/MICROSTRIP PATCH RADIATING ELEMENT	11
5.1	Basic Action	11
5.2	Small antennas using a single sphere/patch element	12
5.3	Patch arrays using overlaid arrays of spherical lenses	12
5.4	Electronically controlled arrays	18
5.5	Summary comments	19
6	CONCLUSIONS AND RECOMMENDATIONS	19
6.1	Conclusions	19
6.2	Recommendations	22
7	REFERENCES	22
8	APPENDICES	24



Accession Bar	
NTIS	X
DTIC	
Unannounced	
Justified	
By _____	
Distribution /	
Availability Codes	
Dist	Avail and/or Special
A-1	

LIST OF FIGURES	PAGE
1 40-wavelength hybrid array operating at 90 GHz.	4
2 40 x 10 element hybrid array with a slab guide transition region.	6
3 40 x 10-element hybrid array with a narrow transition region	7
4 256-element patch array with overlaid spheres ( $d = D = 0.95\lambda_0$ ) operating at 90 GHz.	13
5 64-element patch array with overlaid spheres ( $d = D = 1.90 \lambda_0$ ) operating at 90 GHz.	14
6 Measured E- and H-plane radiation patterns of the 256-element patch array, with overlaid spheres, at 90 GHz.	15
<p>Substrate thickness = 0.127 mm,  Substrate dielectric constant = 2.3,</p> <p>Sphere dielectric constant = 2.2 - 2.5,  <math>d = D = 3.18 \text{ mm} = 0.95\lambda_0</math>.  Co-polar theory omitted for clarity.</p>	
7 Measured E- and H-plane radiation patterns of the 64-element patch array, with overlaid spheres at 90 GHz.	16
<p>Substrate thickness = 0.127 mm,  Substrate dielectric constant = 2.3,  Sphere dielectric constant = 2.2 - 2.5,  <math>d = D = 6.35 \text{ mm} = 1.9\lambda_0</math>.</p>	
8 Comparison between the measured spurious and cross-polar levels of the 256 and 64-element arrays, operating at 90 GHz.	17

	LIST OF APPENDICES	PAGE
8.1	Loss comparisons of insular guide and microstrip millimetre antenna array feeders <sup>4</sup> and Conformal planar millimetre arrays - a systems appraisal <sup>8</sup> .	24
8.2	Dielectric corporate feeds for arrays employing dielectric waveguides.	51
8.2.1	A short review of power division and spreading in planar optical waveguides.	52
8.2.2	Summary of experimental results on dielectric corporate feeds for a two-dimensional insular guide-array.	65
8.3	Millimetre-wave hybrid dielectric-microstrip antenna array. <sup>7</sup>	58
8.4	A review of microstrip radiating element bandwidth.	69
8.4.1	Bandwidth criteria.	70
8.4.2	Rectangular elements.	71
8.4.3	Disc and annular-ring elements.	72
8.4.4	Elements employing parasitic elements of horizontal and lateral extent.	74
8.4.5	References relevant to microstrip bandwidth survey.	86
8.5	Cross-polarization behaviour of series-fed microstrip linear arrays <sup>15</sup> .	88
8.6	Microstrip patch arrays with spherical dielectric overlays, <sup>9</sup> Microstrip planar arrays with dielectric sphere overlays <sup>18</sup> , and Dielectric sphere reflector feed with microstrip excitation <sup>19</sup> .	100



## 1 INTRODUCTION

The attractive nature of microstrip as an electromagnetic radiating structure<sup>1</sup> needs no introduction and research effort continues to increase in this topic area. There are indications however that for microwave applications the topic is reaching some degree of maturity whereby the fundamental action is reasonably well understood and further advances will reside mainly in design innovation. At millimetre wavelengths the situation is somewhat different for several reasons. For instance, the applications are less numerous and mainly directed towards highly specified military requirements; also millimetre-wave technology is less well developed than its microwave counterparts as manufacturing and material tolerances are generally more critical. There is thus much scope for fundamental research into ways of utilizing printed structures at millimetres.

In a recent research programme<sup>2,3</sup> we concentrated our efforts on fundamental design constraints on printed antennas at millimetres and loss mechanisms were identified as a major obstacle. Ways of introducing dielectric feeders to reduce the loss were proposed and a new type of hybrid microstrip/dielectric antenna array was evolved. Manufacturing tolerances were seen as a problem requiring new initiatives but were not in themselves formidable, and are subdivided between design and fundamental investigations.

Several recommendations arising from the above mentioned research formed the basis of this present programme reported here<sup>10-14</sup> and the details are as follows:

### Mainly design:

- (a) Create new antenna designs for elements on aircraft and small vehicles.
- (b) Investigate any new substrate materials, launcher arrangements, and tolerance effects.

### Fundamental investigations into parameters affecting system performance:

- (c) Investigate the problems of cross-polarization and determine the most feasible way to eliminate or reduce it.
- (d) Investigate bandwidth limitations in microstrip antennas and optimal conditions.
- (e) Compare the performance and limitations of

microstrip and dielectric-type structures at millimetres.

The comparison of microstrip and dielectric structures, Item (e), is presented in section 2.1 - 2.3, and provides valuable information about making a choice in an overall systems sense. Item (b) follows on naturally and is given in section 2.4.

Sections 3 and 4 deal with the bandwidth and cross-polarization investigations, Items (d) and (c) respectively, and the findings here have general applications both at microwave and millimetres.

The main design work Item (a) continues with ways of combining dielectric and microstrip structures and exploits the lens effect using spherical dielectric overlays. This is presented in section 5, and we have included work which is being completed during the compilation of this report.

In the interests of clarity and conciseness we have reproduced the publications arising as appendices, thus enabling the main body of the report to be presented as a succinct review of achievements, problematical issues, conclusions and recommendations.

## 2. COMPARISON OF MICROSTRIP AND DIELECTRIC STRUCTURES

### 2.1 Comparison of performance

The details of this particular study have been published<sup>4</sup> and are reproduced in Appendix 8.1. We are concerned here with the types of millimetre-wave antenna array structures that can be deployed conformal with the vehicle skin, with the minimum disturbance to the latter at low cost.

The vehicle is likely to arise from an aerospace requirement or possibly involve small projectiles or guided munitions. Microstrip antennas seemed ideally suited but dielectric waveguide radiators appeared initially to offer considerable advantages in view of their much lower loss. In retrospect, this latter advantage is seen to be outweighed by launching losses.

There are several facets to this investigation as follows:

- (a) An inspection<sup>5</sup> of radiation patterns shows that microstrip antennas offer superior pattern characteristic control to that obtained from travelling-wave dielectric waveguide linear arrays. (Pattern control embraces both co- and cross-polarization characteristics.) This situation parallels that observed when comparing wire Yagi antennas

with conventional dielectric rod antennas where the former gave better control for the same weight and size of structure. Intuitively this is reasonable in that conducting surfaces totally reflect incident waves whereas dielectric interfaces only partially reflect and can sustain guided waves along the interface creating a complicated situation regarding polarization. There is some evidence that more reasonable pattern control results for very long dielectric structures approaching 40 to 50 guide-wavelengths long.

- (b) That microstrip lines have significant loss is well known, but the attitude has also persisted that dielectric lines have negligible loss. A detailed analysis of the latter has shown that the dissipative losses can indeed be very small. However, when forming feeders for antenna applications the lines must be compatible with antenna design requirements and the losses can be somewhat larger. Even so the dielectric radiating structure still has a significant advantage over microstrip linear arrays when comparing dissipative losses.
- (c) Millimetre-wave radars and sensors, etc, commonly employ conventional metal rectangular waveguides and antennas generally have to be compatible with this requirement. The transition between the transmitting/receiving equipment and the antenna is termed the 'launcher' and for microstrip antennas the latter can take a variety of forms. For dielectric structures such as image and insular guide the launcher is essentially a microwave horn. Analysis and experiment has established that dielectric antenna launchers have a significantly higher loss than microstrip antenna launchers. The launcher loss is brought about by direct leakage of radiation from the launcher aperture which also has a corrupting effect both on the co- and cross-polarization properties of the antenna pattern.
- (d) It is seen that the higher launching loss of dielectric antennas tends to negate their lower dissipative losses and a series of curves have been presented depicting overall antenna loss as a function of antenna length. This comparison has been in the nature of a systems comparison with microstrip giving less overall loss for antennas up to about 20 feeder-wavelengths long. Dielectric travelling-wave antennas do not show a clear advantage unless the antenna length exceeds some 40 feeder wavelengths long. When this is compounded with the inferior pattern characteristics stated in Item (a),

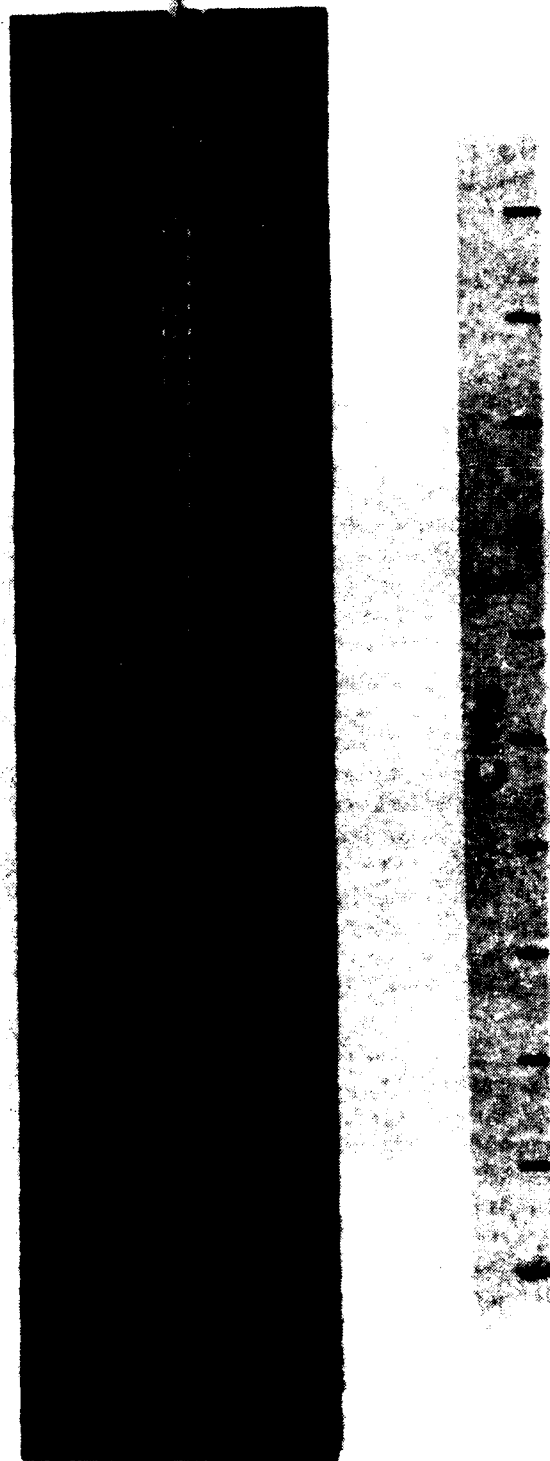


FIGURE 1. 40-Wavelength hybrid array operating at 90 GHz.

it follows that dielectric antennas need to be very long before a clear cut advantage over microstrip radiators is achieved.

## 2.2 Launchers compatible with dielectric circuits

It is evident from paragraph (c), section 2.1, that no significant launching loss would be incurred if the dielectric antenna was connected directly to transmitting/receiver circuits which embodied similar dielectric lines. This needs qualifying in the sense that the feeder line requirement for circuits may differ from that for antenna action and some tapered or abrupt transition may still be required. Even so, the point is established that dielectric antennas require compatible dielectric receiver/transmitter circuits to bring out their advantages. Unfortunately, dielectric circuits have remained essentially a research idea that has yet to come into fruition due to the problem of embedding components in a dielectric line.

## 2.3 Hybrid antenna arrays

A compromise is suggested whereby the microstrip feeder, which is the main source of loss in a linear microstrip array, is removed and replaced with a dielectric insular guide feeder, Fig. 1. The microstrip antenna patches proximity couple to this feeder and the overall effect is that the superior microstrip antenna pattern control over dielectric antennas is achieved with the lower feeder losses. This hybrid antenna was reported on in the previous research programme and we present, in Appendix 8.3, the full paper<sup>7</sup> giving analytical details and results. This antenna is clearly more complicated to manufacture but its main drawback is that the higher launcher loss persists when connected to other than a similar dielectric waveguide and for connection to rectangular metal waveguide it has no overall advantage over microstrip antennas.

## 2.4 Dielectric corporate feeds for dielectric arrays

We have taken the view that dielectric millimetre-wave circuits may well prove to be viable in which case we considered it appropriate to examine the problem of connecting a two-dimensional array to a dielectric feed circuit. Microstrip antennas can be fitted with a two-dimensional array to a dielectric feed circuit. This problem has much in common with the techniques used in planar optical integrated circuitry and is briefly reviewed in Appendix 8.2.1. It was seen that optical circuits require dimensions of the

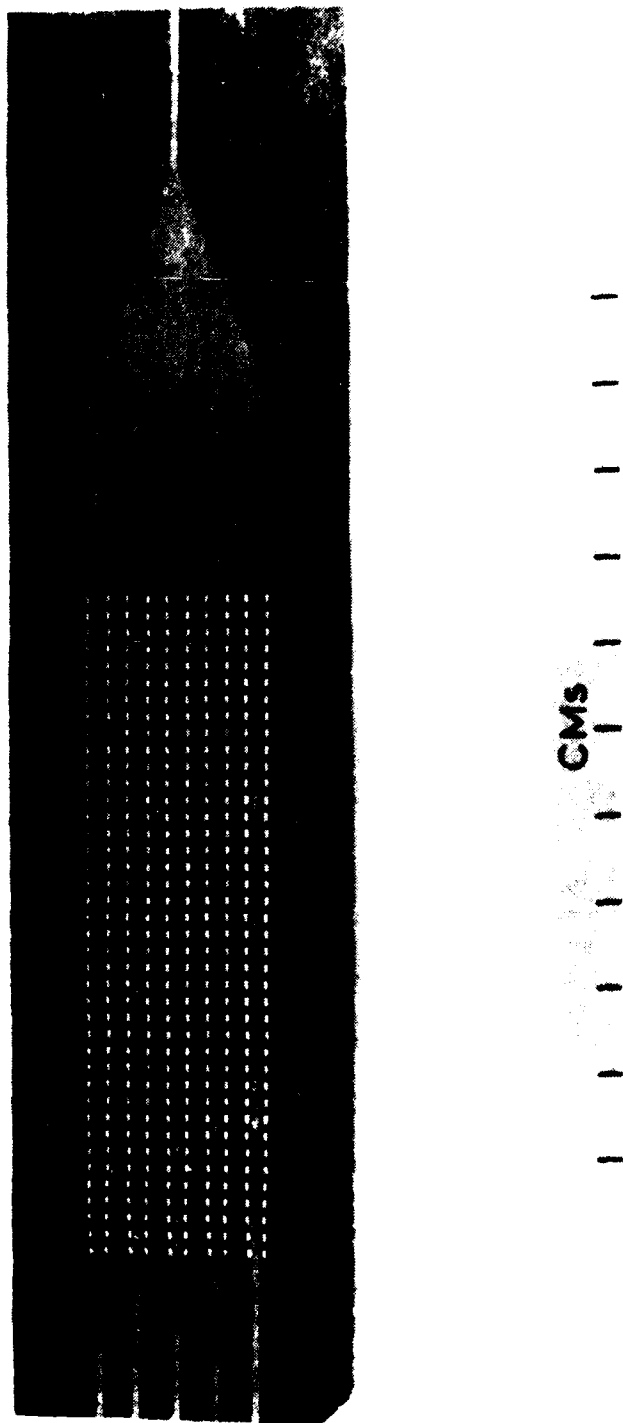


FIGURE 2. 40 x 10 element hybrid array with a slab guide transition region.

conventional rectangular waveguide. If a waveguide launching medium is retained dielectric-based arrays are preferable to purely microstrip arrays for feeder length greater than about 40 wavelengths. Microstrip travelling-arrays are preferable for lengths less than about 20 wavelengths. The breakpoint between purely microstrip and dielectric-based arrays is difficult to judge exactly without reference to a specific application.

The possibilities for compatible all-dielectric corporate feed structures for two-dimensional travelling-wave arrays have been examined and it was found that they will exhibit severe radiation losses in the limited space available in real systems. Power splitting and spreading in dielectric guides requires impractically long lengths, and over these distances, dissipative loss in the dielectric guide alone would rule out their use.

In view of the problems encountered with all-dielectric feeds, waveguide horn launchers seem more attractive for use with large dielectric-based array antennas connected to conventional waveguide or E-plane circuitry both of which are reasonably mature.

(b) A novel structure has been found which combines a dielectric sphere (or truncated sphere) with a microstrip patch radiating element. In common with the travelling wave array this basic element retains microstrip to effectively control the radiation and combines this with a spherical dielectric lens which enhances the single element gain without additional microstrip feeder lines and patch radiating elements.

Used singly, this element has possibilities as a single patch low to medium gain antenna which can be easily integrated with external circuitry and offers continuous design control over gain and beamwidth. To date, gains up to about 16.5 dBi have been realised while still retaining a uniform aperture distribution with sphere diameters less than about 3 wavelengths (substrate dielectric constant = 2.3, sphere dielectric constant = 2.2 - 2.5).

Patch arrays using this element combine microstrip feed lines and radiating elements with dielectric lenses in contact with the array. Low feed radiation loss has been achieved as this type of element allows a minimum, sparse, feed network to be used at the expense of some increase in depth. Spurious and cross-polar levels of less than about 20 dB have been achieved using an interelement spacing of 1.9 wavelengths at 90 GHz. Grating lobes and side-lobes are commensurate with a uniform aperture distribution and the combination with a simple feed network offers good prospects for antennas with sidelobes and grating lobes at less than -20 dB with corrupting radiation below this level.

Patch arrays with sparse feed networks, as well as having the above mentioned advantages, would allow the integration of phase shifting

to a microstrip patch without overlaid lenses. Typically, the scanning loss for a sphere of diameter  $D = d = 0.95\lambda_0$  would be -0.4 dB at  $\pm 10$  degrees and 3.4 dB at  $\pm 30$  degrees, while for a sphere of diameter  $D = d = 2.6\lambda_0$  the scanning loss would be -3.0 dB at  $\pm 10$  degrees, compared to -0.2 dB at  $\pm 10$  degrees and -2.0 dB at  $\pm 30$  degrees for a single microstrip patch (substrate dielectric constant = 2.3). It would remain for the system designer to establish what scanning loss could be tolerated.

## 5.5 Summary comments

This work has demonstrated the advantages of the dielectric sphere/microstrip patch element as a useful low to medium gain antenna of simple design, offering continuous control of gain up to a limit of about 16.5 dBi at a sphere diameter of about 3 free-space wavelengths. It has been demonstrated to be useful as a reflector feed antenna and would also find application in the simplification of millimetre-wave antenna integration.

The use of sparse feed networks, made possible using this novel element, allows a lower level of spurious and cross-polarized radiation to be obtained from parallel-fed patch arrays. This low level of corrupting radiation was evident in the good agreement between calculation and measurements.

Integrated phased arrays have been proposed as an important area where sparse feed networks may find use. Such arrays could employ a matrix of spheres moulded in a single sheet, and accurately fixed to the circuit beneath, to additionally provide a robust cover.

## 6 CONCLUSIONS AND RECOMMENDATIONS

### 6.1 Conclusions

(a) In this investigation a new hybrid antenna structure has been proposed in which the advantages of dielectric and metallic elements have been combined to achieve effective radiation control and power feeding. The first of these solutions is a hybrid planar travelling-wave array using a low loss insular guide feeder and microstrip radiating elements. The second solution retains microstrip for power feeding and radiation control but combines this with a spherical dielectric lens structure in direct contact with the microstrip patch radiating elements. These two types will be treated separately.

The insular guide travelling-wave array of the type proposed offers higher efficiency than an equivalent microstrip array. This advantage is generally negated for dielectric-based arrays due to the high radiation losses encountered at the junction with



lower levels of corrupting radiation to be achieved due to the possibilities for large inter-element spacings and hence sparse feed networks.

Three large millimetre-wave patch arrays have been built with the same aperture size and inter-element spacings of  $d = D = 0.95 \lambda_0$ ,  $1.90 \lambda_0$  and  $3.80 \lambda_0$  containing 256, 64 and 16 spheres and radiating elements respectively. The third array with the largest spacing had a severe grating lobe limitation and the lowest gain of 24 dBi. Figures 4 and 5 show the first two arrays.

The gain of the 64-element array was measured at 26 dBi compared to 27 dBi for the 256-element array (due to greater deviation from a uniform aperture distribution) but the most important difference lay in the lower levels of spurious and cross-polar radiation achieved by the 64-element array summarized in Figure 8 and includes the contribution from the unscreened launcher which is evident on the positive side of the H-plane radiation patterns in Figures 6 and 7.

Figures 6 and 7 show the radiation patterns of the two antennas in Figures 4 and 5 and from Figure 7 it can be seen that grating lobes are evident and at a level expected from a uniform array. The calculated radiation patterns are in good agreement with measurements and also indicated that grating lobe levels vary very little for inter-element spacings up to  $d = D \approx 3\lambda_0$ . Prospects are good for achieving sidelobes, grating lobes, spurious and cross-polar radiation, all at levels less than -20 dB.

#### 5.4 Electronically controlled arrays

There is an electronic scanning requirement for millimetre-wave integrated phased arrays, and attempts in the past to construct such arrays have required the use of quarter-wave shorted patch radiating elements in order to make room for phase shifters<sup>20</sup> while still maintaining good grating-lobe suppression. Quarter-wave patches are not practical for millimetre-wave integrated antennas and so the new element is proposed as a possible solution.

Sparse feed networks can provide the space needed for phase shifters (or other electronic circuits) and their associated control lines. Inter-element spacings would be dictated by the number of bits required for each phase shifter and the space needed to run control lines to the middle of the array. These requirements would need to be balanced against some increase in scanning loss dependent upon sphere size.

Such phased arrays would suffer from higher scanning loss compared

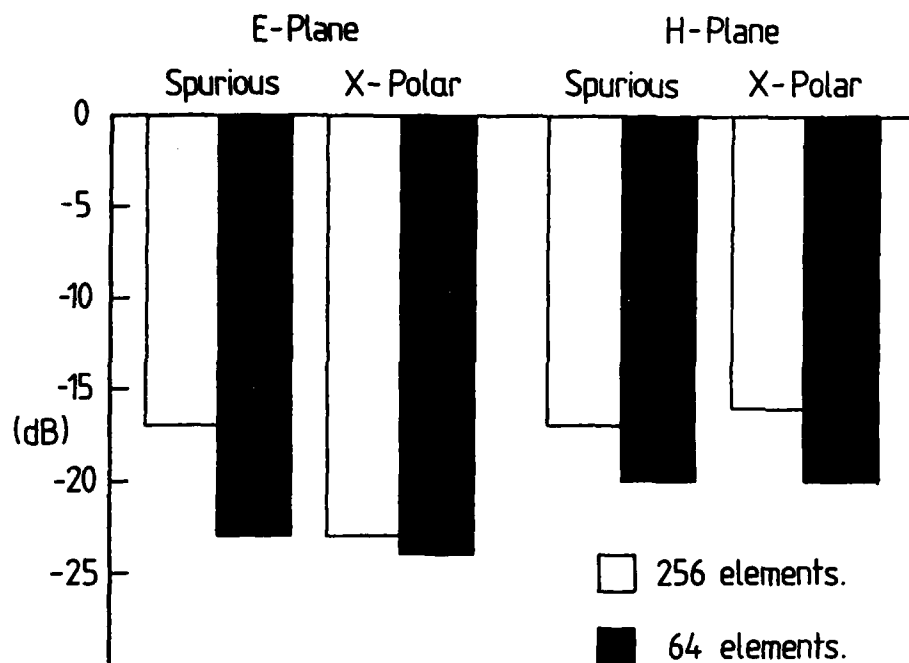


FIGURE 8. Comparison between the measured spurious and cross-polar levels of the 256 and 64 element arrays, operating at 90 GHz.

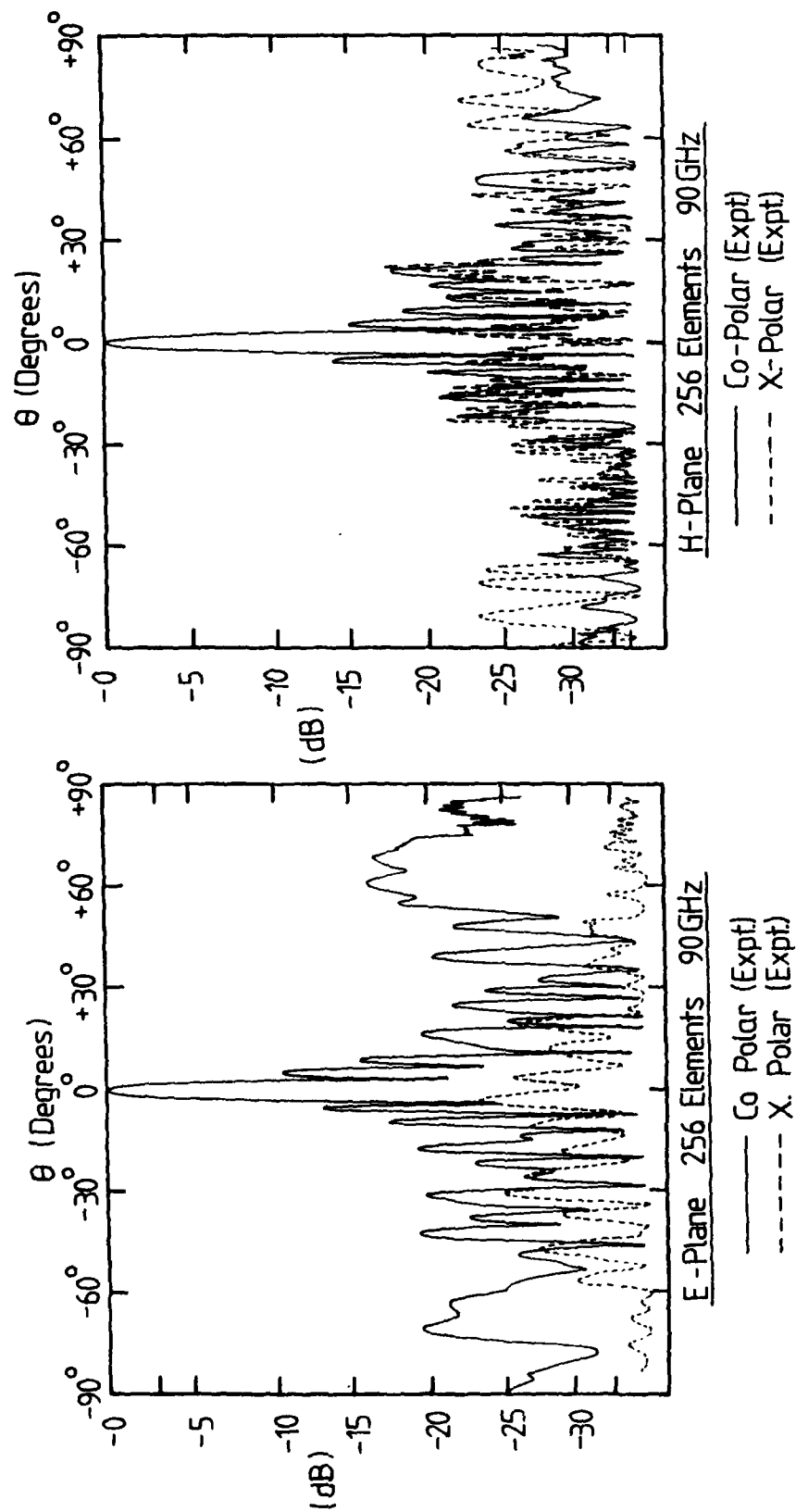


FIGURE 7. Measured E and H-plane radiation patterns of the 64 element patch array, with overlaid spheres at 90 GHz. Substrate thickness = 0.127 mm, Substrate diel. const. = 2.3, Sphere diel. const. = 2.2 - 2.5,  $d = D = 6.35 \text{ mm} = 1.9 \lambda_0$ .

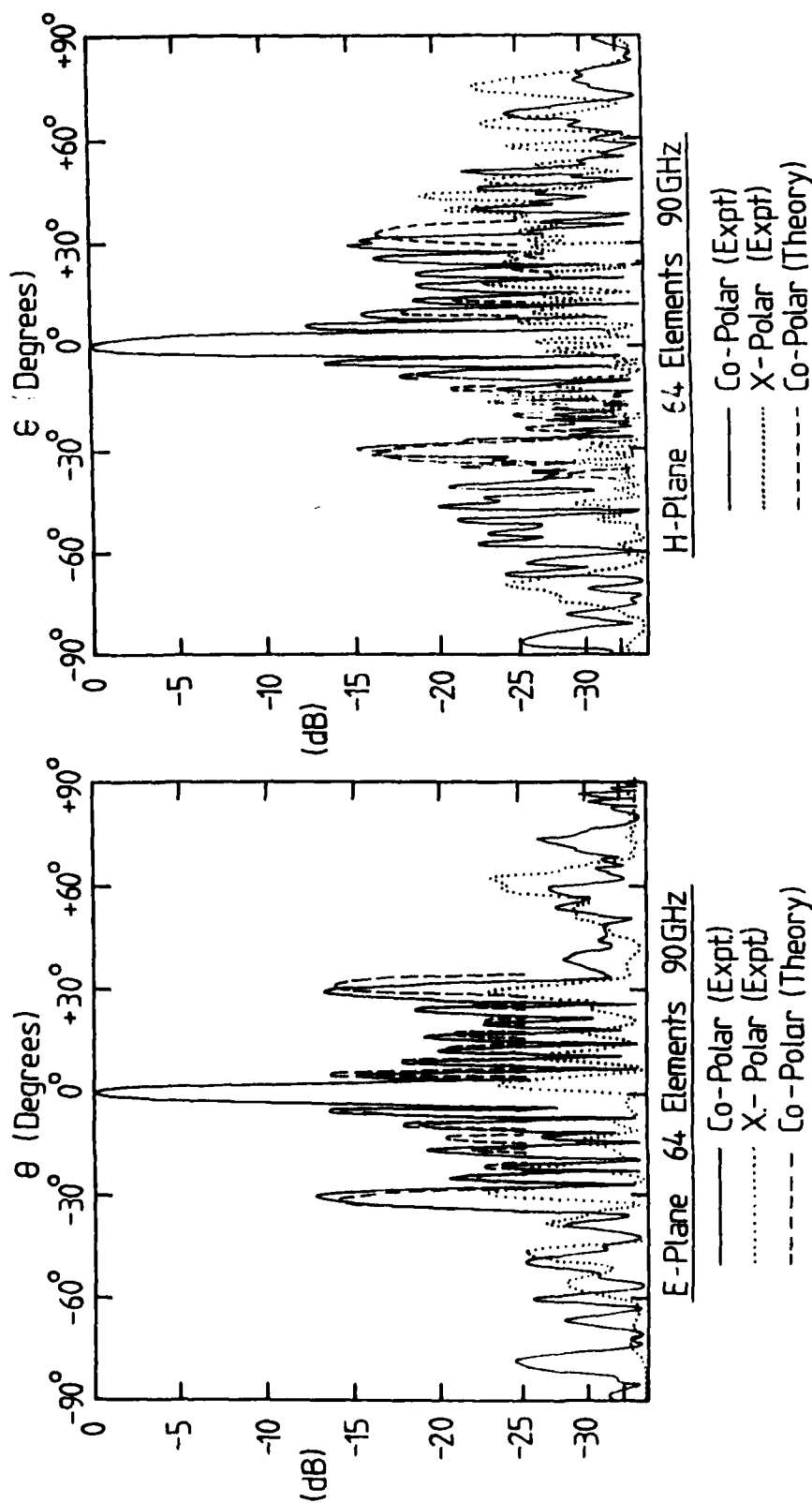
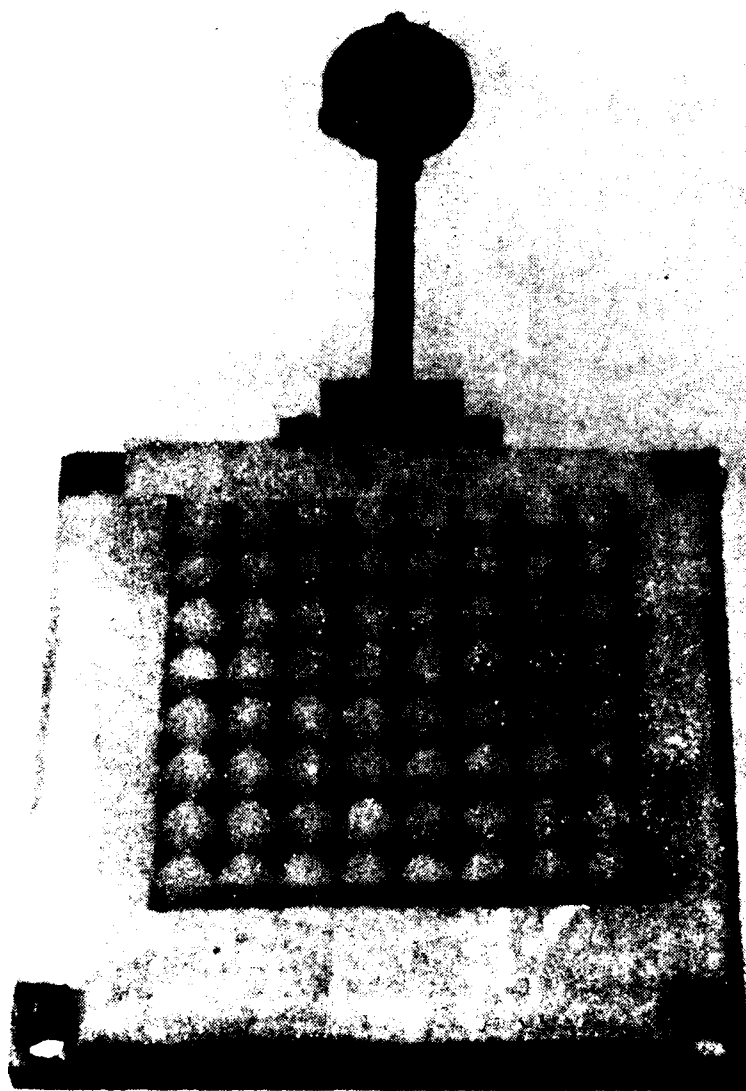
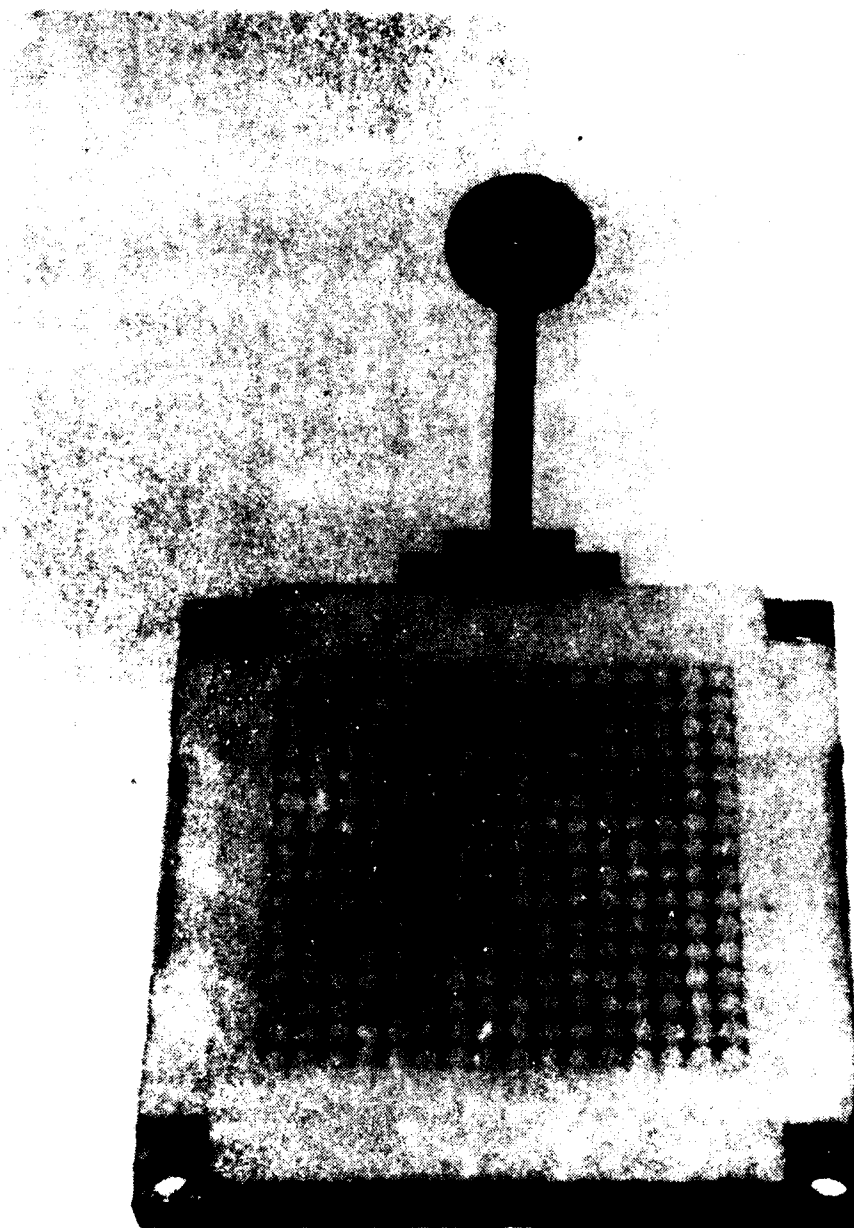


FIGURE 6. Measured E and H-plane radiation patterns for the 256 element patch array, with overlaid spheres at 90 GHz. Substrate thickness = 0.127 mm, Substrate diel. const. = 2.3, Sphere diel. const. = 2.2 - 2.5,  $d = D = 3.18 \text{ mm} \approx 0.95 \lambda_0$ . Co-polar theory omitted for clarity.



CMs

FIGURE 5. 64 element patch array with overlaid spheres  
( $d = D = 1.90 \lambda_0$ ) operating at 90 GHz.



CMs

FIGURE 4. 256 element patch array with overlaid spheres  
( $d = D = 0.95 \lambda_0$ ) operating at 90 GHz.

fields. Our analysis models the patch as two magnetic, Hertzian, dipoles at opposite ends of the patch and the far-field radiation patterns are calculated from a set of fictitious sources on the surface of the sphere by the Equivalence principle. Array patterns are obtained from the multiplication of the element pattern and the appropriate array factor.

Initial measurements showed that the gain of a PTFE sphere in combination with a square microstrip patch (on a substrate of dielectric constant  $\epsilon_r = 2.3$ ) levels off at about 16.5 dBi. Dielectric loss has not been found to be the major limiting factor. Instead, we have found that aperture fields generated by the lens deviate from a uniform distribution for sphere diameters greater than about three free-space wavelengths. This shows up in high side-lobe levels and a rapid levelling in the gain above this diameter.

#### 5.2 Small antennas using a single sphere/patch element.

The single/patch radiating element makes possible a range of low to medium gain antennas the basic limitations of which have already been outlined. These would be useful in applications where some increase in depth would not present serious problems.

This element has already been applied to the design of a single element reflector feed antenna<sup>19</sup>. Choice of an appropriate sphere diameter and truncated height gave continuous design control over the antenna beamwidth and provided a simple method of optimizing reflector illumination with minimum design effort. Measurements showed that the input bandwidth was increased and the input match generally improved when the sphere was put in contact with a microstrip patch.

At millimetres, this element offers a simple technique for integrating small antenna elements without the complications of feed networks; only a single microstrip element and a truncated sphere is required. Possibilities exist for switched or simultaneous beam operation.

#### 5.3 Patch arrays using overlaid arrays of spherical lenses.

Much of the work on the use of these elements has concentrated upon their use in arrays. Conventional patch arrays suffer from high feed radiation losses which corrupt antenna radiation patterns in the form of spurious and cross-polar radiation and this may be reduced by increasing the overall feed impedance level. The use of spherical lenses has enabled

cross-polarization and design options, at least to a first order. For greater accuracy the particular structure of interest must be studied in detail and this has been done for the comb array by carrying out a modal analysis to obtain the local current distribution.

(d) Summary comment.

Increased radiation from a section of a linear antenna generally creates increased cross-polarization. Longer arrays with a more gradual leakage of radiation are thus improved in this respect. Feed cross-polarized radiation remains difficult, and generally requires absorbent material to remove it. Surface-waves and their cross-polarized radiation can be reduced by the use of lower permittivity substrates which are feasible at microwave but not at millimetres. Generally co- and cross-polarization have to be traded for one another and some specifications may not be viable. No one type of radiating structure appears to have an outstanding advantage although it will be possible in some cases to cancel out some cross-polarized radiation by choice of structure symmetry.

5      ARRAYS AND SMALL ANTENNAS USING A DIELECTRIC  
         SPHERE/MICROSTRIP PATCH RADIATING ELEMENT

The salient problem that has emerged from this work is that of unwanted radiation from feed structures and any modification that reduces the effects of this would be an advance. In section 2, we saw that feed radiation is the main obstacle in the way of planar integrated dielectric array realization. Consequently we have been led to retain metallic feed structures and to combine them with some form of lens structure while still maintaining a basically planar form. We have been able to realise this by combining microstrip radiating elements with spherical dielectric lenses<sup>9</sup>.

Previous workers have considered the problem of combining spherical and non-spherical dielectric lenses with waveguide apertures<sup>15</sup> and recently a resonant hemispherical antenna<sup>17</sup> has been reported. Our present work is novel in that the lens is placed in direct contact with a microstrip patch in the form of an overlay and published papers are reproduced in Appendix 8.6.

5.1      Basic action

Unlike lens antennas with waveguide apertures, the combination of a lens with a microstrip patch cannot be easily modelled using the modal method, based on spherical-wave functions, because of the highly complex nature of microstrip patch near



literature, much of which does not put sufficient emphasis on the radiation pattern quality and its variation with frequency. Our own work on  $TM_{11}$ , probe fed disc elements has exposed high levels of H-plane cross-polar radiation which can only be reduced by thinning the substrate and/or increasing its dielectric constant. It is obvious here that the H-plane cross-polarization is an important bandwidth criteria that must be traded for bandwidth.

#### 4. MICROSTRIP ANTENNA CROSS-POLARIZATION PROPERTIES

With the maturity of microstrip antennas attention has been focussed on their cross-polarization characteristics. A patch element such as a disc or rectangular element would seem to be relatively easy to assess but in our experience, radiation from the feed probe or coupler dominates and takes charge of the lower level of cross-polarization and is more difficult to assess analytically.

The corrupting effect of the feed mechanism is seen<sup>6</sup> to reduce when the feeder is coupled to the patch remotely using a non-contacting overlay technique. The pattern performance of a microstrip patch, and large arrays of the latter, is thus a function of the design innovation.

With travelling-wave arrays the situation is different in that the feed is integral with the radiating elements and the designer has essentially two degrees of freedom when creating the topology of the microstrip conductor. A study has been completed on the cross-polarization behaviour of series-fed travelling-wave microstrip linear arrays and the published paper<sup>15</sup> is reproduced in Appendix 8.5. The results here are applicable at microwave and millimetre wavelengths and the principal findings are as follows.

(a) Sources of cross-polarization.

The linear array is approximated by magnetic line currents which can be represented as discrete dipole sources from which the co- and cross-polarized fields can be derived once the type of antenna is known. Other sources include radiation from feeds, terminations and substrate surface-waves, and usable expressions are given for these.

(b) First order geometric constraints.

It is seen that microstrip antennas have two degrees of freedom in geometry and that, within a given space, the degree of coupling to co-polar radiation must be traded for cross-polarized radiation. A way of assessing arrays on this basis is presented and applied to several types such as the serpent, triangle rampart, chain, Franklin antennas, etc.

(c) Application to comb line.

It is considered that the above assessment will evaluate the

Square, rectangular and disc elements are well known and their bandwidth is simply controlled by the substrate thickness, substrate dielectric constant and, in the case of the rectangular patch elements, by the width-to-length ratio. Even-mode annular ring elements constitute an interesting class of elements but there is little evidence that they are better than a rectangular element which would occupy less space for a similar bandwidth and is easier to model.

Of particular relevance to millimetre wavelengths is the use of very thick substrates supporting a number of surface-wave modes generated by patch or thin dipole elements. Coupling to surface-wave modes has the effect of lowering the radiation Q and the efficiency of radiating elements. However, we regard surface-waves as a source of uncontrolled radiation which could cause strong radiation from the substrate edges and substantial interference with integrated circuit elements. Theoretical analysis of the thick substrate has shown that large bandwidths are available (up to 50% in the case of thin dipole elements on Gallium Arsenide) but a proper evaluation of this technique needs practical results and radiation patterns.

With regard to millimetre-wave integrated antenna elements, square rectangular and disc antennas would seem to be best suited to most applications. The annular ring antenna, although novel, does not appear to have much to recommend it outside some special conformal applications, as a wide rectangular patch antenna would offer similar bandwidths, more efficient use of space and greater simplicity. Parasitic antennas would be difficult to realise but we feel that the prospects are good for lateral parasitic antennas proposed by Kumar and Gupta providing a co-planar feed line can be connected to the driven element. Vertical parasitic elements should be possible if great care is taken over tolerance control and would offer wide bandwidth for minimum substrate area. In general, these parasitic antennas are best suited for non-critical applications where a high degree of radiation control is not required as in the case of expendable jammers.

A judgement cannot be made on the bandwidth and practical limitation of placing patches and dipole elements on thick substrates of high dielectric constant until results appear on their practical realization. Such results would probably serve to highlight the problem of cross-polar and surface-wave generation associated with greater radiating element volumes. There is a strong relationship between antenna volume and bandwidth with lateral parasitic elements offering a higher degree of radiation control at the expense of greater complexity.

A dearth of experimental and theoretical results exists in the

order of many hundreds of wavelengths; such dimensions are totally out of the question at millimetre wavelengths.

A series of experiments on a series of short feeds are reported upon in the Appendix 8.2.2 and the two which were initially considered most promising are shown in Figures 2 and 3. The measured efficiencies of these feeds were estimated to be less than 2% in both cases, but we feel that this could be raised to about 10% if the entire array and feed structure were made as a single piece. These experiments have failed to reveal any practical arrangements for short feeds, but we believe that somewhat higher efficiencies could be achieved with much longer transition regions.

However, the losses incurred with a long transition would need to be balanced against those of a shorter microstrip or waveguide feed.

Purely on the basis of dissipative loss, there would be little point in making dielectric feed three times longer than a microstrip feed if the dielectric loss is one third that of microstrip.

In view of the negative results, only an outline mention of the various ideas and experiment has been given, but the outcome is nevertheless of great importance because it casts doubt over the feasibility of creating an integrated assembly of antenna and circuits comprised entirely of dielectric circuits. Looking to the future, the problem of feeding two-dimensional dielectric arrays may have its solution in circuitry. The dielectric feed could be dispensed with if each array and its associated circuitry (such as phase shifters) could be fed by separate phase-locked oscillators.

## 2.5 Summary comment

Contrary to ideas and attitudes which have persisted for many years, the millimetre microstrip antenna array shows considerable overall advantage over other types of dielectric radiators when evaluated in a system sense; that is with due consideration to the connection of the array to the rest of the equipment and the degree to which the radiation pattern can be controlled.

## 3. BANDWIDTH LIMITATIONS

A considerable amount of literature exists on the topic of microstrip radiating element bandwidth, and this is reviewed in Appendix 8.4. In most cases reported, bandwidth is treated as a side issue, involving the measurement of input impedance, but there is an emerging realisation that perhaps this is not the most important criteria and that there may be other criteria that impose more strict limitations on bandwidth.

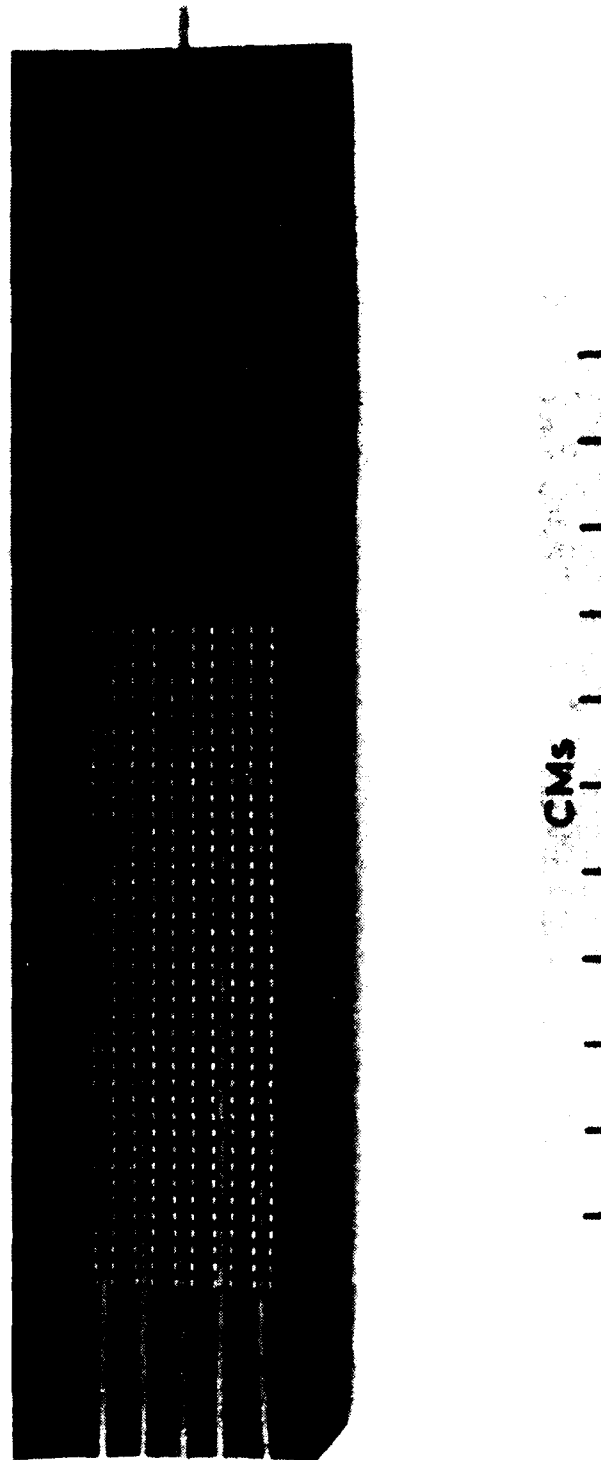


FIGURE 3. 40 x 10 element hybrid array with a narrow transition region.

circuitry and their associated circuitry. The use of dielectric spheres would cause an increase in scanning loss compared to a conventional microstrip patch and hemispherical coverage would not be possible. However, we do not consider that scanning loss would be a major problem for large millimetre phased arrays as most seeker applications would require maximum scan angles between 10 and 30 degrees. A judgement on tolerable scanning loss would have to be made by the system designer.

(c) Cross-polar radiation levels in travelling-wave arrays are a function of the degree to which the feed guide is perturbed and the radiation forced from the array by the radiating elements and also upon the thickness of the substrate or radiating element volume; this is true for both dielectric and microstrip arrays. Generally speaking lower cross-polar operation requires low coupling to a large number of radiating elements on a thin substrate and this implies some trade-off between cross-polar radiation and bandwidth. The 40-wavelength long hybrid array described in this report achieved a maximum level of -25 dB which is equal to the best achieved from a microstrip comb array. Launcher radiation is an additional source of radiation pattern corruption in travelling-wave arrays and here there is a link between the previously mentioned field compatibility problems (which are more serious in dielectric arrays) and launcher efficiency.

Certain feeder configurations can have low cross-polar radiation due to field cancellation from symmetrical halves of the feed structure. This is true of the H-plane cross-polar from parallel-fed patch array feed networks where radiation from right angled microstrip bands cancels in the far-field at boresight. However a low level of feed radiation is still essential in order to achieve a low level of corrupting radiation throughout an entire hemisphere. This has been achieved in this work using sparse feed networks.

(d) A survey of various microstrip radiating elements has shown bandwidth to be a function of antenna volume. Large increases in volume necessary for high bandwidth have been achieved using parasitic elements which impart a closely spaced multifrequency response to the antenna. These parasitic antennas have achieved their practical bandwidth limit without a severe diminishing return on design effort. Lateral parasitic antennas have achieved their increased volume by occupying a large substrate area on a thin substrate and as such they would have low coupling to surface-waves and cross-polar radiation at the expense of a variation of the effective antenna phase centre with frequency. Vertical parasitic antennas here achieved the greatest bandwidth using increased depth which is associated with high cross-polar levels. Generally these antennas are suited for less critical applications. At millimetre

wavelengths the basic square, rectangular and disc radiating elements are sufficient for most purposes. With a 2:1 width to length ratio rectangular resonators equal the bandwidth available from annular ring elements while occupying less substrate area. The annular ring antenna is interesting but would be of little use outside some specialized applications.

There has been much recent interest in the use of Gallium Arsenide as a substrate material for monolithic millimetre-wave circuits and the properties of thin dipoles and microstrip patches on thick substrates have been theoretically studied. On Gallium Arsenide, a maximum bandwidth of 50% has been predicted for thin dipole elements at 30% for patch elements for substrate thicknesses of about 0.1 and 0.2 wavelengths respectively. This has implications for cross-polar radiation, mutual coupling levels and radiation from the substrate edges but as yet there has been no evidence in the literature on the practical application of this technique and its effects.

An emerging issue in the judgement of bandwidth is the link between element volume and cross-polar radiation control. This is an important issue at millimetres and requires an experimental treatment especially on Gallium Arsenide and on soft substrates which are less problematical.

## 6.2 Recommendations

(1) When designing and optimizing a millimetre-wave microstrip antenna as regards cross-polar radiation, bandwidth and losses (both dissipative and radiative) due consideration should be given to the results of the studies carried out in this report which when compounded will allow the best trade-off between the various parameters to be made to suit the required specification.

(2) The investigations contained in this report offer considerable scope for future research on the integration of the antenna with its associated circuitry.

## 7 REFERENCES

- 1 James, J.R., Hall, P.S. and Wood, C., 'Microstrip antenna theory and design', Peter Perigrinus Ltd, London, England, 1981 (IEE, London).
- 2 US Army/Airforce Contract DAJA 37-80-C-0183.
- 3 James, J.R. and Hall, C.M., 'Investigations of new concepts for designing millimetre-wave antennas', Final Tech. Report, Contract No. DAJA 37-80-C-0183, Sept. 1983.

- 4 John, G. and James, J.R. 'Loss comparisons of insular guide and microstrip millimetre antenna array feeders', Electromagnetics, Vol. 3, p217-237,
- 5 Henderson, A. and James, J.R., 'A Survey of millimetre wavelength planar arrays for military applications' Radio and Electronics, Vol. 52, p543-550, Nov./Dec. 1982.
- 6 Hall, P.S. and Prior, C.J., 'Microstrip array for reflector feed applications', Proc. 14th European Microwave Conf., Liege, Belgium p631-636, Sept. 1984.
- 7 James, J.R., John G. and Hall, C.M., 'Millimetre-wave hybrid dielectric-microstrip antenna array', Proc. IEE, Pt.-H, Vol. 131, No.6, p341-350, Dec. 1984.
- 8 James, J.R., Henderson, A. Hall, C.M. and Andrasic, G., 'Conformal planar millimetre arrays - a systems appraisal', Proc. 1984 Military Microwaves Conf., p518-521, 24-26 Oct. 1984.
- 9 Hall, C.M., James, J.R. and Andrasic, G., 'Microstrip patch arrays with spherical dielectric overlays'. Proc. Int. Conf. on Antennas and Propag., 1985, p89-93, Warwick Univ., England. p. 16-19 April, 1985.
- 10 James, J.R. and Hall, C.M., 'Investigations and comparisons of new types of millimetre-wave planar arrays using microstrip and dielectric structures', 1st periodic report, 1st Sept. 1983 to 1st Dec. 1983, Contract No. DAJA 45-83-C-0054.
- 11 op. cit., 2nd periodic report, 25 Nov 1983 to 24 Feb 1984.
- 12 op. cit., 3rd periodic report, 25 Feb 1984 to 24 May 1984.
- 13 op. cit., 4th periodic report, 24 May 1984 to 24 Aug 1984.
- 14 op. cit., 5th periodic report, 25 Aug 1984 to 30 Nov 1984.
- 15 Hall, P.S. and James, J.R., 'Cross-polarization behaviour of series-fed microstrip linear arrays', Proc. IEE, Pt-H, Vol. 131, No.4, p247-257, August 1984.
- 16 Croswell, W.F., Chatterjee, J.S., Mason, V.B. and Tai, C.T., 'Aperture excited dielectric antennas', NASA Tech. Note, TN D-7342, 1974.
- 17 McAllister, M.W. and Long, S.A., 'Resonant hemispherical dielectric antenna', Electron. Lett. (GB), Vol.20, No.16, p657-659, 2 August 1984.
- 18 Hall, C.M., Andrasic, G. and James, J.R. 'Microstrip planar arrays with dielectric sphere overlays', Electron. Lett. (GB), Vol.21, No.8, p356-357, April 1985.
- 19 James, J.R., Hall, C.M., Hall, P.S. and Prior, C.J., 'Dielectric sphere reflector feed with microstrip excitation' to be presented at the International Symposium on Antennas and Propagation, Japan, 1985.
- 20 Mailloux, R.J., 'Phased array theory and technology', Proc IEEE, Vol. 70, No.3, p246-291, 1982.

## Appendix 8.1

Loss Comparisons of Insular Guide and Microstrip Millimetre  
Antenna Array Feeders <sup>4</sup>.

and

Conformal Planar Millimetre Arrays - A Systems Appraisal <sup>8</sup>.



# LOSS COMPARISONS OF INSULAR GUIDE AND MICROSTRIP MILLIMETRE ANTENNA ARRAY FEEDERS

G. John and J. R. James, *Department of Electrical and Electronic  
Engineering, Royal Military College of Science, Shrivenham,  
Swindon, Wilts SN6 8LA, U.K.*

## ABSTRACT

The use of printed antenna techniques at millimetre wavelengths to create planar linear travelling wave antennas is commonly considered to be inhibited by the microstrip feeder loss and the alternate use of low loss dielectric feeders is thus attractive. In this investigation an additional source of unwanted loss is considered and a complete assessment, more favourable to microstrip, emerges. The fields of an insular guide antenna feeder are computed by a mode matching method to provide accurate data for the guide attenuation and also the launcher radiation loss when the insular guide is connected to a conventional rectangular metal waveguide using a horn launcher transition. This latter analysis is based both on a chopped surface wave distribution method and an alternative variational method. Similar loss data is computed for microstrip antenna feeders using existing theories and some experimental data presented. A comparison of total unwanted losses for both types of feeders establishes that microstrip is advantageous for feeder lengths up to about 20 wavelengths long, the precise condition for equality depending on many other factors which are discussed. If however the feeders are assumed to be fully integrated with an electrically compatible guide structure in the receiver or transmitter to remove the source of launcher radiation loss, insular guide is distinctly advantageous, thus highlighting the need for new technological developments in integrated millimetre linear antenna systems.

## 1. INTRODUCTION

The development of military systems operating at millimetre wavelengths has created a demand for planar millimetre wave antenna arrays which can be made conformal with a vehicle surface, are low cost, light weight and can be readily interfaced with the electronic equipment. Typically the array will have three main functions as sketched in Fig 1a where the launcher section connects the antenna structure to the transmitter and/or receiver. A two-dimensional array would additionally require a corporate feed system. Ideally the array will be integrated with the electronic circuitry to obviate the need for a launcher but this is at present generally out of the question in view of the universal use of conventional metal waveguides in millimetre wavelength equipment.

The use of microstrip (Fig 1b) to create radiating structures<sup>1</sup> is becoming well-established at microwave frequencies and fits the above requirements for

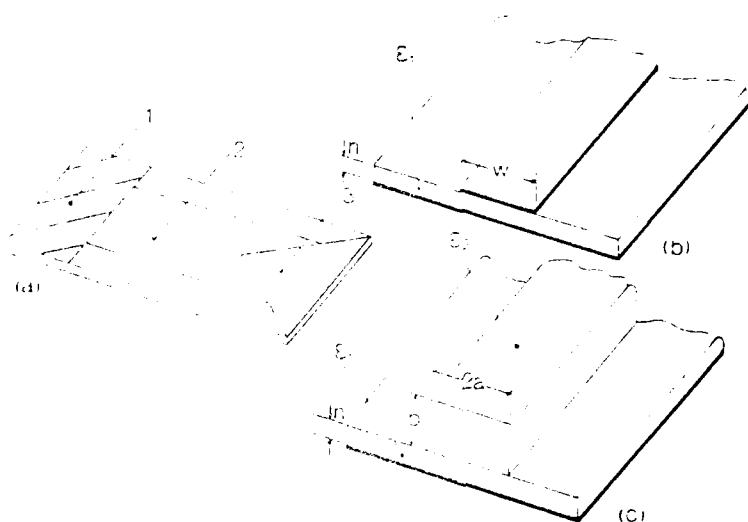


Fig 1.

(a) low profile planar array functions

1. Launcher; 2. Linear radiating system; 3. Load for travelling wave action

(b) Microstrip line

(c) Insular guide ( $h > 0$ ,  $\epsilon_2 > \epsilon_1$ ): Image guide ( $h = 0$ )

conformality etc, but the intrinsic loss is often considered to be unacceptably high at millimetre wavelengths where transmitting power is at a premium. For instance, a microstrip array with a directional gain of 28dB (based on integration of the radiation pattern) is likely to have an internal power loss of typically 50% thus reducing the antenna system gain to 25dB. It was no doubt for these reasons that considerable attention has been focussed on the possibility of creating millimetre wave antennas from dielectric waveguides<sup>3</sup> with their inherent low loss, as an alternative to microstrip.

Many types of ground plane mounted dielectric waveguides have been conceived which lend themselves to conformal array applications<sup>4</sup>. Although their radiation pattern performance does not appear to equate with that which is realisable with microstrip arrays, it is tacitly assumed that the use of dielectric structures will lead to a lower antenna system loss. More recently it was pointed out<sup>5</sup> that the benefits associated with the use of dielectric structures could be negated by the launcher loss and in such circumstances the use of microstrip may be advantageous. The purpose of this paper is to quantify the antenna system loss for planar millimetre wave arrays comprised of microstrip and dielectric guides to extract design recommendations. For the purposes of comparison we concentrate on one of the lowest loss dielectric guides, the insular guide<sup>6</sup> Fig 1c.

The criterion for power loss along a one-dimensional linear antenna array is taken with good approximation as the loss per guide wavelength along the feeder. Radiation elements attached either to the feeder or embraced within it as discontinuities<sup>4</sup> are generally efficient radiators and the main power loss

is in the feeder. Emphasis is thus placed on the accurate calculation of the attenuation and phase constants section 2 and new results are presented for the insular guide. The assessment of launcher radiation loss presents both analytical and measurement problems, particularly for the insular guide where two methods of estimating the loss are outlined in section 3. System loss comparisons are made in section 4 and presented in the context of prevailing system requirements and likely future developments, prior to the conclusion section 5.

## 2. TRANSMISSION LINE CHARACTERISTICS

### 2.1. Insular guide field representations

Adequate formulas already exist<sup>7</sup> for characterising microstrip but insular guide is a more complicated structure and methods of analysing it are less well established. We obtain accurate field representations for use in section 3 and match Cartesian wavefunctions at the various insular guide cross-sectional boundaries. This approach is referred to here as Theory A and is similar to that used in the calculation of image lines<sup>8</sup> and inverted strip dielectric waveguide<sup>9</sup>. A simplified form of Theory A, referred to here as Theory B, is also evaluated and is useful for calculating the dominant phase constant behaviour in insular guide.

In theory A, the cross section of the insular guide Fig 2 is subdivided vertically into subregions  $X_1$  and  $X_2$  where  $0 \leq X_1 \leq a$ ,  $a \leq X_2 \leq \infty$  and symmetry about  $x = 0$  is invoked. The method requires the presence of a fictitious upper ground plane at  $y = (h + b + l)$  and the space between these ground planes is subdivided horizontally into subregions  $Y_1$ ,  $Y_2$  and  $Y_3$  where  $0 \leq Y_1 \leq h$ ,  $h \leq Y_2 \leq (h + b)$ ,  $(h + b) \leq Y_3 \leq (h + b + l)$ . The harmonic behaviour in the  $z$  direction is taken as  $\exp(-j\beta z)$  where  $\beta$  is the phase constant. The form of the  $E_y$  field component is:

$$E_y = \sum_{m=1}^M (\bar{k}_{xm}^2 + \beta^2) \frac{\cos(k_{xm} x) \cdot \bar{\epsilon}_m^e(y)}{\cos(k_{xm} a) \cdot \epsilon(y)} A_m; \text{ region } X_1$$

$$= \sum_{m=1}^N (\bar{k}_{xm}^2 + \beta^2) \exp[-j\bar{k}_{xm}(x - a)] \frac{\bar{\epsilon}_m^{-e}(y)}{\epsilon(y)} C_m; \text{ region } X_2 \quad (1)$$

where  $\bar{\epsilon}_m^e(y)$ ,  $\epsilon(y)$  and  $k_{xm}$  are defined in the appendix section 7.1 and the bar denotes region  $X_2$ ;  $A_m$  and  $C_m$  are unknown coefficients. The  $\bar{\epsilon}_m^e(y)$  functions are defined by the Transverse Magnetic mode behaviour of a three layered stratified model with a relative permittivity in regions  $Y_1$ ,  $Y_2$  and  $Y_3$  of  $\epsilon_1$ ,  $\epsilon_2$  and  $\epsilon_3$  respectively. The resulting transcendental equation defines  $k_{y1m}$ ,  $k_{y2m}$  and  $k_{y3m}$  and hence  $(k_{xm}^2 + \beta^2)$ .

Similarly  $\bar{\epsilon}_m^h(y)$  functions can be defined for the Transverse Electric mode behaviour in the three layered stratified model, appendix section 7.2, with wavenumbers  $k_{xm}'$ ,  $k_{y1m}'$ ,  $k_{y2m}'$  and  $k_{y3m}'$  enabling  $(k_{xm}'^2 + \beta^2)$  to be calculated. The form of  $H_y$  is:

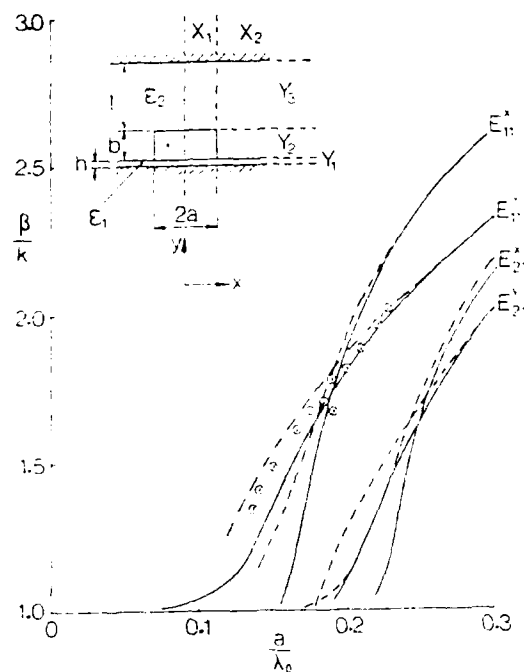


Fig 2. Insular guide mode chart

$$a = 1.58b$$

$$h = 0.242b$$

$$l = 5\lambda_0$$

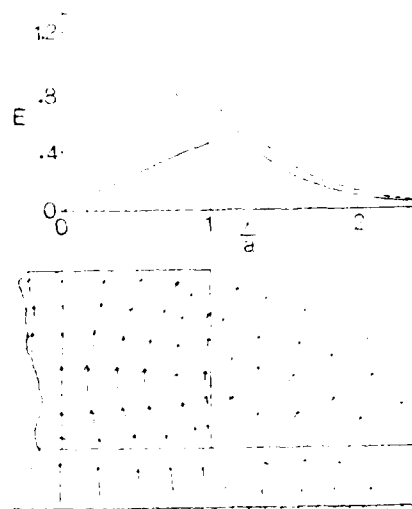
$$\epsilon_1 = 3.32$$

$$\epsilon_2 = 10$$

———— theory A

----- theory B

⊗ ⊗ ⊗ ⊗ ⊗ ⊗ Experiment  
(from 8-14 GHz)

Fig 3. Field plot of  $E_{11}^+$  mode

Field strength proportional  
to length of arrow.

E - relative value of  
electric field, computed  
for  $y = h + \frac{b}{2}$ .

————  $E_x$   
-----  $E_y$

$$\begin{aligned}
 H_y &= \sum_{m=1}^{M'} (\bar{k}_{xm}'^2 + \beta^2) \frac{\sin(\bar{k}_{xm}' x)}{\sin(\bar{k}_{xm}' a)} \bar{\phi}_m^h(y) B_m; \text{ region } X_1 \\
 &= \sum_{m=1}^{N'} (\bar{k}_{xm}'^2 + \beta^2) \exp[-j\bar{k}_{xm}' (x-a)] \bar{\phi}_m^h(y) D_m; \text{ region } X_2
 \end{aligned} \quad (2)$$

where  $B_m$  and  $D_m$  are unknown coefficients and bars denote region  $X_2$ . Similar expressions exist for  $E_x$ ,  $H_x$ ,  $E_z$  and  $H_z$  having individual terms, as in eqn (1) and (2), that by definition are continuous across the horizontal boundaries delineating regions  $Y_1$ ,  $Y_2$  and  $Y_3$ . On the vertical boundaries of regions  $X_1$  and  $X_2$ , the tangential fields are matched and orthogonality relationships invoked to yield a system of homogeneous equations from which the unknown coefficients and  $\beta$  can in principle be extracted. In reality the dimension  $l$  determines the number of modes  $M$ ,  $N$ ,  $M'$  and  $N'$  eqns (1) and (2) and hence the completeness of the field forms used in the matching and the convergence of the computation. After many trials we have compromised on  $l = 5\lambda$  throughout, where  $\lambda$  is the free space wavelength, giving  $M = N = M' = N' = 10$  and sufficient convergence of the field forms without the build up of round-off errors. The dominant behaviour is portrayed by surface wave terms in Theory A, which are evanescent in the  $y$ -direction above the dielectric slab. If these are used alone we obtain a relatively simple calculation Theory B; this is also known as 'the effective dielectric constant' method which is essentially equivalent<sup>10,9</sup> to considering only  $m = 1$  terms in eqns (1) and (2). For fields with their transverse electric components polarised in the  $y$  direction take  $M = N = 1$  and  $M' = N' = 0$ , eqns (1) and (2) yielding:

$$\begin{aligned}
 \beta^2 &= \epsilon_{e1} k^2 + \bar{k}_{x1}^2 = \epsilon_{e2} k^2 - \bar{k}_{x1}^2 \\
 \frac{\bar{k}_{x1}}{k_{x1}} &= \begin{cases} \tan(k_{x1} a); & \text{even} \\ -\cot(k_{x1} a); & \text{odd} \end{cases}
 \end{aligned} \quad (3)$$

where even and odd refer to symmetry and asymmetry of  $E_y$  about  $x = 0$ , respectively and

$$\begin{aligned}
 \epsilon_{e2} &= \epsilon_2 - \left(\frac{k_{y21}}{k}\right)^2 \\
 \epsilon_{e1} &= \epsilon_1 - \left(\frac{k_{y11}}{k}\right)^2
 \end{aligned}$$

where  $\epsilon_{e1}$  and  $\epsilon_{e2}$  are the effective dielectric constants for the  $X_2$  and  $X_1$  regions respectively. Similarly putting  $M = N = 0$  and  $M' = N' = 1$  eqns (1) and (2) yield fields with the transverse electric component polarised in the  $x$  direction.

Computed results for Theory A and Theory B together with some experimental results are given in Fig 2; we follow the conventional mode nomenclature where  $E_{pq}$  corresponds to  $p$  and  $q$  power concentrations in the  $x$  and  $y$  directions respectively. The experimental results were obtained by measurement of a standing wave pattern on the structure and lie between the computed results of the two theories. Theory B cannot model the cut-off behaviour of the modes and gives very incomplete field patterns. Field patterns obtained by Theory A, Fig 3 show evidence of the incompleteness of the matching process at the

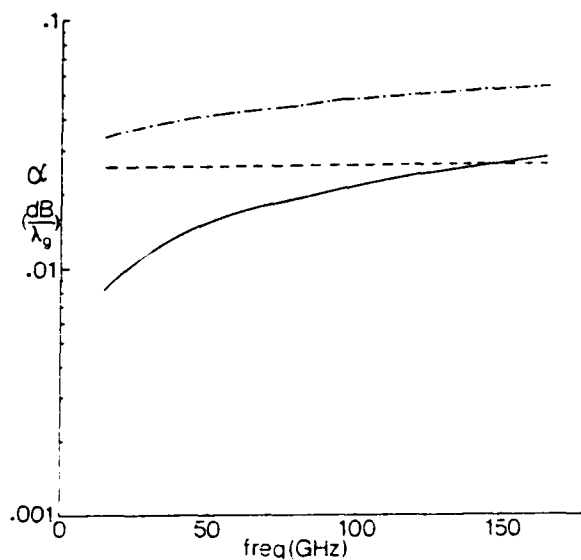


Fig 4. Insular guide losses  $E_{11}^V$  mode  
 $a = 0.14\lambda_0$  (loose binding)

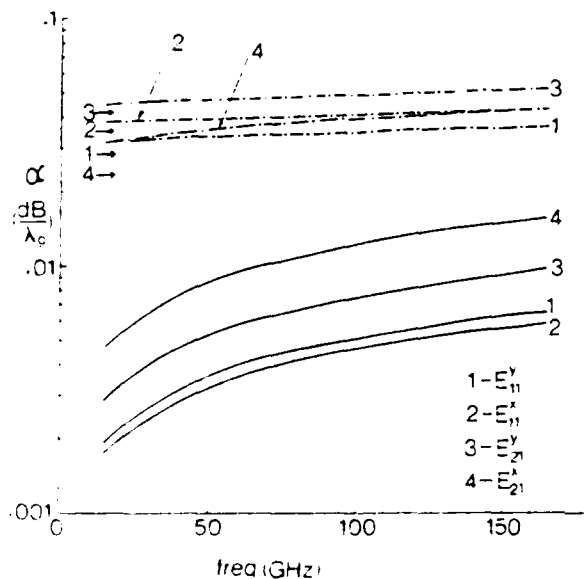


Fig 5. Insular guide losses  $E_{11}^V$  mode  
 $a = 0.25\lambda_0$  (tight binding)

For figures 4 and 5,

$$a = 1.58b$$

$$h = 0.242b$$

$$\epsilon_1 = 2.32$$

$$\epsilon_2 = 10$$

$$\tan \delta_1 = 0.001$$

$$\tan \delta_2 = 0.001$$

$$\sigma = 5.7 \times 10^7 \text{ S/m}$$

$$\text{---} \alpha_{IC}$$

$$\text{---} \alpha_{ID}$$

$$\text{---} \text{total loss } \alpha_I$$

$\alpha_{ID}$  in Fig 5 is constant  
 over frequency range, and  
 the level is indicated by  
 $\rightarrow$

vertical boundaries.

## 2.2. Loss characteristics

Previous calculations<sup>6</sup> of the loss in insular guides have been based on simplified field representations such as Theory B. Here we use the Cartesian field representations of Theory A eqns (1) and (2) for  $E_y$  and  $H_y$  with  $E_x$ ,  $H_x$ ,  $E_z$ ,  $H_z$  likewise derived from similar equations of this theory. In view of the low loss of these guides a perturbation calculation is applicable. The attenuation constant  $\alpha_I = \alpha_{IC} + \alpha_{ID}$  where  $\alpha_{IC}$  and  $\alpha_{ID}$  are the attenuation constants for the conductor loss and the dielectric loss respectively.

$$\alpha_{IC} = \frac{R_s}{4P_I} \int_{-\infty}^{\infty} [H_x H_x^* + H_z H_z^*] dx \quad (4)$$

where  $R_s = (\omega \mu_0 / 2\sigma)^{1/2}$ ,  $\sigma$  = conductivity of the ground plane, \* denotes complex conjugate,  $P_I$  = total power flowing in insular guide and the magnetic fields are evaluated only in the lower ground plane Fig 2, at  $y = 0$ .

$$\alpha_{ID} = \frac{\omega \epsilon_0}{4P_I} \int_{x=-\infty}^{\infty} \int_{y=0}^{h+b} \epsilon_r(x,y) \tan \delta(x,y) [E_y E_y^* + E_x E_x^*] dx dy$$

$$\left. \begin{aligned} \epsilon_r(x,y) &= \epsilon_1 \\ \tan \delta(x,y) &= \tan \delta_1 \end{aligned} \right\} 0 \leq y \leq h, -\infty \leq x \leq \infty$$

$$\left. \begin{aligned} \epsilon_r(x,y) &= \epsilon_2 \\ \tan \delta(x,y) &= \tan \delta_2 \end{aligned} \right\} h \leq y \leq h+b, -a \leq x \leq a \quad (5)$$

where  $\tan \delta_1$  are material loss tangents. The total power flowing in the guide is

$$P = \frac{1}{2} \text{Re.P.} \int_{x=-\infty}^{\infty} \int_{y=0}^{h+b} [E_x H_y^* - E_y H_x^*] dx dy \quad (6)$$

where the integration range embraces the six sub-crosssectional areas dictated by the boundaries of the regions  $X_1$ ,  $X_2$ ,  $Y_1$ ,  $Y_2$  and  $Y_3$ . Some computed results for eqns (4) and (5) are shown in Fig 4 for a loosely bound  $E_{11}^y$  mode and for a selection of modes with tighter binding in Fig 5. The increased conductor loss with loose binding of the  $E_{11}^y$  mode outweighs the increase in dielectric loss for tight binding and is a comparison only made possible by the use of fields of Theory A. The composition of losses differ for different modes Fig 5 but the trend shown is that the  $E_{11}^y$  mode has the lowest overall loss. Existing data<sup>6</sup> for the  $E_{11}^y$  mode shows values of  $\alpha_I$  somewhat in excess of ours and we presume that this is because simpler field forms were used. An experiment was conducted on two different lengths of insular guide set between two waveguide horn launchers of the type described in section 3. The guide was composed of material having  $\epsilon_1 = 2.32$ ,  $\epsilon_2 = 10$ ,  $\tan \delta_1 = 0.001$ ,  $\tan \delta_2 = 0.001$  and the transmission loss measured by substitution at 9.5 GHz whereby the launcher loss

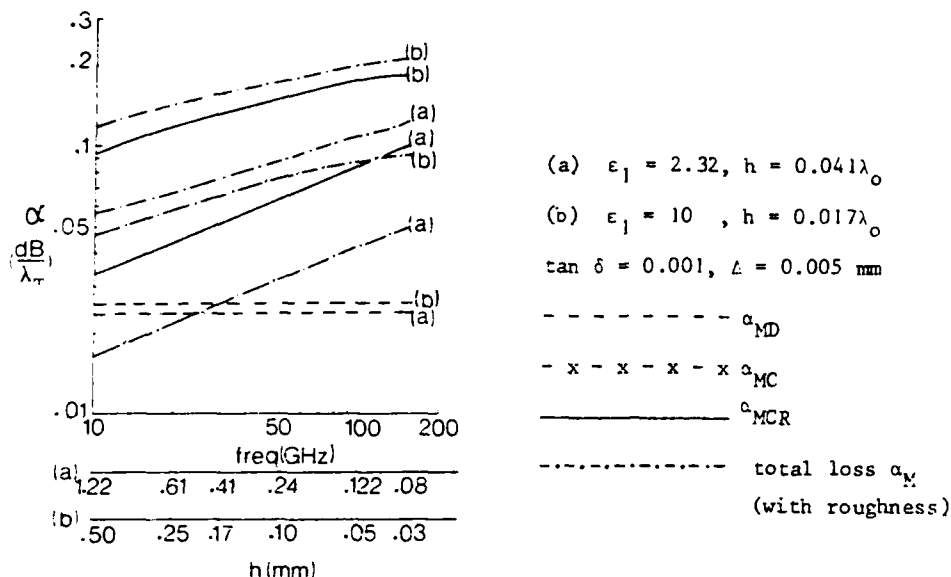


Fig 6. Microstrip losses (50C line)

was eliminated. A value of  $\alpha_T = 0.041$  dB/λ was obtained compared to the computed value of 0.036 dB/λ where λ is the wavelength in the insular guide. The low level of loss resulted in a high degree of measurement error.

For microstrip the attenuation constant  $\alpha_M = \alpha_{MC} + \alpha_{MD}$  where  $\alpha_{MC}$  and  $\alpha_{MD}$  are the attenuation constants arising from conductor and dielectric loss respectively. Little has been established about the precise loss mechanisms at millimetre wavelengths and we use loss formulas that have found wide acceptance at microwave frequencies. The formula for  $\alpha_{MD}$  is given<sup>11</sup> as:

$$\alpha_{MD} = 27.3 \frac{\epsilon_1}{\epsilon_e} \left( \frac{\epsilon_e - 1}{\epsilon_1 - 1} \right) \frac{\tan \delta}{\lambda_m} \text{ dB/m} \quad (7)$$

where  $\epsilon_1$ ,  $\epsilon_e$  and  $\tan \delta$  are the relative permittivity, the effective permittivity and loss tangent of the microstrip substrate respectively,  $\lambda_m$  is the wavelength in the microstrip. The equations of Pucel<sup>12,13</sup> are used to calculate  $\alpha_{MC}$  and some examples of losses for commonly used microstrip lines are shown in Fig 6, together with a correction<sup>14,27</sup> for surface roughness.

$$\alpha_{MCR} = \alpha_{MC} \left[ 1 + \frac{2}{\pi} \tan^{-1} 1.4 \left( \frac{\Delta}{\delta} \right)^2 \right] \text{ dB} \quad (8)$$

where  $\alpha_{MCR}$  is the corrected value of  $\alpha_{MC}$ ,  $\Delta$  = RMS surface roughness, skin



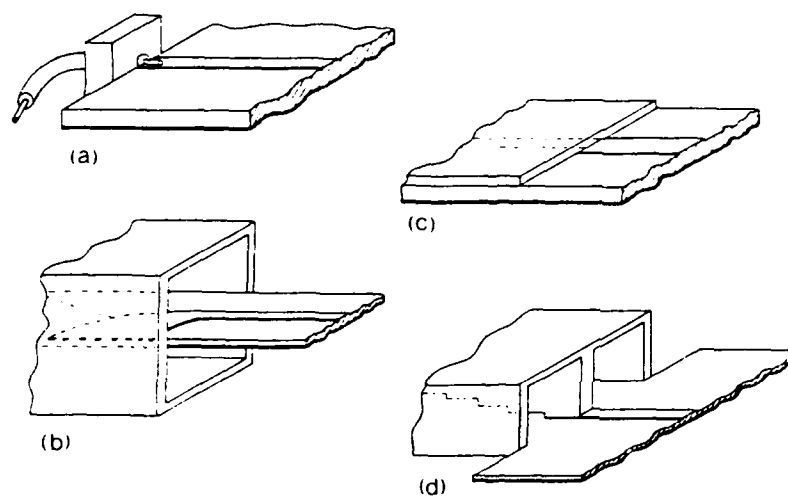


Fig. 7. Methods of launching microstrip

- (a) coax connector<sup>16</sup>      (b) waveguide E-plane launcher<sup>22</sup>  
 (c) triplate<sup>16</sup>      (d) ridge guide<sup>20</sup>

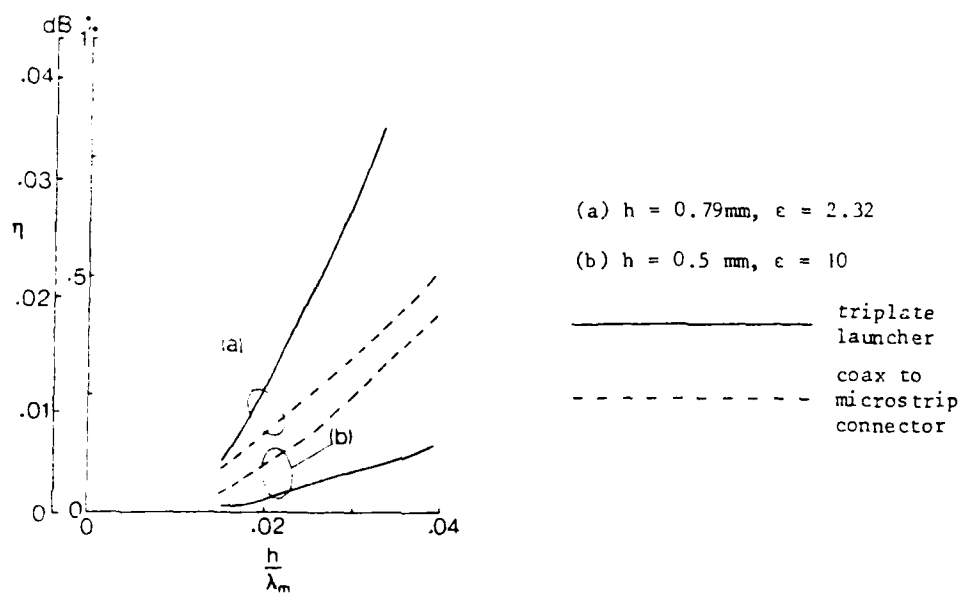


Fig 8. Computed launching power loss for microstrip (50Ω)

depth  $\delta = \frac{1}{R_s \sigma}$ . Inspection of eqn (8) shows that  $\alpha_{MC} \leq \alpha_{MCR} \leq 2\alpha_{MC}$  and for

typical  $\delta$  at millimetre wavelengths, the upper limit is reached for a very minute degree of roughness. We are not aware of evidence that eqn (8) accurately models the roughness loss at millimetres but recent measurements<sup>15</sup> have established that eqn (8) is at least a useful indication.

### 3. LAUNCHER RADIATION LOSS

Several ways of launching waves onto microstrip are illustrated in Fig 7 and computed results for the launcher radiation loss  $\eta$  from a previous analysis<sup>16</sup> are given in Fig 8. The radiation loss from the triplate launcher is of similar<sup>17</sup> order but our recent measurements<sup>15</sup> have shown that some significant insertion losses and cross-polarisation effects from the E-plane launcher Fig 7 can occur at 90 GHz. Mechanical tolerances contribute significantly to these effects.

Little has been reported about transitions for insular guides and it would appear that its connection to a conventional metal guide must involve some form of horn launcher as sketched in Fig 9. Initial experiments showed that the radiation loss for  $E_{11}^y$  launching was an order greater than that from microstrip launchers and somewhat insensitive to the horn flare angle which is contrary to expectations. Experiments on image guide launchers<sup>19</sup> report similar high levels of radiation loss.

The chopped surface wave distribution method has previously<sup>18</sup> been used to estimate launching radiation loss  $\eta$  on to an unbounded guide. We apply it to the insular guide as follows:

$$\eta = \frac{P_I - P_{I\text{horn}}}{P_I} 100\% \quad (9)$$

where  $P_I$  is defined in eqn (6) and  $P_{I\text{horn}}$  is the portion of  $P_I$  that flows in the cross sectional region  $-d \leq x \leq d$ ,  $0 \leq y \leq H$  interior to the horn mouth Fig 9.

$$P_{I\text{horn}} = \frac{1}{2} \text{Re Part} \int_{x=-d}^{x=d} \int_{y=0}^{y=H} [E_x H_y^* - E_y H_x^*] dx dy \quad (10)$$

If  $E_x$ ,  $E_y$ ,  $H_x$  and  $H_y$  eqn (10) are derived from the approximate Theory B eqn (3) for the  $E_{11}^y$  mode then excellent launching efficiency is predicted as in Fig 10 when the horn aperture height  $H$  tends to  $5\lambda_c$ . In the calculation  $2d$  is made larger than  $H$  and the latter then controls  $\eta$ .<sup>c</sup> If however the more precise insular guide fields of Theory A eqn (1) and (2) are used to derive  $E_x$ ,  $E_y$ ,  $H_x$  and  $H_y$  eqn (10) then the results, also given in Fig 10, show the insensitivity of  $\eta$  to  $H$  as observed experimentally. Since Theory A imposes an upper ground plane above the insular guide, Fig 2, at  $y = h + b + 1$ ,  $H$  cannot exceed the latter boundary. An examination of the fields of Theory A confirms the existence of fields in the vicinity of the upper ground plane as an integral part of the solution. In reality these correspond to 'box' type modes that are created when unbounded guides are shielded in a box. It is concluded that these 'box' modes exist in the horn aperture and are most significant as  $H$  increases. The 'box' modes are launched as radiation thus maintaining  $\eta$  at a higher level than that predicted by Theory B.

suitable for circuit operation are not ideal for antenna applications and vice versa; the dissipative losses differ also in the two cases. We compare microstrip linear arrays with arrays composed of the lowest loss dielectric structure, that is insular guide. In both cases  $L_g$  increases linearly with the array length and computed loss curves for microstrip and insular guide linear arrays are given in Figs 8 and 9 respectively. It is evident that the low loss of insular guide is negated by the higher launcher loss and for typical values of permittivity applicable to antenna applications, the insular guide does not show a loss advantage until the length exceeds some 20 guide wavelengths. This also applies to the hybrid antenna. However if the insular guide could be fed from a compatible dielectric structure with insignificant loss a very low overall antenna loss would be achieved.

#### CONCLUSIONS

When the above system loss comparison is compounded with the other factors such as pattern control, cross polarisation, realisation of two-dimensional array forms and corporate feeds etc, microstrip emerges as the best available technology at present, for the realisation of a wide variety of thin conformal millimetric arrays up to 140 GHz, particularly for smaller arrays. Manufacturing tolerances are a problem which, given large enough production runs, are probably amenable to micro-fabrication techniques. Dielectric structures do not appear to have advantageous properties overall and are physically incompatible with conventional waveguide equipment.

#### ACKNOWLEDGEMENTS

The work was partially sponsored by the Science and Engineering Research Council, UK and the US Army European Research Office.

#### REFERENCES

- [1] RUTLEDGE, D B et al (1984) : 'Infra-red and millimeter waves', Vol 10, Academic Press (New York)
- [2] SOLBACH, K and WOLFF, I (1981) : 2nd Int. Conf. on Antennas and Prop. (York, England), IEE Conf. Publ. No 195, 59 - 62
- [3] HENDERSON, A et al (1981) : Proc. 11th Europ. Microwave Conf. (Amsterdam) 825 - 830
- [4] INGGES, M R et al (1981) : Electron. Lett. 17 146 - 147
- [5] HALL, P S et al (1978) : Agard Conf. Proc. No 245, (Munich, Germany), 31 - 1 to 31 - 9
- [6] SANCHEZ, A and OLINER, A A (1983) : Proc. Int. URSI Symp., Spain, 397 - 400
- [7] LAMPARIELLO, P and OLINER, A A (1983) : Electron. Lett. 19, 18 - 20
- [8] ITOH, T and ADELSACK, B (1982) : IEEE Trans. AP - 30, 505 - 509
- [9] RAO, B R (1983) : Proc. Int. Symp. Digest A P (Houston, Texas), 688 - 691
- [10] WEISS, M A (1981) : IEEE Trans. AP-29, 1, 171 - 174
- [11] HORN, R E et al (1982) : IEEE Trans. MTT - 30, 816 - 820
- [12] BAHL, I J and BHARTIA, P (1980) : IEEE Trans. MTT - 28, 1205 - 1212
- [13] HENDERSON, A and JAMES J R (1982) : Radio and Electronic Engineer, Vol 52, No 11/12, 543 - 550
- [14] JOHN, G et al (1982) : Proc. 12th Europ. Microwave Conf., (Helsinki), 534 - 539.

inverted strip [4], microstrip [5], H-guide [6], groove guide [7], trough guide [8], and a precision slotted metal waveguide linear array [9]. Parallel fed radiating elements invoke feeder difficulties and examples are confined essentially to microstrip patch arrays [10]. Novel ways of creating an electronic scanning facility use semiconductor implants [11] and artificial dielectric material [12], generally at the expense of side-lobe level control and dissipation loss. A previous survey [13] concluded that dielectric radiating structures gave inferior radiation pattern control to antennas incorporating conducting radiating elements. For instance dielectric radiating structures can generate high cross polarisation levels, cannot readily be developed into two dimensional arrays and require bulky launchers to connect the array to conventional waveguide equipment. For many military applications the bandwidth of all these antenna types is adequate. It is concluded that the interest in dielectric arrays has arisen mainly from consideration of the low intrinsic loss dielectric guides in comparison to microstrip, and the most critical issue at the present time remains the question of loss and its origin.

#### ANTENNA LOSS AND ITS MINIMISATION

*Microstrip loss* - Microstrip is an important structure for conformal antennas and a study into the dissipative loss mechanism and the possibility of reducing the loss has been carried out. Loss measurements in the region 75 - 110 GHz substantiate the order of computed data corrected for surface roughness, Fig 3. Computations show that a round conductor above a ground plane has about half the loss of a flat strip but to apply this concept to microstrip would mean that its thin planar characteristics would be sacrificed. The use of foam substrates would likewise reduce the loss but are not practical propositions at millimetre wavelengths.

*Hybrid dielectric-microstrip array* - Thin printed elements have previously been incorporated in dielectric guides [3]. The hybrid antenna retains the constructional advantages of a printed substrate but embodies an integral insular guide feeder, proximity coupled at a distance  $x_0$  to the resonant patch array, Fig 4. The coupling and radiation mechanism has been analysed to yield a design process resulting in the radiation pattern, Fig 5, at 90 GHz; good cross polarisation properties are obtained and the insular guide feeder reduces the loss budget by about 3 dB. Unlike microstrip arrays, the hybrid antenna requires particular launching requirements to connect it to conventional waveguide and additional losses can be acquired.

*Launcher radiation losses* - This cause of antenna loss is particularly significant when the antenna structure is to be connected to a receiver or transmitter having a different type of feeder. Analysis [14] and measurements show that a microwave microstrip antenna has a launcher loss of less than 0.2 dB when fed from a coaxial cable. At millimetre wavelengths other types of launchers are required, Fig 6, and the loss will be somewhat higher depending on the manufacturing precision. In contrast dielectric guide structures with horn launchers suffer large launcher losses, typified by the computed result Fig 7.

#### COMPARISON OF ANTENNA SYSTEMS LOSS

Launcher radiation loss  $L_1$  and guide dissipative loss  $L_g$  are the major sources of loss in linear travelling wave arrays, Fig 1. In some cases the terminating load loss is a consideration. It is known that open guides

## CONFORMAL PLANAR MILLIMETRE ARRAYS - A SYSTEMS APPRAISAL

J R James\*, A Henderson\*, C M Hall\* and G Andrasic\*

### ABSTRACT

The use of millimetric homing devices on small projectiles and missiles will generate a requirement for large quantities of expendable thin conformal antenna arrays. At microwaves, microstrip arrays play an important role in meeting conformal antenna requirements but at millimetres, doubts have been expressed about their dissipative loss. A new type of antenna, incorporating low loss dielectric feeder lines and metal patch elements is presented here to illustrate the systems losses typically incurred at millimetres and the loss mechanisms involved. Detailed measurements and analytical results have been carried out and its performance compared with other antenna types. Finally, an overall systems appraisal of low profile millimetre antennas is made, involving aspects such as radiation pattern control and loss. It is concluded that the use of microstrip continues to be advantageous for small millimetric arrays when launcher losses and circuit compatibility are taken into account.

### INTRODUCTION

Where space, weight and manufacturing tolerances are not critically constrained, conventional horn and reflector antennas can be appropriately scaled down in size from microwave designs. Military requirements have led to the development of new types of antennas and arrays to provide electronic scanning facilities on small vehicles such as projectiles, at low cost. The 'integrated circuit' antenna concept [1] offers signal processing facilities but requires depth to accommodate the lens assemblies. On very small vehicles, thin conformal arrays with perhaps only limited scanning facilities, are demanded. There is now a multitude of thin conformal arrays composed mainly of microstrip dielectric lines reported in the literature, all with different advantages and disadvantages. In this present paper some new results are described which together with existing data enable a much clearer systems appraisal to be made of the various types of conformal planar millimetric array designs now available.

### ANTENNA TYPES

Conformal millimetric arrays for use on small projectiles, for example, are thin 'stick-on' type structures, preferably with a single feed point for ease of mounting on the host vehicle. For two-dimensional arrays some form of corporate feed is needed and to avoid feeder problems the types most commonly addressed to date have the general construction as sketched in Fig 1. Most attention has been focussed on creating novel linear travelling wave arrays from low-cost open millimetric guides where the radiating elements are generally discrete or continuous discontinuities in the guide along its length. Typical examples of novel linear array designs utilise image guide [2], Fig 2, insular guide [3],

\*Department of Electrical and Electronic Engineering, Royal Military College of Science, Shrivenham, Swindon, Wiltshire, SN6 8LA.

## 7.3. Functions used in eqn (11)

$$\begin{Bmatrix} E_r \\ H_r \end{Bmatrix} = \int_0^k \int_0^{\sqrt{k^2 - K_{y2}^2}} S(\gamma) \begin{Bmatrix} E \\ H \end{Bmatrix} dK_x dK_{y2}$$

where  $(E, H)$  are plane wave expansions for region  $Y_1$  and region  $Y_2$  Fig 2.

$$K_x^2 + K_{yi}^2 = k^2 \epsilon_i - \gamma^2$$

$$0 \leq K_x, K_{y2} \leq k \text{ for radiation}$$

$$i = 1 \quad 0 \leq y \leq h$$

$$= 2 \quad h \leq y \leq b; -a \leq x \leq a$$

$P_F$ ,  $P_S$  and  $P_r$  are functions of integrals representing power flow terms.  $S(\gamma)$  is the plane wave amplitude spectrum.

## 7. APPENDIX

## 7.1. Functions used in eqn (1)

$$e_m^e(y) = \begin{cases} \cos(k_{y1m}y), & \text{for } Y_1 \\ p_m^e \cos[k_{y2m}(y-h)] + q_m^e \sin[k_{y2m}(y-h)], & \text{for } Y_2 \\ r_m^e \cos[k_{y3m}(h+b+1-y)], & \text{for } Y_3 \end{cases}$$

$$p_m^e = \cos(k_{y1m}h)$$

$$q_m^e = \frac{-\epsilon_2 k_{y1m}}{\epsilon_1 k_{y2m}} \sin(k_{y1m}h)$$

$$r_m^e = [\cos(k_{y1m}h) \cos(k_{y2m}b) - \frac{\epsilon_2 k_{y1m}}{\epsilon_1 k_{y2m}} \sin(k_{y1m}h) \sin(k_{y2m}b)] / \cos(k_{y3m}l)$$

$$k_{y1m} = (\epsilon_1 k^2 - k_{xm}^2 - \epsilon^2)^{\frac{1}{2}}$$

$$k_{y2m} = (\epsilon_2 k^2 - k_{xm}^2 - \epsilon^2)^{\frac{1}{2}}$$

$$k_{y3m} = (\epsilon_3 k^2 - k_{xm}^2 - \epsilon^2)^{\frac{1}{2}}$$

$$k^2 = \omega^2 \epsilon_0 \epsilon_0$$

## 7.2. Functions used in eqn (2)

$$e_m^h(y) = \begin{cases} \sin(k'_{y1m}y), & \text{for } Y_1 \\ p_m^h \cos[k'_{y2m}(y-h)] + q_m^h \sin[k'_{y2m}(y-h)], & \text{for } Y_2 \\ r_m^h \sin[k'_{y3m}(h+b+1-y)], & \text{for } Y_3 \end{cases}$$

$$p_m^h = \sin(k'_{y1m}h)$$

$$q_m^h = \frac{k'_{y1m}}{k'_{y2m}} \cos(k'_{y1m}h)$$

$$r_m^h = [\sin(k'_{y1m}h) \cos(k'_{y2m}b) + \frac{k'_{y1m}}{k'_{y2m}} \cos(k'_{y1m}h) \sin(k'_{y2m}b)] / \sin(k'_{y3m}l)$$

$$k'_{y1m} = (\epsilon_1 k^2 - k_{xm}^2 - \epsilon^2)^{\frac{1}{2}}$$

$$k'_{y2m} = (\epsilon_2 k^2 - k_{xm}^2 - \epsilon^2)^{\frac{1}{2}}$$

$$k'_{y3m} = (\epsilon_3 k^2 - k_{xm}^2 - \epsilon^2)^{\frac{1}{2}}$$

- [14] Morgan, S.P.: 'Effect of surface roughness on eddy-current losses at microwave frequencies', J Appl Phys, 1949, 20, pp 352-358.
- [15] James, J.R. and Hall, C.: Unpublished laboratory report, Royal Military College of Science, 1982.
- [16] Henderson, A. and James, J.R.: 'Design of microstrip antenna feeds - Part 1: Estimation of radiation loss and design implications', IEE Proc H, Feb 1981, pp 19-25.
- [17] Hall, P.S. and James, J.R.: 'Design of microstrip antenna feeds - Part 2: Design and performance limitations of triplate corporate feeds', IEE Proc H, Feb 1981, pp 26-34.
- [18] Wenger, N.C.: 'Launching of surface waves on axial cylindrical reactive surface', NASA Technical Note, D-3180 Jan 1966.
- [19] Collier, R.J. and Chang, G.X.: 'A broad band to image guide transition', Proc 12th European Microwave Conference, Helsinki Aug 1982, pp 526-533.
- [20] Arnold, J. and Butlin, R.S.: 'Extended frequency range GaAs MESFETs using 0.3  $\mu$ m gate lengths', Proc 11th European Microwave Conference, Amsterdam, Sept 1981, pp 264-269.
- [21] Gelsthorpe, R.V., Williams, N. and Davey, N.M.: 'A low cost technology for millimetre wave integrated circuits', The Radio and Electronic Engr, 1982, 52, pp 522-528.
- [22] Van Heuven, J.H.C.: 'A new integrated waveguide to microstrip transition', IEEE Trans MTT-24, Mar 1976, pp 144-147.
- [23] James, J.R. and Henderson, A.: 'High-frequency behaviour of microstrip open-circuit terminations', IEE J Microwaves, Opt, and Acoust, 1979, 3, pp 205-218.
- [24] Reference [1] above, p 57.
- [25] Henderson, A., England, E. and James, J.R.: 'New low-loss millimetre-wave hybrid microstrip antenna array', Proc 11th European Microwave Conference, Amsterdam, 1981, pp 825-830.
- [26] Solbach, K.: 'Slots in dielectric image line as mode launchers and circuit elements', IEE Trans 1981, MTT-29, 1, pp 10-16.
- [27] Hammerstad, E.O. and Bekkadal, F.: 'Microstrip Handbook', ELAB Report STF44 A74169, The University of Trondheim - The Norwegian Institute of Technology.



solution appears to lie in the technology of fully integrating the antenna feeder with the rest of the equipment.

#### ACKNOWLEDGEMENT

This research was supported by the Sci. Eng. Res. Council (UK).

#### 6. REFERENCES

- [1] James, J.R., Hall, P.S. and Wood, C.: 'Microstrip antenna theory and design' Peter Peregrinus Ltd, 1981, IEE Electromagnetic Waves Series 12.
- [2] James, J.R., and Hall, P.S.: 'Microstrip antennas and arrays, Part 2: New array-design techniques', IEE J Microwaves, Opt and Acoust, 1977, 1, (5), pp 175-181.
- [3] Itoh, T.: 'Dielectric millimeter wave integrated circuits', Chap 5 in Infrared and millimeter waves, Vol 4, Millimeter Systems, Ed by K J Button and J C Wiltse, Academic Press 1981.
- [4] Henderson, A. and James, J.R.: 'A survey of millimetre wavelength planar antenna arrays for military applications', The Radio and Electronic Engr, 1982, 52, pp 543-550.
- [5] John, G., Henderson, A. and James, J.R.: 'Analysis of insular guide launcher radiation loss and comparison with microstrip counterparts', Proc 12th European Microwave Conference, Helsinki, August 1982, pp 534-539.
- [6] Knox, R.M.: 'Dielectric waveguide microwave integrated circuits - an overview', IEEE Trans 1976, MTT-24, pp 806-814.
- [7] Reference [1] above, Chapter 2.
- [8] Solbach, K. and Wolff, I.: 'The electromagnetic fields and the phase constants of dielectric image lines', IEEE Trans 1978, MTT-26, pp 266-274.
- [9] Mittra, R., Hou, Y.L. and Jammec, V.: 'Analysis of open dielectric waveguides using mode matching technique and variational methods', IEEE Trans 1980, MTT-28, pp 36-43.
- [10] Toullos, P.P. and Knox, R.M.: 'Image line integrated circuits for system applications at millimeter wavelengths', Final Rep, Contract DAAB07-73-C-0217, US Army Electronics Command Report ECOM-73-0217-F, July 1974.
- [11] Schneider, M.V.: 'Dielectric loss in integrated microwave circuits', Bell Syst Tech J, 1969, 48, pp 1421-1444.
- [12] Pucel, R.A., Masse, D.J. and Hartwig, C.P.: 'Losses in microstrip', IEEE Trans 1968, MTT-16, pp 342-350.
- [13] Pucel, R.A., Masse, D.J. and Hartwig, C.P.: 'Correction to "Losses in Microstrip"', IEEE Trans 1968, MTT-16, p 1064.

sections show how this different action is brought about by the change in conductor loss.

When the antenna feeder curves in Fig 12a and b are compared it is seen that microstrip ( $\epsilon_r = 2.32$  and  $3.8$ ) and insular guide ( $\epsilon_r = 10$ ) have comparable losses ( $L_g + L_l$ ) for  $21 \leq N_\lambda \leq 25$  depending on the launching horn height, whereas a comparison of the same microstrip cases with insular guide having  $\epsilon_r = 3.8$  shows that comparable losses occur for  $3 \leq N_\lambda \leq 4.5$ . However, it is known<sup>4</sup> that dielectric structures require a high permittivity and the radiation released gradually over many wavelengths to achieve control of the radiating elements, comparable to that of microstrip antennas. On this basis microstrip is seen to be advantageous for  $N_\lambda \leq 25$ . Another point to consider is that  $\beta/k$  differs for microstrip and insular guide and for a given physical length of aperture the insular guide feeder will have a larger  $N_\lambda$ , thus increasing  $L_g$  and raising the breakeven point to beyond  $N_\lambda = 25$ .

If we now assume that each feeder structure is fully integrated with the receiver and/or transmitter circuit there will be no launcher loss ( $L_l = 0$ ) and insular guide becomes the lower loss feeder for all  $N_\lambda$  as shown in Fig 13, where the additional loss due to the antenna terminal load  $L_t$  is also included. The additional loss  $L_t$  depends on the actual antenna design and is typically 0.5dB for microstrip<sup>27</sup> at  $N_\lambda \sim 15$ . No data is available for insular guide but previous<sup>25</sup> experimental work indicates that  $N_\lambda > 20$  would be required to reduce  $L_t$  to 0.5dB. This is plotted as a single point in Fig 13. In making the comparisons in Fig 13 it is assumed that it has been possible to construct a lossless transition from tightly coupled microstrip (insular guide) in the receiver/transmitter circuits to the loosely coupled microstrip (insular guide) in the antenna. Such transitions are likely to require long tapering sections. Furthermore we have made reference to insular guide circuits knowing that such arrangements are very state-of-the-art and have yet to be developed.

## 5. CONCLUSIONS

Loss mechanisms  $L_g$ ,  $L_l$  and  $L_t$  associated with microstrip and insular guide travelling wave array feeders have been identified and analytical results derived for  $L_l$  and  $L_g$ . Present day millimetre wave equipment makes predominant use of conventional metal waveguide and this investigation has established (Fig 12a and b) that for linear antennas of length about 20 guide wavelengths having similar radiation pattern control, the two types of antenna structures have comparable system losses. The precise break even point depends on many factors such as the extent to which a larger horn can be used in low profile applications, whether the antenna is resonant or travelling wave, the dielectric material used, and other constraints on the antenna specification. A significant reduction in launcher loss is thus needed to make dielectric structures competitive and this can in principle be brought about by complete integration of the antenna with a similar feed guide in the transmitting or receiving equipment. A gradual transition between the tightly bound fields in the circuit region and loosely bound fields in the antenna region is a requisite. In this situation insular guide has a distinct advantage over microstrip (Fig 13) but this result presumes that a technology for insular guide receiver/transmitter circuits exists or is forth coming. In the meantime it may be practical to seek other more compatible launchers for insular guide based on microstrip (Table 1) which can itself be connected to metal waveguides without excessive launcher loss. In conclusion it is seen that the electrical compatibility of these types of antenna feeders with the field guiding structures to which they are connected have a dominant effect on the antenna system loss and the optimum

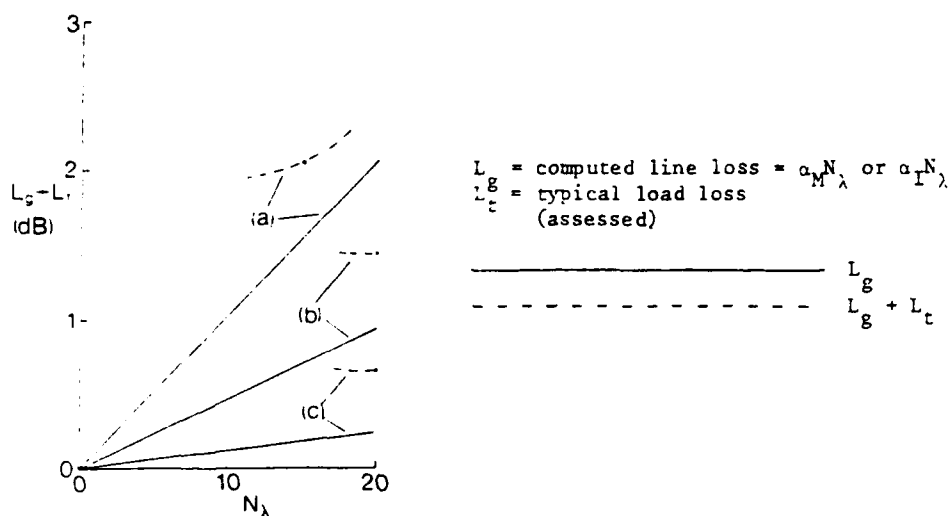


Fig. 13. System loss comparison of microstrip and insular guide ( $E_{11}$  mode) antenna feeder loss for optimal integration - thus no launcher is required.

- (a) microstrip :  $h = 0.032$ ,  $\epsilon_1 = 3.8$ ,  $\tan \delta = 0.0001$ ,  $50\Omega$   
 (b) insular guide:  $a = 0.14\lambda = 1.58b$ ,  $h = 0.242b$ ,  $\epsilon_1 = 2.32$ ,  $\epsilon_2 = 10$ ,  
 $\tan \delta_1 = 0.001$ ,  $\tan \delta_2 = 0.001$   
 (c) insular guide:  $a = 0.26\lambda = 1.58b$ ,  $h = 0.242b$ ,  $\epsilon_1 = 2.32$ ,  $\epsilon_2 = 3.8$ ,  
 $\tan \delta_1 = 0.001$ ,  $\tan \delta_2 = 0.0001$

$$\xi = \frac{Z_m \epsilon_e}{0.40} \left( \frac{\lambda_0}{\pi h} \right)^2 \quad (13)$$

$Z_m$  and  $\epsilon_e$  are the impedance and effective relative permittivity of the microstrip line. For antennas and their feeder lines on the same substrate the line fields need to be loosely coupled and  $\xi$  must be small provided

$$\frac{h}{\lambda_0} < \frac{1}{4(\epsilon_r)^{1/2}} \quad (14)$$

where the condition<sup>24</sup> ensures that excessive substrate surface waves are not generated. The launcher loss for both types of conditions is based on typical results (Table 1) for ridge waveguide launchers. A similar situation is given in Fig 12b for types of insular guide ( $E_{11}^y$  mode) having tight ( $\frac{\epsilon}{k}$  approaching  $\epsilon_2^{1/2}$ ) and loosely ( $\frac{\epsilon}{k} \ll \epsilon_2^{1/2}$ ) bound fields applicable to circuit and antenna applications respectively. The transition is a rectangular guide to horn launcher and two horn heights  $H$  are considered in Fig 12b. It is interesting to note that tighter field binding corresponds to a slightly decreased  $L_g$  for insular guide whereas for microstrip it brings about a significant increase in  $L_g$ . Consideration of the loss mechanism and field plots from previous

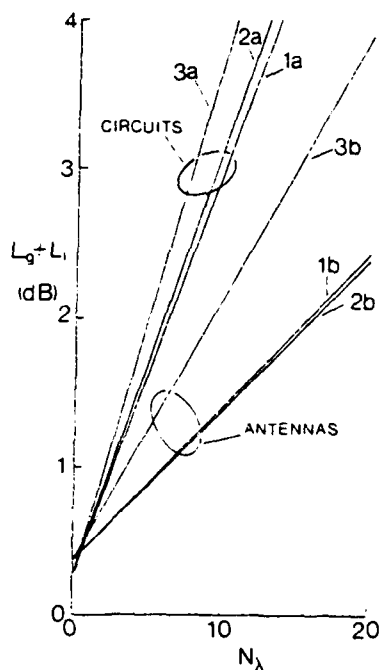


Fig 12a. Microstrip system losses (50Ω line) at 90 GHz for circuit and antenna feeder applications.

$N_\lambda$  = length in guide wavelengths

$L_\lambda$  = computed line loss =  $\alpha_\lambda N_\lambda$

$L_1^g$  = associated ridge waveguide launcher loss (from experimental data)

1a  $h = 0.017\lambda_0$ ,  $\epsilon_1 = 2.32$

1b  $h = 0.041\lambda_0$ ,  $\tan \delta = 0.001$

2a  $h = 0.009\lambda_0$ ,  $\epsilon_1 = 3.8$

2b  $h = 0.032\lambda_0$ ,  $\tan \delta = 0.0001$

3a  $h = 0.005\lambda_0$ ,  $\epsilon_1 = 10$

3b  $h = 0.02\lambda_0$ ,  $\tan \delta = 0.001$

$\Delta = 0.005 \text{ mm}$

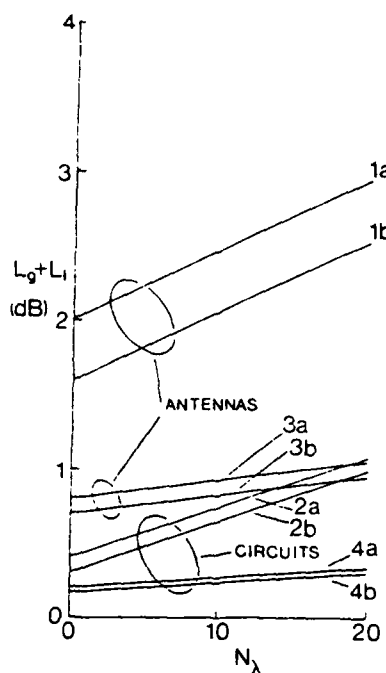


Fig 12b. Insular guide ( $E_{11}^y$  mode) system loss at 90 GHz for circuit and antenna feeder applications.

$N_\lambda$  = length in guide wavelengths

$L_\lambda$  = computed line loss =  $\alpha_\lambda N_\lambda$

$L_1^g$  = associated computed horn launcher loss (two horn sizes are given in each case, curve (a)  $H < \lambda_0$  and curve (b)  $H \sim 5\lambda_0$ )

1. a =  $0.14\lambda_0$ , 2. a =  $0.25\lambda_0$

a =  $1.58b$ ,  $h = 0.242b$ ,  $\epsilon_1 = 2.32$ ,

$\epsilon_2 = 10$ ,  $\tan \delta_1 = 0.001$ ,

$\tan \delta_2 = 0.001$

3. a =  $0.26\lambda_0$ , 4. a =  $0.45\lambda_0$

a =  $1.58b$ ,  $h = 0.242b$ ,  $\epsilon_1 = 2.32$

$\epsilon_2 = 3.8$ ,  $\tan \delta_1 = 0.001$ ,

$\tan \delta_2 = 0.0001$

$\Delta = 0.005 \text{ mm}$

the insular guide and aperture susceptance respectively.  $\Gamma$  is the reflection coefficient for the  $E_{11}^y$  mode in the aperture assuming the horn taper is very gradual and  $Y_0$  is the wave admittance in the horn mouth, the latter region denoted by A. The remaining terms are defined in appendix section 7.3. Taking the near field storage term B as a small effect:

$$\eta \sim \frac{G_r}{(G_r + G_s)} (1 - |\Gamma|^2) \quad (12)$$

A simple choice of trial field such as

$$\begin{aligned} E_{cA}^y &= 1, -a \leq x \leq a, 0 \leq y \leq h + b \\ &= 0, \text{otherwise} \end{aligned}$$

gave values of  $\eta$  in excess of the chopped result based on Theory A Fig 10. When the fields of Theory A eqn (1) and (2) are substituted for the trial field, the results for  $\eta$  are similar to those of the chopped method based on Theory A, Fig 10 showing somewhat less radiation loss. Fig 11 gives a comparison with dimension a the parameter. Thus with a more realistic trial field the  $\eta$  results of the variational analysis are of similar order and exhibit the same behaviour as the chopped distribution method. The variational theory has therefore given confidence to the results obtained by the simpler chopped distribution method based on Theory A but adds no new information. There is dearth of experimental results in the literature and in Table 1 we present some relevant data by others together with our measurements, the latter substantiating the order of radiation loss for microstrip and insular guide launchers. The microstrip to insular guide launcher loss Table 1 is a useful result suggesting that the transition fields are more compatible than those of the waveguide to insular guide transition.

#### 4. ANTENNA SYSTEM LOSS COMPARISONS

The sources of unwanted power loss associated with an antenna feeder are compounded and referred to as the system loss. An operating frequency of 90 GHz is selected since it lies in a band of considerable current interest. Launcher loss  $L_1$ , loss along the guide length  $L_g$  ( $= \alpha_N N_g$  or  $\alpha_T N_g$ ) and the terminal loss  $L_t$  on a travelling wave antenna feeder are the constituents of system loss considered here. For a resonant antenna array there is no terminal load thus  $L_t = 0$  but additional losses of this magnitude arise because of resonator action<sup>2</sup>.  $L_g$  gives a good approximation to the loss of a long linear antenna where the microstrip or the dielectric guide acts as a travelling wave feeder with the radiating elements adjacent to the line or actually embedded in it as discontinuities<sup>4</sup>. Two dimensional millimetre wave arrays comprised of travelling wave linear arrays appear to present particular problems concerning the realisability of a viable corporate feed system as used at microwave<sup>17</sup> and are not considered here. It should be noted that the reduction of feeder loss by parallel feeding each radiating element has been considered impractical at millimetre wavelengths and thus omitted from this investigation.

Fig 12a gives the launcher and the line loss associated with lengths of microstrip for both circuit applications and linear antenna arrays. The transition is from rectangular waveguide to microstrip. The distinction previously<sup>2,5</sup> pointed out is that for circuit applications the fields must be tightly bound and  $\xi$  must be made large where

Transition Details	Launcher	Frequency GHz	Substrate relative permittivity	launcher dimensions and other details	n dB (Z)	
					Theory	Measured
Waveguide (rect) to microstrip <sup>20</sup>	Ridge Waveguide	40	$\epsilon_1 = 4$	-	-	0.25 (5.5)
Coax to microstrip	Coaxial <sup>16</sup> Conductor	13	$\epsilon_1 = 2.3$	$h = 0.035\lambda_0$ 50 $\Omega$ line	0.0174 (0.4) Fig 8	0.1 <sup>†</sup> (2.5)
Waveguide (rect) to insular guide	Horn	9.5	$\epsilon_1 = 2.3$ $\epsilon_2 = 10$ $a = 0.5$ cm $b = 0.316$ cm $h = 0.0765$ cm	$H = 2\lambda_0$ $d \gg H^0$	1.25 (25)	1.32 (26.2)
Microstrip to insular guide <sup>21</sup>	Strip horn with open sides	$\sim 30$	$\epsilon_1 = 2.3$ $\epsilon_2 = 9.8$	-	-	< 0.2 (< 4.5)

<sup>†</sup> measurement error dominated by tolerance in line loss measurement.

Table 1. Data on experimental launchers.

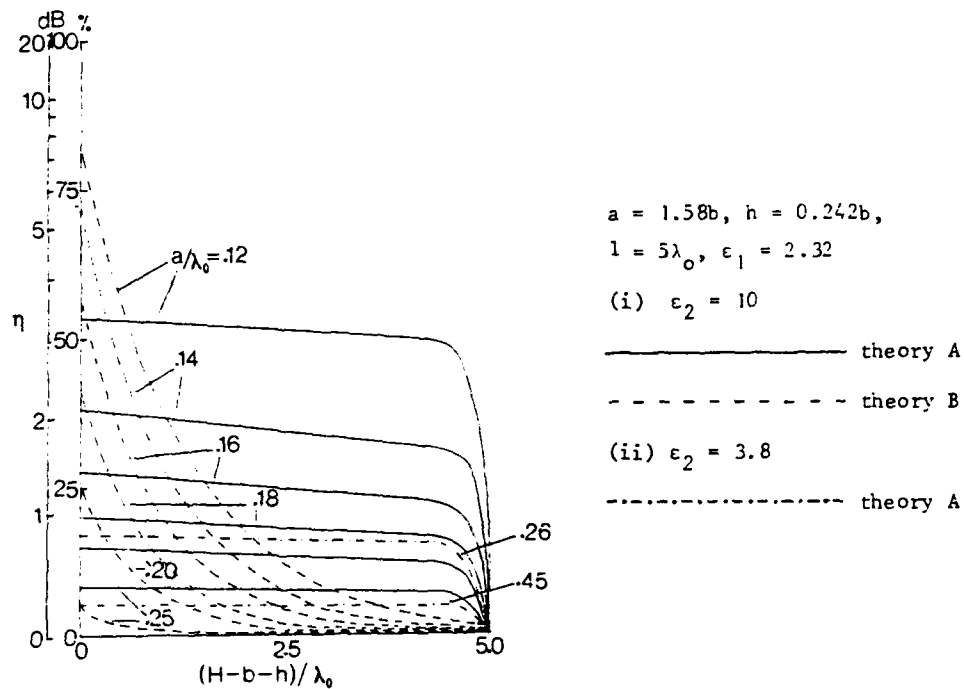


Fig. 10. Horn launching loss  
(Chopped surface wave method)

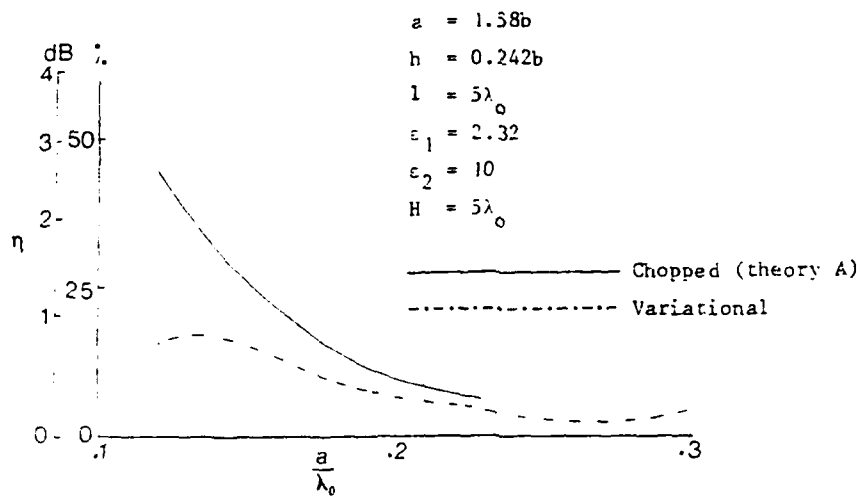


Fig. 11. Horn launching loss

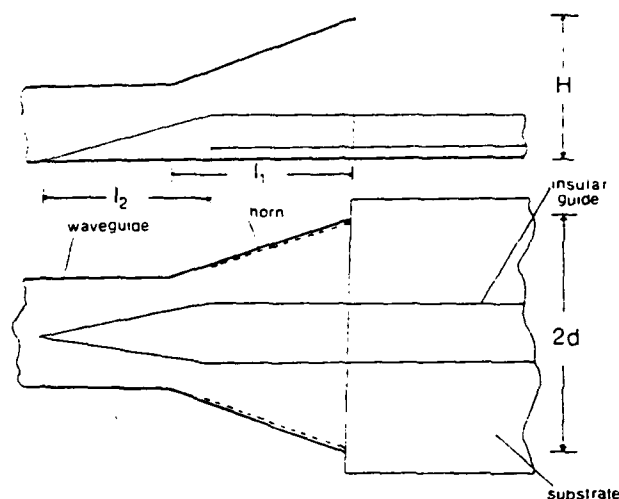


Fig. 9. Horn launcher connecting rectangular metal waveguide to insular guide. The substrate enters horn up to dielectric tapered section;  $l_1$  and  $l_2$  are several insular guide wavelengths.

A more accurate analysis of the horn launcher has been carried out using the variational method previously used<sup>16</sup> on microstrip transitions. For insular guide launching the method is computationally involved and requires several simplifying assumptions. As in the chopped surface wave distribution method the tapered region of the horn cannot be taken into account and is assumed to be a gradual transition. The horn aperture field for  $z < 0$  is taken as that of Theory A eqn (1) and (2) which presumes that  $2d \gg H$ . The insular guide fields for  $z > 0$  are derived from Theory B eqn (3) and denoted by  $(\vec{E}_s, \vec{H}_s)$ . The radiation field for  $z > 0$  is represented by the continuous eigenvalue spectrum and denoted by  $(\vec{E}_r, \vec{H}_r)$  appendix section 7.3.

The variational method requires an estimate of the field in the xy plane at  $z = 0$  and this is referred to as the trial field  $\vec{E}_A$ . On relating the discrete and continuous mode spectrums to  $\vec{E}_A$  and asserting continuity of the fields in the trial field plane we obtain:

$$Y_0 \left( \frac{1 - \Gamma}{1 + \Gamma} \right) = G_r + G_s + jB$$

$$\frac{G_r}{Y_0} = P_F \int_0^k \int_0^{\sqrt{k^2 - k_y^2}} \frac{(\hat{z} \cdot \int_A \vec{E}_A \times \vec{H}_r dA)^2}{P_r} dK_x dK_y \quad (11)$$

$$\frac{G_s}{Y_0} = \frac{P_F}{P_s} (\hat{z} \cdot \int_A \vec{E}_A \times \vec{H}_s dA)^2$$

where  $G_r$ ,  $G_s$  and  $B$  are the radiation conductance, conductance load presented by



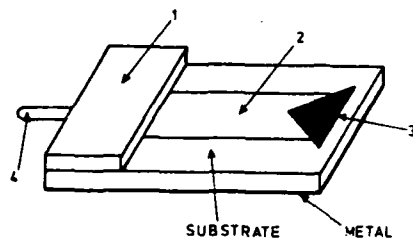


Fig 1: General form of millimetre planar linear array. (1) Launcher (2) Array of elements (3) Load (4) Input

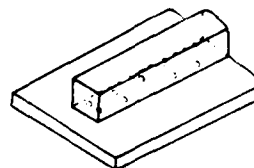


Fig 2: Image guide linear array consisting of holes drilled into a ground plane [2].

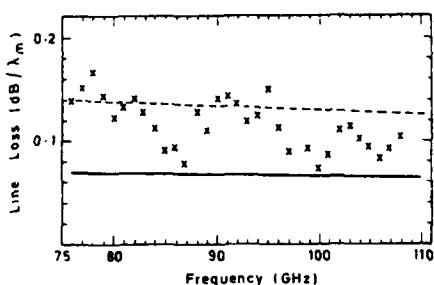


Fig 3: Microstrip loss at millimetres  
 xxx measured  
 — computed loss without roughness  
 - - - computed loss with roughness

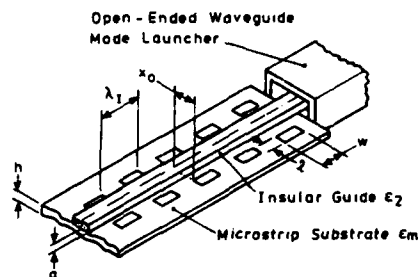


Fig 4: Hybrid microstrip array

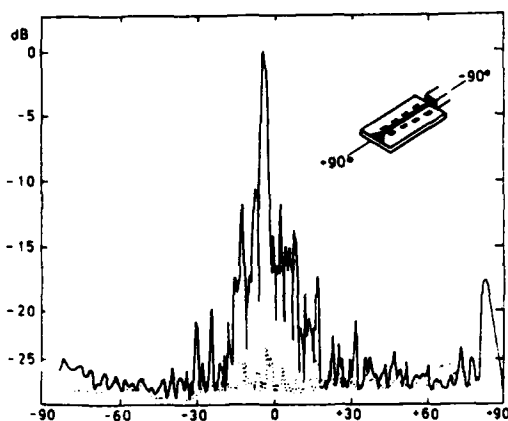


Fig 5: Radiation pattern of hybrid array, Fig 4, measured at 90 GHz  
 .... cross-polar

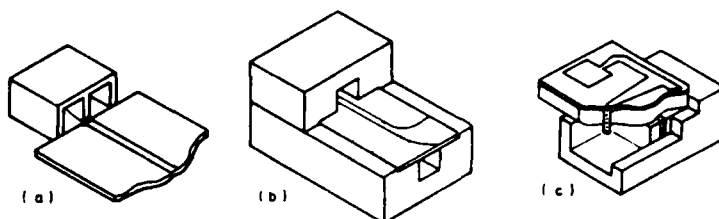


Fig 6: Launchers for microstrip applications,  
(a) Ridge (b) E-plane (c) Back-fed probe.

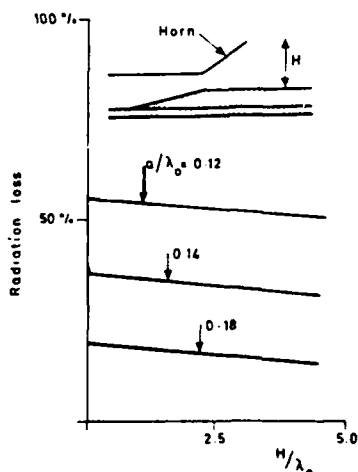


Fig 7: Calculated radiation loss of horn/insular guide launcher.

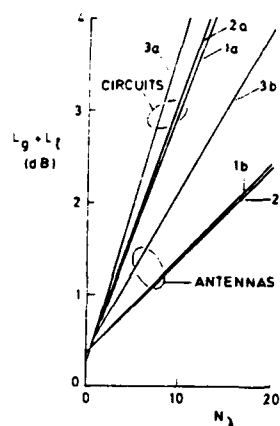


Fig 8: Microstrip systems loss at 90 GHz for circuit and antenna applications (50 ohm lines)

- (1) Plastic (a)  $h=0.017\lambda_0$   
(b)  $h=0.041\lambda_0$
- (2) Quartz (a)  $h=0.009\lambda_0$   
(b)  $h=0.032\lambda_0$
- (3) Ceramic (a)  $h=0.005\lambda_0$   
(b)  $h=0.02\lambda_0$

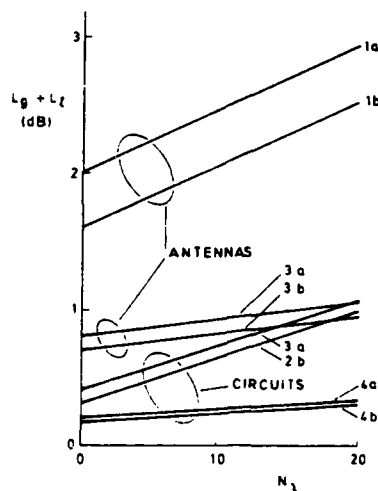


Fig 9: Insular guide systems loss at 90 GHz.  $\epsilon_m = 2.32$   
Horn (a)  $H < \lambda_0$   
Horn (b)  $H \sim 5\lambda_0$

- (1)  $h=0.017\lambda_0$ ,  $\epsilon_2=10.0$
- (2)  $h=0.25\lambda_0$ ,  $\epsilon_2=10.0$
- (3)  $h=0.26\lambda_0$ ,  $\epsilon_2=3.8$
- (4)  $h=0.45\lambda_0$ ,  $\epsilon_2=3.8$

$a=1.58b$ ,  $h=0.24b$

$b$  is the thickness of the guide  $\epsilon_2$ .

Appendix 8.2

Dielectric Corporate Feeds For Arrays  
Employing Dielectric Waveguides

## 8.2 DIELECTRIC CORPORATE FEEDS FOR FOR ARRAYS EMPLOYING DIELECTRIC WAVEGUIDES

As we already possess a design for an effective linear insular guide array, we considered it appropriate that we try to connect several together, in parallel, with some form of corporate feed using a compatible transmission media. Prior to the experimental work, note was taken of the capabilities of power dividers in planar optical guides and a brief review now follows.

### 8.2.1 A SHORT REVIEW OF POWER DIVISION AND SPREADING IN PLANAR OPTICAL WAVEGUIDES

Multiway power splitting has already been carried out at optical wavelengths using buried and etched surface waveguides where a difference of about 1% between the refractive index of the guide and that of the surrounding media is regarded as substantial. Optical power dividers are diverse and are listed below.

- (a) Branch line couplers Figure 1 (a)
- (b) Split-tree type couplers - Y Junction Figure 1 (b)
- (c) Directional couplers Figure 1 (c, d, e, f)
- (d) Tapers Figure 1 (g, h)
- (e) Combined Taper and Y-junction Figure 1 (i)

Branch type couplers have a coupling ratio dependent upon the branch angle  $\alpha$  see Figure 1 (a). Branch couplers with 1, 2, 3, 4 and 5 degree branch angles have been constructed and require a shallow branch angle of about 2 degrees to achieve an equal power split. Typically, the optical guide width is  $75 \mu\text{m}$  which requires the length of branch guide in contact to be  $2149 \mu\text{m}$ . Assuming a wavelength of less than  $0.7 \mu\text{m}$ , this is greater than 3000 wavelengths long. Y-junction couplers used mainly for coupling optical fibres also require shallow branch angles and exhibit increasing losses and mode selectivity with increasing branch angle, Figure 1 (b).

A similar power splitting action has been achieved with a 3-waveguide directional coupler, Figure 1 (c). If the coupling length  $L$  is made  $L = \ell/\sqrt{2}$  ( $\ell$  = length for complete coupling from one guide to another) then an equal power split can be achieved. This is the synchronous condition where the propagation constants of all three guides must be equal and it is very sensitive to tolerances. Both the guide dimensions and the gap width between individual guides must be closely controlled. Power combination cannot be achieved unless both inputs have equal phase. The same synchronous condition requires tight control of cross-section and separation distance for the 2 guide directional coupler of Figure 1 (d) and requires coupling lengths in the range 100 to 10,000 guide

wavelengths in optical guides. Small differences in the propagation constants of the coupled guides can seriously degrade performance and can be avoided at the expense of increased complexity, by using a tapered coupling region, as in Figure 1 (e). Coupling is no longer synchronous but total energy coupling can be achieved with less stringent tolerance requirements. This technique has been applied to successive power divisions between a large number of guides as in Figure 1 (f) and again requires a total length of many hundreds of wavelengths.

The previous cases have dealt with power division, but a similar case is that of power spreading from a linear guide to a planar or slab guide, for example. Here, adequate power spreading requires a long transition region. Analysis has shown that a 90% coupling efficiency can be achieved between a  $50\text{ }\mu\text{m}$  wide planar guide and a  $3\text{ }\mu\text{m}$  wide linear guide with a transition region of length 2 mm. This corresponds to a transition length of over 2800 wavelengths ( $\lambda g < 0.7\text{ }\mu\text{m}$ ), see Figure 1 (g). Coupling between two guides of different propagation constants (or refractive indices,  $n$ ) can be achieved by providing an intermediate value of  $n$ , as shown in Figure 1 (h). Again, high coupling efficiencies require a long and very gentle transition.

The final class of optical power dividers covered combines both a linear to planar, tapered, transition and a Y-junction from the planar guide to two linear guides, see Figure 1 (i). Between the transition region and the fork region, there is a wide slab guide of uniform width. Two sources of loss are apparent,

- (1) mode mismatch between the guided modes in the uniform guide and the fork waveguide modes and,
- (2) loss associated with the directional changes between the wide waveguide and the forked guides. This loss can be minimized as there is an optimum fork angle which minimizes directional change loss. This structure has been analysed and no practical results are known of, but from the foregoing results such a structure would require both a very long transition region of many hundreds of wavelengths and very shallow initial fork angles. The case of more than two output guides has not been analysed, but would require an even longer transition region in order to achieve a uniform power distribution across the wide face of the transition region.

In contrast more abrupt changes of direction have been achieved using dielectric image lines in the 20 to 26 GHz frequency range using metallic reflectors at right-angle bends, Tee-junctions and Y-junctions. Once the rough position for the location of the reflector on a right-angle bend has been found, it's position is not critical when aiming for minimum bending loss, see Figure 1 (j). The insertion loss for single-mode operation

was measured at 2.22 - 3.22 dB compared to 2.43 - 2.92 dB for multi-mode operation. The Tee-junction of Figure 1 (k) exhibited an insertion loss of 4.26 dB and an isolation of 8.5 dB for 3 dB power division. This isolation was increased to 20 dB in the Y-junction of Figure 1 (l) and the insertion loss was little different at 4.22 dB. Smaller branch angles were considered to reduce the insertion loss which was mainly due to radiation as the measured reflection losses were everywhere less than -10 dB. This is an important result showing that compactness in wavelengths is obtained only at the expense of a significant loss.

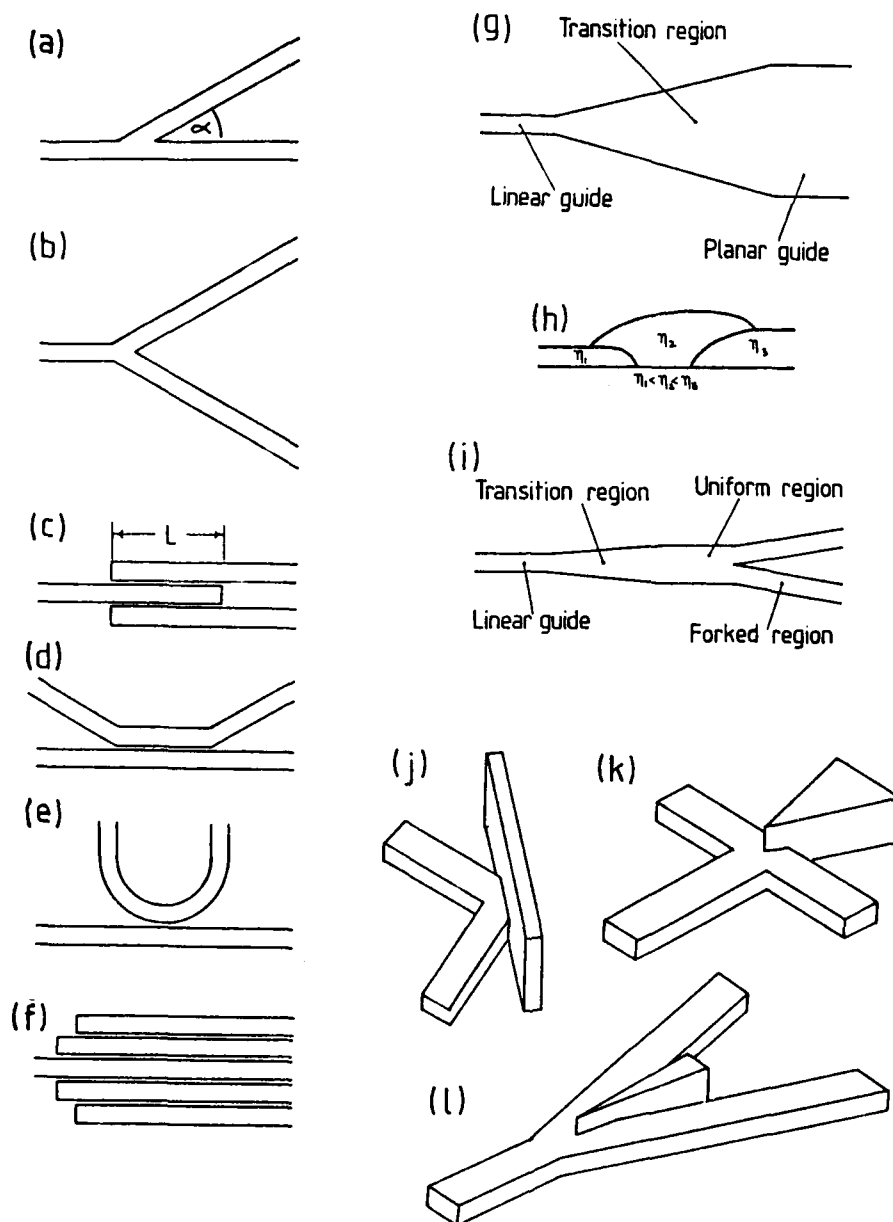
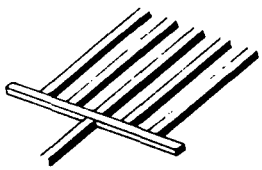
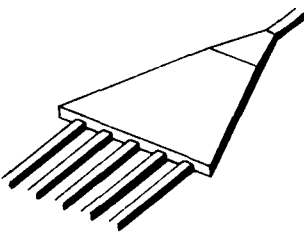
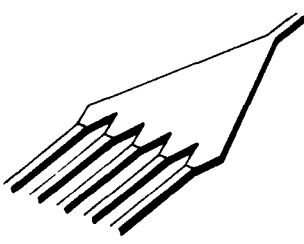


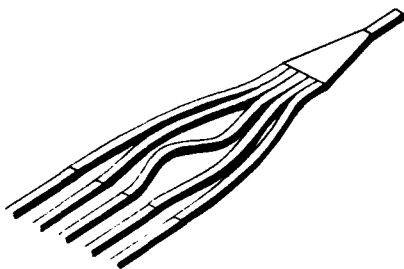
Fig 1: Schematic representations of various power splitting and spreading structures

### 8.2.2 SUMMARY OF EXPERIMENTAL RESULTS ON DIELECTRIC CORPORATE FEEDS FOR A TWO-DIMENSIONAL INSULAR GUIDE ARRAY

Dielectric feeds were designed to feed a 40 x 10 element two-dimensional array. Taking into account individual array losses and launcher losses the expected gain was 27 dBi at 90 GHz assuming no radiative or dissipative losses in the corporate feed region. Experiments were carried out on the following structures.

	<p>(1) Measured gain was 13 dBi compared to expected gain of 27 dBi leading to an estimated efficiency of 4%. Power in input guide did not spread to outer guides but continued on into central guide in array. Disconnecting the two outer guides at the main junction caused a 1 dB increase in gain.</p>
	<p>(2) With the horn section height twice that of the input and array guides, feed radiation dominated and there was no discernable beam. Feed loss was estimated to be about 27 dB and the efficiency of the feed less than 1%. The horn length was about 10 guide-wavelengths.</p>
	<p>(3) The horn section dimensions were similar to feed 2 (above). The horn section height was reduced to that of the array guides and the horn was cut into a series of tapers in an attempt to force power into the array guides.</p> <p>A beam was discernable with a gain of 8 dBi. Feed loss was estimated to be about 17 dB and the feed efficiency about 2%.</p>
	<p>(4) The short horn section of about 3 guide wavelengths in length did not allow adequate spreading of the input power and most of the power coupled to the central guide.</p> <p>Before the sides of the horn section were trimmed lack of phase</p>





control caused multiple beams with a spread of about 10 degrees and a maximum gain of 10 dBi. Trimming of the sides of the horn section concentrated power into central guide and gain was measured at 9 dBi. Feed losses were estimated to be about 18 dB and efficiency about 1.6%.

NOTE: It was found, experimentally, that the butt joints used to join sections of the insular guide together were responsible for a radiation loss of between 3 and 4 dBs per joint.

Appendix 8.3

Millimetre-wave Hybrid  
Dielectric-Microstrip Antenna Array <sup>7</sup>.

# Millimetre-wave hybrid dielectric-microstrip antenna array

Prof. J.R. James, B.Sc., Ph.D., D.Sc., F.I.M.A., C.Eng., F.I.E.R.E., F.I.E.E.,  
G. John, B.Sc., M.Sc., Ph.D., and C.M. Hall, B.Sc.

*Indexing terms:* Antennas; Dielectrics; Microwave components; Waveguides

**Abstract:** The new concept of using dielectric guides as a replacement for microstrip lines in linear microstrip arrays is conceived as a means of reducing the antenna dissipative loss, while retaining many of the attractive manufacturing and operational advantages of printed arrays. This hybrid microstrip-dielectric array takes the form of an insular guide to which the microstrip elements are to be coupled. Precise field representations for the insular guide enable design data for dissipative losses and element coupling to be analysed, principally for the  $E_1$  and  $E_3$  insular guide modes. For ease of manufacture and good coupling control, the microstrip elements take the form of proximity coupled resonant patch antennas, and measurements at both millimetre wavelengths and on microwave scaled models substantiate analytical results throughout. A 40-element travelling-wave hybrid array is designed illustrating the reduction in dissipative losses, the sensitivity to dimensional tolerances and the compatibility of the hybrid antenna concept with dielectric, as opposed to conventional metal, waveguide transmitter/receiver circuits.

## List of principal symbols

$a$	= half guide width of insular guide
$b$	= thickness of dielectric in insular guide
$f_r$	= frequency of resonance
$h$	= thickness of substrate in insular guide and microstrip
$k$	= free-space wave number $= 2\pi/\lambda_0$
$k_{yim}, \bar{k}_{yim}, k'_{yim}, \bar{k}'_{yim}$	= wave numbers (in $y$ -direction) for the modes in insular guide with $i = 1, 2, 3$
$k_{xm}, \bar{k}_{xm}, k'_{xm}, \bar{k}'_{xm}$	= wave numbers (in $x$ -direction) for the modes in insular guide
$l$	= length of microstrip patch
$w$	= width of microstrip patch
$x_0$	= separation of patch from the insular guide
$C$	= percentage of insular guide power coupled to narrow microstrip line
$C_R$	= percentage of insular guide power coupled to radiation in patch
$C_T$	= percentage of insular guide power coupled to patch
$E_i, H_i$	= transverse fields of incident wave for narrow line coupling
$E_c, H_c$	= transverse fields of coupled wave for narrow line coupling
$E_f, H_f$	= fields in insular guide
$E_s, H_s$	= fields in substrate
$E_{mn}, E_{mn}^*$	= modes in insular guide with $m$ and $n$ positive integers
$J$	= fictitious currents
$K_j$	= power coupled to $j$ th microstrip patch
$M, N, M', N'$	= number of modes used in TE- and TM-solutions to solve for $\beta$
$P_c, P_d, P_R$	= power loss in patch due to losses of conductor, dielectric and radiation, respectively
$P_j$	= power radiated by $j$ th microstrip patch
$P_m$	= power coupled to microstrip line
$P_i$	= total power flow in insular guide
$P_L$	= power absorbed in load termination
$Q_c, Q_d, Q_R$	= $Q$ -factors related to patch conductor, dielectric and radiation losses, respectively
$Z_m$	= transverse wave impedance in microstrip $= (\mu_0/\epsilon_0\epsilon_r)^{1/2}$

$Z_0$	= wave impedance in free space
$\alpha_m, \alpha_f$	= attenuation constant in microstrip and insular guide, respectively
$\beta$	= insular guide phase constant
$\delta$	= skin depth
$\delta_{ij}$	= Kronecker delta
$\tan \delta$	= loss tangent
$\tan \delta_{eff}$	= effective loss tangent (all the losses combined)
$\epsilon_{r1}, \epsilon_{r2}$	= relative permittivities
$\epsilon_r$	= effective relative permittivity
$\lambda_0, \lambda_m, \lambda_g$	= wavelengths in free space, microstrip and insular guide, respectively
$\phi_m^{\pm}(y)$	= sinusoidal functions of $y$
$\mu_0, \epsilon_0$	= free-space permeability and permittivity
$\Delta$	= RMS surface roughness
$\omega$	= angular frequency $= 2\pi f$

## 1 Introduction

At microwave frequencies, microstrip antennas [1] have outstanding constructional and cost advantages which, for many applications, outweigh their disadvantages, such as the intrinsic dissipative loss of the microstrip lines, cross-polarisation effects [2] and unwanted radiation [3] from input connections and transitions. The choice [4] of the substrate thickness  $h$  and relative permittivity  $\epsilon_r$  is important because it enables a tradeoff to be obtained between the main performance parameters, such as antenna efficiency, bandwidth, crosspolarisation and array sidelobe levels.

In principle it is possible to scale down in size a microwave microstrip antenna for operation at millimetre wavelengths, and examples have been previously described [5]. An obvious difficulty concerns the mechanical and electrical tolerances of the substrate and copper conductors, but the microstrip-line loss increases with frequency and is seen as a major limitation for millimetre-wave arrays requiring long microstrip feeders. Smaller arrays of microstrip radiating elements having shorter feeder lengths do not, therefore, suffer such losses to the same extent and are viable propositions at millimetre wavelengths. Thus, there is a need to devise a lower-loss feeder for large microstrip arrays while retaining as many of the advantages associated with the printed planar antenna concept as possible. To satisfy the latter requirement, the feeder should be compatible with the substrate requirements [4] dictated by the

Paper 3410H (E11) first received 22nd February and in revised form 25th May 1984  
The authors are with the Department of Electrical & Electronic Engineering, Royal Military College of Science, Shrivenham, Swindon SN6 8LA, England

microstrip radiating elements. The purpose of this paper is to describe one way of creating lower-loss feeders using rectangular dielectric guides. The dielectric guide is bonded on to the substrate, the latter accommodating a conventional array of microstrip radiating elements that can be manufactured as a separate printed subassembly. From an electrical standpoint this hybrid dielectric microstrip structure has distinct advantages: the feeder is an insular dielectric waveguide which possesses very low transmission loss [6, 14], while the microstrip radiating elements ensure better control [7] of the radiation pattern than that obtainable if discontinuities were created in the dielectric feeder itself [15]. Mechanically the new structure is more complicated than a microstrip antenna, particularly with regard to the coupling mechanism between the feeder and microstrip elements. The coupling process is thus an important aspect, and is analysed in Section 2 together with the dissipative and radiative losses of a microstrip element. The design and construction of a linear travelling-wave antenna, based on analytical results, is dealt with in Section 3. Measurements support the investigation throughout, and the performance and potential of this new type of antenna are critically assessed in Section 4 and conclusions are given. Some supporting mathematical detail is located in the Appendix.

## 2 Analysis of coupling and radiation

### 2.1 Insular guide fields

The feeder arrangement described is illustrated in Fig. 1, showing the rectangular dielectric slab of width  $2a$  and

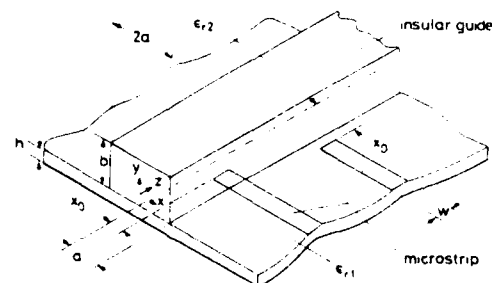


Fig. 1 Insular guide feeder for narrow microstrip lines

height  $b$  mounted on a substrate of height  $h$ . The substrate is backed by a conducting ground plane on the underside.  $\epsilon_{r1}$  and  $\epsilon_{r2}$  are the relative permittivities of the substrate and slab, respectively, and if  $\epsilon_{r2} > \epsilon_{r1}$  the composite structure behaves as an insular dielectric waveguide. Also shown in Fig. 1 are microstrip lines of width  $w$  placed normal to the insular guide axis at a distance  $x_0$ . We wish to examine the coupling to the microstrip line under the general condition that the line either protrudes under the dielectric slab ( $x_0 < a$ ) or does not contact the latter ( $x_0 > a$ ). In this Section the field representations and transmission characteristics of the insular guide are considered under the constraints imposed by available materials. The microstrip substrate was Duroid 5870 with  $\epsilon_{r1} = 2.3$ , and the dielectric slab was Duroid 6010 with  $\epsilon_{r2} = 10$ . The slab was machined to size and bonded to the substrate with cyanoacrylate adhesive. Extensive calculations are demanded to quantify the radiation characteristics of the hybrid antenna, and the insular guide fields ( $E_i$ ,  $H_i$ ) are obtained by a mode-matching method [8] rather than by relying entirely on the well known simpler, but less accurate, effective dielectric constant method [9]. We have described and compared both these latter methods else-

where [8], and for the mode-matching method the fields in the  $y$ -direction for  $|x| \leq a$  are of the form:

$$\begin{aligned} E_{iy} &= \sum_{m=1}^N (k_{xm}^2 + \beta^2) \frac{\cos(k_{xm}x)}{\cos(k_{xm}a)} \frac{\phi_m^e(y)}{a(y)} A_m \\ H_{iy} &= \sum_{m=1}^N (k_{xm}^2 + \beta^2) \frac{\sin(k_{xm}x)}{\sin(k_{xm}a)} \frac{\phi_m^h(y)}{a(y)} B_m \end{aligned} \quad (1)$$

where  $\beta$  is the phase constant of the wave transmitted along the insular guide and the term  $\exp(-j\beta z)$  is omitted in eqns. 1 and 2.  $\phi_m^e(y)$  and  $\phi_m^h(y)$  are functions of  $y$  and are given in Appendix 7.1 for different sections of the guide in the  $y$ -direction. For the region  $|x| \geq a$ , the  $y$ -directed fields are

$$\begin{aligned} E_{iy} &= \sum_{m=1}^N (k_{xm}^2 + \beta^2) \exp[-k_{xm}(x-a)] \frac{\phi_m^e(y)}{a(y)} C_m \\ H_{iy} &= \sum_{m=1}^N (k_{xm}^2 + \beta^2) \exp[-k_{xm}(x-a)] \frac{\phi_m^h(y)}{a(y)} D_m \end{aligned} \quad (2)$$

Similar representations are obtained for the other Cartesian field components in other regions around the insular guide.  $A_m$ ,  $B_m$ ,  $C_m$ ,  $D_m$  are unknown coefficients obtained from the solution of a matrix equation generated by invoking the boundary conditions at the various guide surfaces, and  $M$ ,  $M'$ ,  $N$  and  $N'$  are made large enough to achieve satisfactory convergence of  $\beta$  and the resulting fields. Some further relationships between the functions in eqns. 1 and 2 are given in Appendix 7.1.

Computed  $\beta$  results for the first four insular guide modes are given in Fig. 2 and field plots in Fig. 3. The

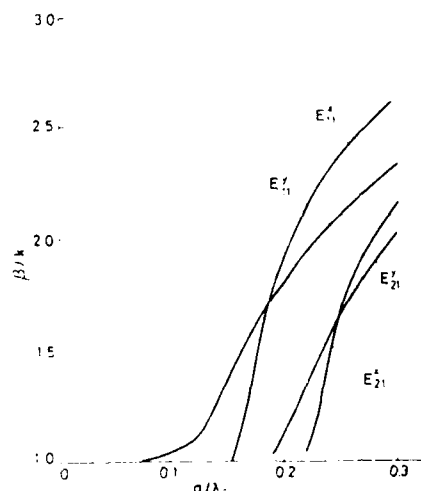


Fig. 2 Computed mode chart for insular guide using mode-matching method

$h = 0.633a$ ,  $b = 0.153a$ ,  $\epsilon_{r1} = 2.3$ ,  $\epsilon_{r2} = 10$

latter are very sensitive to any source of inaccuracy, and some discontinuity in the field behaviour is apparent at the vertical wall of the slab due to a degree of incompleteness inherent in the mode-matching process [8].

The total insular guide loss due to dielectric and ground plane conductor losses has been previously calculated [8] using the mode-matching fields and the perturbation approach. A typical computed result for both the  $E_{11}^e$ - and  $E_{11}^h$ -modes is shown in Fig. 4, together with a computed result for a microstrip line. Conventional mode nomenclature is used here, whereby  $E_{pg}$  represents a modal  $E_i$ -field

with  $p$  and  $q$  power concentrations in the  $x$ - and  $y$ -directions, respectively. The microstrip loss includes an empirical correction for surface roughness [8], where  $\Delta$  = RMS roughness. Measurements to date indicate a

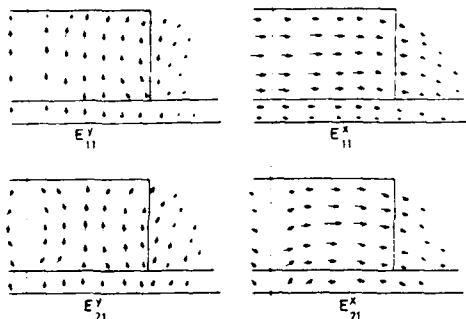


Fig. 3 Field plots for the first four modes in the insular guide  
Electric field direction and magnitude are indicated by arrows

somewhat higher loss for microstrip ( $\epsilon_{r1} = 2.3$ ) of about 0.13 dB  $\lambda_m$  at 90 GHz, where  $\lambda_m$  = microstrip wavelength. Measurements on insular guide substantiate the order of the computed loss, but have reduced accuracy due to radiation from transitions and the low level of loss being measured. The curves of Fig. 4 readily indicate the order of reduction in feeder loss that is offered by the hybrid dielectric-microstrip antenna concept.

$$P_m = \frac{1}{2Z_m h w} \left| \int_{x_0=0}^h \int_{z=0}^w \sum_{m=1}^M \frac{A_m}{\epsilon_{r1}} (\beta^2 + k_{zm}^2) \cos(k_{ym} y) \frac{\cos(k_{zm} x_0)}{\cos(k_{zm} a)} \exp(-j\beta z) dy dz \right|^2$$

$$= \frac{[1 - \cos(\beta w)]}{\beta^2 Z_m h w} \left[ \sum_{m=1}^M \frac{A_m (\beta^2 + k_{zm}^2) \sin(k_{ym} h) \cos(k_{zm} x_0)}{\epsilon_{r1} k_{ym} \cos(k_{zm} a)} \right]^2 \quad (4)$$

$$C = (P_m / P_I) \times 100\%$$

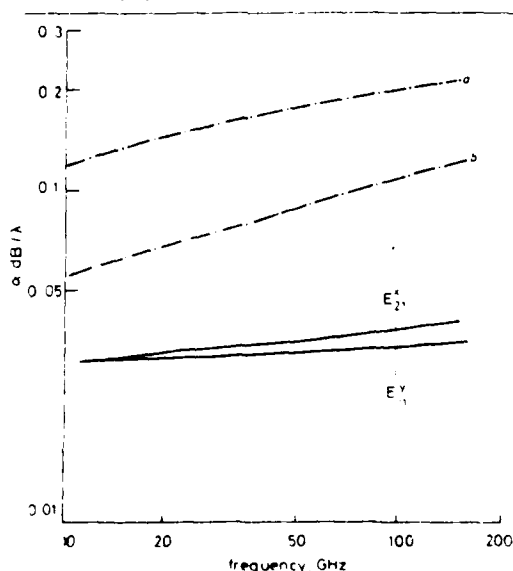


Fig. 4 Losses in microstrip line and insular guide

$\lambda$  = wavelength in respective transmission line  
 $a = 0.017 \lambda_0, \epsilon_{r1} = 10, \tan \delta_1 = 0.001, \Delta = 0.005 \text{ mm}$  (microstrip 50  $\Omega$ )  
 $b = 0.041 \lambda_0, \epsilon_{r2} = 2.3, \tan \delta_2 = 0.001, \Delta = 0.005 \text{ mm}$  (insular guide)  
 $a = 0.25 \lambda_0, \epsilon_{r1} = 0.833, \epsilon_{r2} = 0.153, \epsilon_{r3} = 2.3, \tan \delta_1 = 0.001, \tan \delta_2 = 0.001, \tan \delta_3 = 0.001$

## 2.2 Coupling to narrow microstrip lines

The degree of coupling obtainable when a narrow line is in the proximity of the insular guide feeder of Fig. 1 is of interest as a coupling element in both microstrip circuit and antenna applications. Microstrip circuits and/or antennas can, in principle, be attached to the narrow microstrip line if a sufficient range of coupling levels can be achieved in a controlled manner. The microstrip line of width  $w$  is assumed to be matched and be deployed as in Fig. 1 either within or exterior to the insular guide structure, although from a manufacturing standpoint deployment under the dielectric slab is a complication. The power  $P_m$  coupled to the microstrip line is calculated using a form [10] of the Lorentz reciprocity theorem applicable to coupling between unbounded structures:

$$P_m = \frac{1}{2Z_m} \left| \int_A \mathbf{E}_i \cdot \mathbf{E}_t d\mathbf{a} \right|^2 \text{Re} \int_A |\mathbf{E}_t|^2 d\mathbf{a} \quad (3)$$

$\text{Re}$  = real part and  $A$  is the transverse aperture where the incident wave with transverse fields  $(\mathbf{E}_i, \mathbf{H}_i)$  generates the coupled wave with transverse fields  $(\mathbf{E}_t, \mathbf{H}_t)$ . We approximate by taking  $A$  as the transverse rectangular section of dimension  $h \times w$ , situated in the substrate at the input end of the microstrip line of Fig. 1,  $(\mathbf{E}_i, \mathbf{H}_i)$  are the components of  $\mathbf{E}_i, \mathbf{H}_i$  transverse to aperture  $A$  and  $(\mathbf{E}_t, \mathbf{H}_t)$  is the quasi-transverse electromagnetic wave (TEM) in the microstrip line. Thus, on normalising the TEM-field to unity,  $E_t = \hat{y}$  and  $Z_m$  = transverse wave impedance in microstrip =  $[\mu_0 (\epsilon_r \epsilon_{r1})]^{1/2}$ , where  $\epsilon_r$  = effective relative dielectric constant of microstrip line. On substituting in eqn. 3 for  $\mathbf{E}_i$  and for  $\mathbf{E}_t$  in eqn. 1, for  $|x_0| \leq a$ ,

where  $C$  is the percentage of insular guide incident power  $P_I$  coupled to the microstrip line. For  $|x_0| > a$ ,  $P_m$  is obtained from eqns. 2 and 3.  $P_I$  is obtained by integrating the Poynting vector of the guide fields (eqns. 1 and 2 and related equations) over the guide cross-section. Computed results (Fig. 5) for eqn. 4 give the variation of coupling with  $x_0$ . A monotonic decay occurs when the coupling aperture  $A$  is moved progressively further away from the region of field concentration, which, for  $E_{11}^x$ , is at  $x = 0$ . The  $E_{11}^x$ - and  $E_{31}^x$ -modes, with, respectively, two and three power concentrations across the slab width, show corresponding peaks in the coupling curves in Fig. 5 for increasing  $x_0$ . The  $E_{21}^x$ -mode also has two power concentrations, but, having orthogonal polarisation, does not couple as effectively. The results are seen to be discontinuous at  $x = a$  due to the approximate fields used, which are, however, sufficient to illustrate the general behaviour and the order of coupling which falls to a very low value for  $x_0 > a$ . For strips wider than  $0.1 \lambda_0$ , one might expect the periodic nature of the insular guide field in the  $z$ -direction to affect the coupling, and this is evident in Fig. 6. From eqn. 4 it is seen that when  $\beta w = 0, 2\pi, 4\pi$ , etc. the coupling is zero, and for the  $E_{11}^x$ -case computed this occurs at  $w/\lambda_0 = 0.45, 0.9$  etc. In practice, such wide strips would cause excessive perturbation of the insular guide fields if  $x_0 < a$ .

## 2.3 Coupling to rectangular microstrip patch antenna

The above computations show that only low coupling levels are possible for narrow lines unless located under the

dielectric slab. The coupling becomes significant for large strip widths, but then the microstrip line is too wide for conventional feeder applications where the purpose would

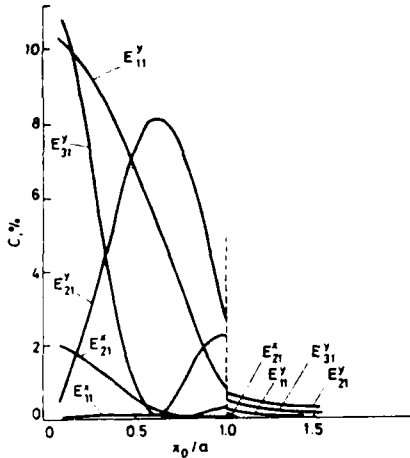


Fig. 5 Percentage of power  $C$  coupled to a narrow microstrip line from insular guide as a function of separation  $x_0$  from the guide  
 $l = 0.25\lambda_0$ ,  $b = 0.633a$ ,  $h = 0.153a$ ,  $\epsilon_{r1} = 2.3$ ,  $\epsilon_{r2} = 10$ ,  $w = 0.1\lambda_0$ ,  $\lambda_0 = 2.01$  cm

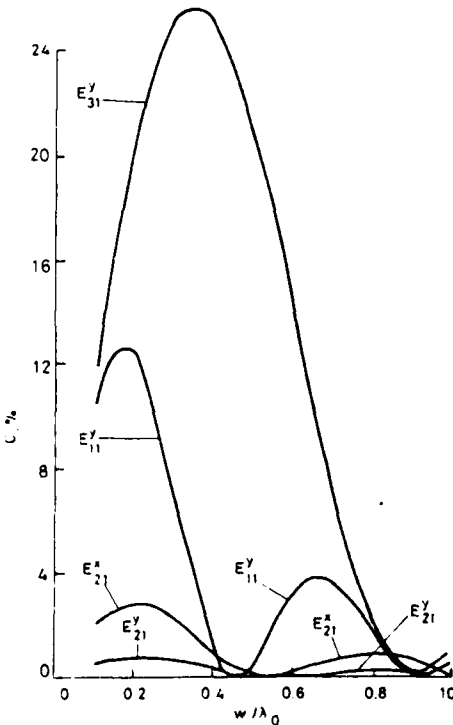


Fig. 6 Percentage of power  $C$  coupled to a narrow microstrip line from insular guide as a function of strip width  $w$   
 $l = 0.25\lambda_0$ ,  $b = 0.633a$ ,  $h = 0.153a$ ,  $\epsilon_{r1} = 2.3$ ,  $\epsilon_{r2} = 10$ ,  $x_0 = 0.1a$ ,  $\lambda_0 = 2.01$  cm

be to couple distant microstrip circuits to the insular guide. For the wide microstrip case the coupling configuration has the reality of an insular guide coupling to a wide microstrip resonator not in contact with the dielectric slab (see Fig. 7). Microstrip patch resonators can act as antennas, and we are thus interested in the conditions that

allow the patch to radiate the coupled power strongly. Unlike the narrow line case, the insular guide fields can now generate fields in both the  $x$ - and  $y$ -directions in the

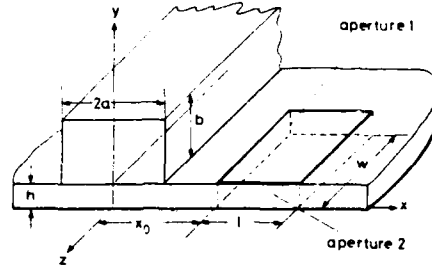


Fig. 7 Insular guide feeder for microstrip patch resonator antenna

microstrip patch. To analyse the coupling, fictitious currents  $J$  are assumed to exist in apertures on two of the vertical sides of the microstrip resonator to accommodate the various excitation polarisations, where

$$\text{aperture 1} = (x = x_0, 0 \leq y \leq h, 0 \leq z \leq w)$$

$$\text{aperture 2} = (x_0 \leq x \leq x_0 + l, 0 \leq y \leq h, z = 0) \quad (5)$$

The microstrip patch electric field  $E_s$  in the substrate then satisfies (see Reference 1, p. 96)

$$(\nabla^2 + \epsilon_{r1}k^2)E_s = j\omega\mu_0 J - \frac{1}{j\omega\epsilon_0\epsilon_{r1}} \nabla \nabla \cdot J \quad (6)$$

where  $J$  is defined by the insular guide magnetic field in the aperture thus:  $J = \hat{n} \times H_l$ , and  $\hat{n}$  is the unit vector normal to the aperture. Hence,

$$J = H_{l2} \hat{y} \quad (\text{aperture 1}) \quad (7)$$

$$J = -H_{l1} \hat{y} \quad (\text{aperture 2})$$

From the mode-matching theory of eqns. 1 and 2, the insular guide magnetic fields are

$$H_{l1} = - \sum_{m=1}^M j\omega\epsilon_0 \beta \exp[-\tilde{k}_{xm}(x-a)] \tilde{\phi}_m^*(y) C_m \cos(\beta z)$$

$$H_{l2} = - \sum_{m=1}^M j\omega\epsilon_0 \tilde{k}_{xm} \exp[-\tilde{k}_{xm}(x-a)] \tilde{\phi}_m^*(y) C_m \sin(\beta z) \quad (8)$$

It is assumed that the substrate is electrically thin and the resonator field has a  $y$ -independent electric field solely in the  $y$ -direction. Furthermore, the  $\tilde{\phi}_m^*(y)$  functions can be averaged over the substrate thickness; hence,  $\tilde{\phi}_m^*(y) \approx \sin(\tilde{k}_{y1m}h)/(\tilde{k}_{y1m}h)$ . The eigenfunction representation [11] of the cavity modes is

$$E_{sv} = \sum_{p=0}^{\infty} \sum_{q=0}^{\infty} \frac{B_{pq}}{\epsilon_{r1}k^2 - k_{pq}^2} \cos\left(\frac{p\pi z}{w}\right) \cos\left[\frac{q\pi(x-x_0)}{l}\right]$$

$$H_s = - \frac{j}{\omega\mu_0} \hat{y} \times \nabla E_{sv} \quad (9a)$$

$$k_{pq}^2 = \left(\frac{p\pi}{w}\right)^2 + \left(\frac{q\pi}{l}\right)^2 = \epsilon_{r1}k^2 \quad (9b)$$

where the cavity action is assumed to be brought about by magnetic walls on the microstrip patch boundaries. From Appendix 7.2 the cavity mode coefficients generated by aperture 1 depend only on  $p$ , and  $B_{pq}$  is denoted by  $B_p$ :

$$B_p = \frac{2}{(1 + \delta_{p0})w} k^2 \sum_{m=1}^M \tilde{k}_{xm} X_m \frac{\beta}{\beta^2 - (p\pi/w)^2} \times [1 - (-1)^p \cos(\beta w)] \quad (10)$$

Bandwidth of a dipole element on the lower substrate of the height  $h$  had to be inferred from the results of James et al<sup>2</sup>, Pues et al<sup>4</sup> and Pozar<sup>5</sup> and from photographs for the aspect ratio. Bandwidths in the region of 0.5% to 1.4% were estimated for  $w/\ell$  between 1/2 and 1/4; the average estimated bandwidth being 1% therefore the measured bandwidths were approximately equal to  $M$ . Bandwidth increased with increasing total height  $H_T$  with a maximum of  $M = 7.7$  being observed at  $H = H_T/h = 3.0$ ; see Figure 8(r).

Sabban<sup>18</sup> used a parasitic resonator separated by an air gap above a feeder resonator; best results were obtained with concentric circular resonators. Sabban's results were obscured by the lack of essential information as the frequency and the air gap thickness were omitted. All we know is that the antenna operated at X-band (8-12 GHz) and that the lower substrate thickness and dielectric constant were 1.5 mm and 10.3. At X-band  $h/\lambda_0$  would be in the range 0.04 to 0.06 so the bandwidth was estimated to be in the range 2% to 7% as the bandwidths of square and circular disc elements are similar. The measured bandwidths of the rectangular and circular parasitic antennas were 10% and 11% respectively ( $VSWR \leq 2.0:1$ ). Bandwidth ratios were then estimated at  $M = 6.4$  to 1.82 for the rectangular antenna and  $M = 7.0$  to 2.0 for the circular disc antenna.

These results for parasitic antennas are presented graphically in Figures 9 and 10 to aid interpretation. Figure 9 plots bandwidth ratio ( $M$ ) against the number of dimensional degrees of freedom which is a measure of complexity ( $C$ ), see note 3, page 77. Figure 10 plots the estimated increase in antenna volume ( $V_p/V$ ) compared to a single element on the same substrate, see note 4, page 77. For a complexity ( $C$ ) value of 6 a two layer vertical parasitic antenna<sup>11</sup>, Figure 8(p), can have 5 times the  $M$  value compared to lateral parasitic antennas<sup>12, 17</sup>, Figure 8(f, h), and for 9 degrees of freedom, a bandwidth ratio eight times greater than the antenna<sup>12</sup> of Figure 8(d), which had quarter-wave parasitic elements coupled to the radiating edges of a half-wave patch. Although their complexity measure is no different, the three element arrangements<sup>19</sup> of Figures 8(i, j, l, m) have reduced  $M$  values compared to the two layer antenna<sup>11</sup> owing to the greater increase in volume obtained with the two layer antenna compared to the quarter-wave shorted parasitic arrangement<sup>12</sup>, Figure 8(d, f). This can be seen clearly in Figure 10, where the bandwidths of all types depend very strongly on the volume ratio.

calculations showed that for each configuration there exists 3 possibilities for resonance. One of which yielded a radiation conductance at the slot of 4 times that of a single radiating edge; energy stored was twice that of a single element. Since bandwidth is proportional to radiated power over stored energy it was thought reasonable to deduce that the bandwidth would be twice that of a single element. For  $VSWR \leq 2.0:1$ , good comparison between measured and calculated bandwidths was found. Greater increases in bandwidth were obtained by Shaubert and Farrar<sup>15</sup> and Dahele and Lee<sup>17</sup>. Shaubert and Farrar<sup>15</sup> placed strips of different lengths close to the non-radiating edges of patch elements, Figure 8(g) and obtained bandwidth ratios of  $M = 3.6$  and  $4.4$ , relative to a patch without parasitics. A smaller increase in bandwidth was obtained by Dahele et al<sup>17</sup> ( $M = 2.85$ ) by placing a parasitic element close to a centre-fed planar monopole element. The parasitic imparted a dual frequency response, see Figure 8(h), with a tuneable upper resonance. A particular combination of spacing and parasitic length led to an increase in the bandwidth of the lower resonance.

Greater increases in  $M$  were obtained by Kumar and Gupta<sup>19</sup> at the expense of greater design complexity. By varying the sizes and separations of parasitic resonators around a central driven element they were able to obtain  $M$  values varying from 4 to 7, see Figure 8 (i, j, k, l, m, n). Greatest bandwidth increases were obtained experimentally using 4 parasitic elements around a central driven element. The important point arising here is that both FEGCOMA, Figure 8(k), and FEDCOMA, Figure 8(n), antennas offer 41% and 31% more bandwidth than the NEGCOMA, Figure 8(i), antenna for twice the design complexity: see note 2, page 77 for explanation of acronyms.

Another class of antennas is those in which the parasitic elements are vertical in extent. Antennas employing vertical parasitic radiators can employ thin substrates, so as to keep feed radiation at low level and still have broad bandwidth<sup>11, 13, 18</sup>. Hall, Wood and Garret<sup>11</sup> tackled this problem in response to the need to improve the bandwidth of radiating elements which are commonly made on high dielectric constant substrates ( $\epsilon_r = 9.8$ ) and have lower efficiency and bandwidth than those built on substrates of a lower dielectric constant. By stacking resonators above a patch resonator on alumina<sup>11</sup> useful bandwidth increases of  $M = 6$  and  $11.8$  were obtained for a single overlaid resonator and  $M = 15.4$  for two overlaid resonators, see Figure 8(o, p, q). The lowest increase in bandwidth ( $M = 6$ ) was obtained with an open-circuited 30 ohm line feed instead of a patch. Again parasitic elements achieved broadbanding by imparting a closely spaced multi-frequency response.

Evaluation of  $M$  was made difficult in the case of electromagnetically coupled (EMC) dipole elements (Oltman and Heubner<sup>13</sup>) as no details of  $M$  or the dipole aspect ratios ( $w/l$ ) were given.



feed probe becomes significant and accentuates the existing bias of the impedance locus towards the inductive side of the complex impedance (Smith) plane. By putting the correct value of capacitance in series with the feed probe, the probe inductance could be tuned out and a bandwidth of square and disc antennas have been found to be similar (see Figure 7). The bandwidth ratio  $M$  was estimated at  $M = 33/17 = 1.94$  or a rough doubling in bandwidth; see note 1, page 77.

Das and Chatterjee<sup>21</sup> showed that conically depressing the upper surface of a disc resonator, radiated power can be increased for a negligible increase in stored energy, Figure 6(c). Calculation and measurement indicated that bandwidth increases with decreasing conical angle,  $\psi$ , (or increasing depth). In this case measurements showed that for a deep depression,  $\psi = 80^\circ$ , the increase in bandwidth was due to frequency splitting reminiscent of Poddar et al.<sup>14</sup>. The experimental results of Das and Chatterjee<sup>21</sup> showed that a decrease in  $\psi$  from  $90^\circ$  to  $85^\circ$  yielded a doubling of the bandwidth. Frequency splitting at  $\psi = 75^\circ$  gave a substantial increase in bandwidth greater than 100%. The input reflection coefficient was nowhere better than -8 dB and the same feed position was used in all three cases ( $S = a/3$  for  $\psi = 90^\circ$  and  $S = \frac{1}{3}$ rd of the slant of height in other cases). Both methods employed to achieve broadband performance<sup>20, 21</sup> yielded bandwidth ratios in the region of  $M = 2$ , where  $M$  is the ratio of bandwidth achieved with some device compared to that of a standard element, see note 1, page 77.

Of additional interest is the semi-air-spaced structure of Figure 6(d) which was cited by Lee et al.<sup>24</sup> and Ness et al.<sup>25</sup> as a method of fine tuning a resonator. No information was given on available bandwidth but it is similar to the structure used by Sabban<sup>18</sup> to obtain greater bandwidth (see section 8.4.4).

#### 8.4.4 Elements Employing Parasitic Elements of Horizontal and Lateral Extent.

Techniques for broadbanding microstrip antennas fall into 2 groups, (1) adjusting the parameters of the substrate  $h$  and  $\epsilon_r$  and (2) the use of parasitic elements around the central, driven element, which are either lateral or vertical in extent. In general broadband performance beyond that obtainable by adjusting  $\epsilon_r$  and  $h$  is obtained by giving the antenna an overlapped multifrequency capability. A subcategory of (1) which imparts a dual frequency response to a patch radiator is the use of stepped and tapered substrates<sup>14, 25</sup>. Figure 8 shows all the antenna types known of to date that employ parasitic element along with their sources.

Wood<sup>12</sup> considered the effect of adding quarter-wave, shorted, parasitic elements to the radiating edges of quarter-wave and half-wave patch elements: Figures 8(c, d, e, f). Wood's

Of special interest is the  $TM_{12}$  annular mode, Figure 5(a), which can have double the bandwidth of a  $TM_{11}$  disc antenna. Figure 7 compares the results of Chew<sup>22</sup> with theoretical results for square,  $TM_{01}$ , antennas<sup>3,5</sup>. For the  $TM_{12}$  annular mode, bandwidth has a dependence upon the thickness ratio  $b/a$  with bandwidth increasing with decreasing  $b/a$ . (If  $b/a$  is made too small, the annulus would become too large). Das and Mathur<sup>23</sup> illustrated this effect by considering the effect of changing the outer radius  $b$  upon the radiation from the inner and outer apertures and showed that for any given value of  $a$ , there exists an optimum choice for  $b$ ; Figure 5(b) shows the calculated variation of  $E_z$  to be a damped sinusoidal variation with radial distance for a specific case. It is convenient here to breakdown the discussion into odd  $TM_{1m}$  ( $m = 1, 3, 5, \dots$ ) and even  $TM_{1m}$  ( $m = 2, 4, 6, \dots$ ) modes.

(1) ODD MODES. Without proper choice of  $b$ , the inner and outer fringing fields cancel resulting in a boresight null. For this particular case,  $a = 1.2$  cm, and a choice of  $b = 6.3$ , or 12 cm results in  $E_z = 0$  at the outer aperture and radiation from the inner aperture only where  $E_z$  is the vertically directed field between conductor and ground plane. At the points  $b = 6.3$  and 12 cm the rate of change of  $E_z$  with the electrical dimension  $k_p b$  is a maximum, where  $k_p$  is the radial propagation constant. Narrow bandwidth is implied because of the sensitivity to frequency. A choice of  $b = 14.75$  cm for the  $TM_{13}$  mode coincides with the second positive maximum of  $E_z$ . This still results in fringing field cancellation from the outer aperture but with minimum sensitivity to frequency unlike a choice of  $b = 12$  cm for  $E_z = 0$ ; this suggests that a wider bandwidth may be achieved.

(2) EVEN MODES. Inner and outer fringing fields have the same polarity for the even modes, Figure 5(a), so  $b$  must be chosen to give an  $E_z$  resulting in inner and outer fringing fields of the same polarity. In this particular case, ( $a = 1.2$  cm) a choice of  $b = 9.45$  cm satisfied this condition and here the rate of change of  $E_z$  with  $k_p b$  is a minimum, which implies minimum sensitivity to frequency and higher bandwidth.

Apart from these theoretical predictions, Das and Mathur<sup>23</sup> did not experimentally investigate the bandwidth of annular ring antennas. Using a coaxial (50 ohm) feed placed at various radial distances between  $a$  and  $b$ , a minimum VSWR of 2.2 was obtained with the feed position at  $S = a + R/3$ , where  $R = (a + b)/2$ , see Figure 6. To date, no other experimental data on annular ring matching or bandwidth is known of.

There have been two attempts at broadbanding disc radiators. Griffin and Forrest<sup>20</sup> noticed that as substrate height is increased in an attempt to achieve an increase in bandwidth, the inductance of the

Bandwidth for square patches was only considered up to the second surface-wave cut-off point.

(2) For much thicker substrates, examination of thin microstrip dipoles on very thick substrates revealed a periodic dependence of bandwidth upon  $h/\lambda_0$  and that the maximum bandwidth on  $\epsilon_r = 12.8$  was greater than for  $\epsilon_r = 2.55$ : maximum bandwidth being 48% ( $h/\lambda_0 = 0.11$ ) and 29% ( $h/\lambda_0 = 0.2$ ) for  $\epsilon_r = 12.8$  and 2.55 respectively.

The periodicity of dipole bandwidth was considered over a much greater range of thicknesses by Alexopoulos<sup>7,8,9</sup> Figure 4(a), who found that the bandwidth maximum occurs just beyond the cut-off point for the second ( $TE_0$ ) surface wave mode. The periodicity in  $h/\lambda_0$  beyond the first maximum following the cut-off points of TE and TM surface wave modes; maxima occurring in the region of TE cut-off and minima in the region of TM cut-off. This is more evident for increasing  $\epsilon_r$ .

Because bandwidth is obtained at the expense of efficiency the conditions for maximum bandwidth and maximum radiating efficiency are not the same. Alexopoulos<sup>9</sup> showed that maximum bandwidth increases monotonically with  $\epsilon_r$  while the bandwidth for maximum radiating efficiency reaches a maximum at  $\epsilon_r = 9.4$ , above which it decreases. Therefore a bandwidth of 26% is achievable on alumina substrates for maximum efficiency, Figure 4(b).

#### 8.4.3 Disc and Annular-Ring Elements

Disc microstrip antennas are essentially narrow band, like rectangular elements, with bandwidth depending primarily upon substrate height and dielectric constant. Measurements by Howell<sup>10</sup> first compared disc and rectangular elements and revealed little difference for comparable thickness and dielectric constants.

Compared to a circular disc antenna, Figure 6(a), an annular ring antenna, Figure 6(b), has less stored energy which implies a greater bandwidth. However, the radiated power as a function of frequency depends very much upon the mode excited. The lowest radiating mode is the  $TM_{11}$ , Figure 5(a), with effective radiation emanating from the outer aperture due to far field cancellation of the inner fringing fields; the  $TM_{11}$  disc mode is similar in form. Chew<sup>2</sup> calculated the bandwidths (bandwidth criteria 3 dB variation) and showed that for similar dimensions and  $\epsilon_r$ , a  $TM_{11}$  circular disc has greater bandwidth than a  $TM_{11}$  annular ring. Excitation of the even higher-order modes,  $TM_{12}$ ,  $TM_{14}$  etc, results in radiation from both inner and outer apertures that reinforces in the far field. Radiation efficiency is potentially doubled compared to the  $TM_{11}$  disc antenna implying double the bandwidth.

$f$  = frequency,  $\epsilon_s$  = stored energy at  $f = f_0$  (resonance) and  $P_R$  = power radiated.

The above reveals that broadband, low-Q, operation can be achieved by reducing the substrate dielectric constant.

Modifications to the radiator geometry in both horizontal and vertical planes can effect  $\epsilon_s$ <sup>14 21 22 23</sup>.  $Q_R$  is a complex function of  $h$  because the substrate height is involved in the calculation of both  $P_R$  and  $\epsilon_s$ .

#### 8.4.2 Rectangular elements

Figure 2(a) shows the results of James et al<sup>3</sup> for square resonators taking into account the generation of surface wave modes in the substrate. The dominant effects on bandwidth are the substrate height in relation to the wavelength ( $h/\lambda_0$ ) and the substrate dielectric constant. At  $h/\lambda_0 = 0.05$  the bandwidths of resonators on substrates for  $\epsilon_r = 1.1$  and 10 differ by a factor of 6 ( $\epsilon_r = 1.1$ , bandwidth = 15%;  $\epsilon_r = 10$ , bandwidth = 2.5%); the bandwidth criteria here was for VSWR  $\leq 2.6:1$ . James et al<sup>2</sup> and Pues et al<sup>4</sup> have examined the effect of patch aspect ratio  $w/\ell$  on bandwidth. Their results, Figure 2(b), show a rough proportionality between increase in bandwidth and increase in  $w/\ell$  up to  $w/\ell = 2$  above which the gain in bandwidth for a given increase in  $w/\ell$  decreases and is associated, in part, with the generation of transverse modes. Practically patches with  $w/\ell > 2$  are not used because of radiation pattern degradation due to these transverse modes. The results of James et al<sup>2</sup> and Pues et al<sup>4</sup> did not take any account of surface-wave generation and would tend to underestimate bandwidth for larger values of  $h/\lambda_0$ . Measured bandwidth results by various workers are included in Figure 2(b) and show an increasing divergence with increasing  $\epsilon_r$  for square resonators with ( $w/\ell = 1$ ). Measurements by Derneryd and Lind<sup>16</sup> showed good comparison up to  $h/\lambda_0 = 0.12$  with increasing divergence towards this limit, showing that for thick substrates surface wave terms must be included in  $Q_R$ .

The behaviour of square microstrip patches and half-wave printed dipoles on very thick substrates was examined accurately by Pozar<sup>5</sup> for dielectric constants of 2.55 (PTFE) and 12.8 (Gallium arsenide) which is considered to be the most practical substrate for antennas in the millimetre region. Two interesting points emerged, Figure 3.

(1) For square patches a cross-over point exists ( $x$ ) at  $h/\lambda_0 = 0.04$  above which the bandwidth on a patch on GaAs is greater than on PTFE. Bandwidths of 27% can be obtained for thick substrates ( $h/\lambda_0 = 0.05$ ) at  $h/\lambda_0 = 0.06$  and 0.12 for GaAs and PTFE respectively (bandwidth criteria, VSWR  $\leq 2.4:1$ ).

## 8.4 A REVIEW OF MICROSTRIP RADIATING ELEMENT BANDWIDTH

### 8.4.1 Bandwidth Criteria

The bandwidth of a microstrip resonator, Figure 1, is generally expressed in terms of its Q-factor which includes terms for metallic and dielectric dissipative losses as well as radiation losses. For an antenna the overall Q-factor is dominated by radiation and the bandwidth is generally judged as the frequency range over which the input reflection coefficient is more than -7 dBs down on that at the band edges. Corrections can be applied to this level depending on the depth of the resonance<sup>1</sup>. An input reflection coefficient of -7 dBs corresponds to an input V.S.W.R. of  $S = 2.6:1$  and for antennas that behave essentially as RLC tuned circuits, the bandwidth for any given VSWR and total Q-factor ( $Q_T$ ) is given by,

$$\text{Bandwidth} = \frac{100(S-1)}{\sqrt{S} Q_T} \% (S>1)$$

The most commonly used convention for expressing impedance bandwidth is the frequency range for which  $VSWR \leq 2:1$ : some workers preferring a  $VSWR \leq 3:1$ . Antennas employing some sort of broad-banding device have non-ideal responses and the depth of the resonance varies between similar antennas. One criteria employed in this sort of case is the bandwidth over which the loss is half that at centre frequency<sup>14</sup>. For multi-element antennas, a 3dB gain variation bandwidth is often employed. Circularly polarized antennas employ the criteria of variation of ellipticity (axial ratio) as this is often the most important performance factor. Ellipticity bandwidths are generally much less than impedance bandwidths and here again the 3 dB variation criteria is the most common with some workers preferring 1 or 2 dB variations. Generally speaking, bandwidth criteria are judged relative to the dominant performance criteria. Travelling-wave arrays, for example, may have input impedance taking a secondary role to the variation of beam position and gain: in certain applications bandwidth may be decided by acceptable sidelobe or cross-polar levels.

The Q-factor of an open microstrip antenna is dominated by the radiation loss factor which is given by:

$$Q_R = \frac{2\pi \epsilon_s f_0}{P_R}$$

$$\text{where } \epsilon_s = \frac{1}{2} \int_V \epsilon_r \epsilon_0 |E_z|^2 dv = \frac{h}{2} \int_A \epsilon_r \epsilon_0 |E_z|^2 da$$

Appendix 8.4

A Review of Microstrip Radiating  
Element Bandwidth

$$r_m^e = \left[ \cos(k_{y1m}h) \cos(k_{y2m}h) - \frac{\epsilon_{r2}k_{x1m}}{\epsilon_{r1}k_{x2m}} \right. \\ \left. \times \sin(k_{y1m}h) \sin(k_{y2m}h) \right] / \cos(k_{y3m}L)$$

$$k_{y1m} = (\epsilon_{r1}k^2 - k_{xm}^2 - \beta^2)^{1/2}$$

$$k_{y2m} = (\epsilon_{r2}k^2 - k_{xm}^2 - \beta^2)^{1/2}$$

$$k_{y3m} = (k^2 - k_{xm}^2 - \beta^2)^{1/2}$$

$$k^2 = \omega^2 \mu_0 \epsilon_0$$

$\epsilon(y)$  and  $\tilde{n}(y)$  = relative permittivities for appropriate region defined by  $y$ .

The analysis is based upon a quasibounded structure with a second ground plane at  $y = h + b + L$ , with  $L$  typically  $5\lambda_0$ . Functions of a similar form exist for  $\phi_m^h(y)$ , where  $k_{y1m}$ ,  $k_{y2m}$  and  $k_{y3m}$  carry a prime. The  $k$ -values for  $|x| > a$  carry a bar, as in eqn. 2, to distinguish them from the  $k$ -values appropriate to  $0 \leq x \leq a$ .

### 7.2 Coupling to microstrip patch

The matching of aperture 1 fields to the microstrip fields involves eqns. 6, 9a and 7 to give

$$\sum_{p=0}^{\infty} \sum_{q=0}^{\infty} B_{pq} \cos\left(\frac{p\pi z}{w}\right) = k^2 \sum_{m=1}^M \bar{k}_{xm} X_m \sin(\beta z)$$

A Fourier decomposition is performed by multiplying both sides by  $\cos(p\pi z/w)$ ,  $p' = 0, 1, 2, 3, \dots$  and integrating over  $0 \leq z \leq w$ , which isolates the terms containing  $p$  to give the result of eqn. 10.

The Fourier decomposition for aperture 2 is similar with both sides of the equation multiplied by  $\cos[q\pi(x-x_0)/l]$ ,  $q' = 0, 1, 2, 3, \dots$  and integrating over  $x_0 \leq x \leq x_0 + l$  to yield eqn. 11.

### 7.3 Measurement of coupling

Sophisticated microwave measurement techniques using network analysers are applicable to unbounded structures such as microstrip lines provided the radiation losses at the input and output transitions are negligible. The measurement of coupling (see Figs. 10 and 11) is an order more difficult and less accurate because of the radiation loss from the waveguide to insular guide transition at each end of the insular guide under test. The transitions were fitted with small flanges to create a horn launcher action [8] and absorbent material was also used. Radiation from the microstrip patch under investigation and reflections from the imperfect insular guide to waveguide transition are other factors creating uncertain errors in the coupling results.

### 7.4 Microstrip patch losses

The losses  $P_d$ ,  $P_r$  and  $P_R$  in Section 2.3, together with their respective  $Q$ -factors  $Q_d$ ,  $Q_c$  and  $Q_R$ , are readily calculated (see Reference 1, Chap. 4) given the cavity fields of the microstrip patch resonator eqn. 8. For instance

$$P_d = \frac{1}{2} \int_{\text{vol}} \omega \epsilon_{r1} \epsilon_0 \tan \delta |E_{Sy}|^2 dv \\ = \frac{1}{2} \omega \epsilon_{r1} \epsilon_0 \tan \delta h w l \sum_{p=0}^{\infty} \sum_{q=0}^{\infty} \\ \times \left[ \frac{B_{pq}}{\epsilon_{r1} k^2 - k_{pq}^2} \right]^2 \frac{(1 + \delta_{p0})}{2} \frac{(1 + \delta_{q0})}{2}$$

$$Q_d = \frac{\omega}{P_d} \text{ (total energy stored in volume of cavity)}$$

The calculation of  $P_R$  is straightforward but extensive, and first the radiation pattern arising from radiation from the magnetic sources on the four sides of the microstrip cavity is obtained and then integration of the Poynting vector yields  $P_R$ . A magnetic source  $K$  is defined as

$$K = -2\hat{n} \times \hat{y} E_{Sy}$$

where  $\hat{n}$  is a unit vector normal to the radiating surface and  $E_{Sy}$  is given from eqn. 8a in each radiating aperture as follows:

$$\sum_{p=0}^{\infty} \sum_{q=0}^{\infty} \psi_{pq} \cos\left(\frac{p\pi z}{w}\right) \text{ for } x = x_0, 0 \leq z \leq w$$

$$\sum_{p=0}^{\infty} \sum_{q=0}^{\infty} \psi_{pq} \cos\left[\frac{q\pi(x-x_0)}{l}\right]$$

$$\text{for } x_0 \leq x \leq x_0 + l, z = 0$$

$$\sum_{p=0}^{\infty} \sum_{q=0}^{\infty} \psi_{pq} \cos(q\pi) \cos\left(\frac{p\pi z}{w}\right)$$

$$\text{for } x = x_0 + l, 0 \leq z \leq w$$

$$\sum_{p=0}^{\infty} \sum_{q=0}^{\infty} \psi_{pq} \cos(p\pi) \cos\left[\frac{q\pi(x-x_0)}{l}\right]$$

$$\text{for } x_0 \leq x \leq x_0 + l, z = w$$

where

$$\psi_{pq} = \frac{B_{pq}}{\epsilon_{r1} k^2 - k_{pq}^2}$$

$$P_R = \frac{1}{Z_0} \left( \frac{k_0 h}{\pi} \right)^2 \left[ \frac{B_{pq}}{\epsilon_{r1} k^2 - k_{pq}^2} \right]^2 \times I(\theta, \phi)$$

where

$$I(\theta, \phi) = \int_{\theta=0}^{\pi/2} \int_{\phi=0}^{2\pi} I_1^2 \sin \theta (I_2 + I_3 - I_4) \\ \times [1 - \cos p\pi \cos wX][1 - \cos q\pi \cos lZ] d\theta d\phi$$

$$I_1 = \frac{\sin(k_0 h \cos \theta/2)}{(k_0 h \cos \theta/2)}$$

$$I_2 = \frac{X^2(1 - \cos^2 \phi \sin^2 \theta)}{[(p\pi/w)^2 - X^2]^2}$$

$$I_3 = \frac{Z^2(1 - \sin^2 \phi \sin^2 \theta)}{[(q\pi/l)^2 - Z^2]^2}$$

$$I_4 = \frac{2XZ \sin \phi \cos \phi (1 + \cos^2 \theta)}{[(p\pi/w)^2 - X^2][(q\pi/l)^2 - Z^2]}$$

$$X = k_0 \sin \theta \cos \phi$$

$$Z = k_0 \sin \theta \sin \phi$$

At and near the microstrip patch resonant frequency the solution is dominated by one term: thus, at resonance, the radiations from the (1, 0) and (1, 1) modes (see Fig. 8) are dominated, respectively, by  $p = 1, q = 0$  and  $p = 1, q = 1$  terms in the above expressions. This property has been made use of in our computations.

for very long arrays where the saving in feeder loss is significant and the coupling to the microstrip resonators has only a small perturbing effect on the insular guide feeder. The shaping of the aperture distribution to obtain lower sidelobe levels is a matter for further development work, but low crosspolarisation levels appear to be readily obtained, which is an important property. The manufacturing tolerance problem encountered at 90 GHz highlights the need for a higher degree of mechanical and

material precision commonly found in semiconductor technology.

The hybrid antenna concept is seen to be ideally compatible with equipment composed of dielectric waveguide circuits, but its deployment with conventional rectangular waveguides can create an additional significant system loss at the launcher transition unless a more gradual, and hence bulkier transition region is incorporated.

## 5 Acknowledgments

This work was supported by the UK Science & Engineering Research Council and the United States Army and Airforce through the European Research Office, London.

## 6 References

- JAMES, J.R., HALL, P.S., and WOOD, C.: 'Microstrip antenna theory and design' (IEE Electromagnetic Wave Series 12, Peter Peregrinus Ltd., 1981)
- HALL, P.S., and JAMES, J.R.: 'Cross polarisation sources in comb line microstrip antenna arrays'. Third International Conference on Antennas and propagation, Norwich, Apr. 1983, pp. 454-458
- HENDERSON, A., and JAMES, J.R.: 'Design of microstrip antenna feeds. Part 1: Estimation of radiation loss and design implications'. *IEE Proc. H, Microwaves, Opt. & Antennas*, 1981, 128, (1), pp. 19-25
- JAMES, J.R., HENDERSON, A., and HALL, P.S.: 'Microstrip antenna performance is determined by substrate constraints'. *MSN Microwave Syst. News*, August 1982, pp. 73-84
- HALL, P.S., GARRETT, C., and JAMES, J.R.: 'Feasibility of designing millimetre microstrip planar antenna arrays'. Agard Conf. Proc. 245 on Millimeter and submillimeter wave propagation and circuits, Munich, Sept. 1978, pp. 31-1-31-7
- KNOX, R.M.: 'Dielectric waveguide microwave integrated circuits—an overview'. *IEEE Trans.*, 1976, MTT-24, pp. 806-814
- HENDERSON, A., and JAMES, J.R.: 'A survey of millimetre wavelength planar antenna arrays for military applications'. *Radio & Electron. Eng.*, 1982, 52, pp. 543-550
- JOHN, G., and JAMES, J.R.: 'Loss comparisons of insular guide and microstrip millimetre antenna array feeders'. *Electromagnetics*, 1983, 3, pp. 217-238
- TOULIOS, P.P., and KNOX, R.M.: 'Image line integrated circuits for system applications at millimetre wavelengths'. Final Report, Contract DAAB07-73-C-0217, US Army Electronics Command Report ECOM-73-0217-F, July 1974
- BARLOW, H.M., and BROWN, J.: 'Radio surfacewaves' (Oxford University Press, 1962), Chap. 9
- SLATER, J.C.: 'Microwave electronics' (Van Nostrand, New York, 1950), Chap. 4
- MIAO, J.F., and ITOH, T.: 'Coupling between microstrip line and image guide through small apertures in the common ground plane'. *IEEE Trans.*, 1983, MTT-31, pp. 361-363
- HENDERSON, A., ENGLAND, E., and JAMES, J.R.: 'New low-loss millimetre wave microstrip antenna array'. 11th European Microwave Conference, Amsterdam, Sept. 1981, pp. 825-830
- BIRAND, M.T., and WILLIAMS, N.: 'Printed dipole millimetre wave array using an insular guide feeder'. *IEE Proc. H, Microwaves, Opt. & Antennas*, 1984, 131, (2), pp. 107-113
- ITOH, T., and ADELSECK, B.: 'Trapped image guide leaky-wave antenna for millimeter wave applications'. *IEEE Trans.*, 1982, AP-30, pp. 505-509

## 7 Appendix

### 7.1 Insular guide field representations

$$\phi_m^e(y) = \begin{cases} \cos(k_{y1m}y) & \text{for } 0 \leq y \leq h \\ P_m^e \cos[k_{y2m}(y-h)] + q_m^e \sin[k_{y2m}(y-h)] & \text{for } h \leq y \leq (h+b) \\ r_m^e \cos[k_{y3m}(h+b+L-y)] & \text{for } (h+b) \leq y \leq (h+b+L) \end{cases}$$

$$p_m^e = \cos(k_{y1m}h)$$

$$q_m^e = -\frac{k_{y2} k_{y1m}}{k_{y1} k_{y2m}} \sin(k_{y1m}h)$$

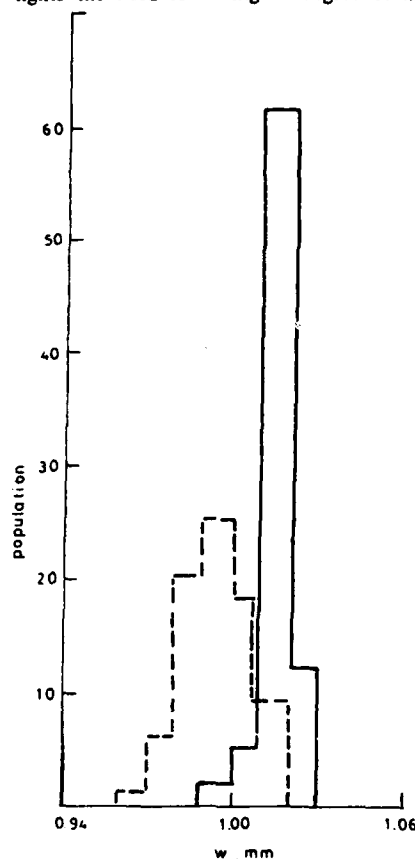


Fig. 16 Tolerances on patch width  $w$  for the antennas in Fig. 15 show error due to etch process

— measured on photographic mask from cut and peel artwork  
 - - - measured on etched resonator using 0.5 oz copper

Table 2: Examples illustrating the beam shift at 90 GHz arising from a given percentage change in the  $b$  and  $h$  dimensions of an insular guide

$b$ , mm	$h$ , mm	$A_g$ , mm	Variation in			Phase shift per wavelength, degrees	Shift in beam, degrees
			$b$ , %	$h$ , %	$A_g$ , %		
0.35	0.127	2.339					
0.35	0.140	2.350	+10		0.47	1.89	0.38
0.35	0.114	2.324	-10		-0.64	2.31	-0.53
0.35	0.144	2.352	+13		0.56	2.0	0.45
0.35	0.118	2.329	-7		-0.43	1.54	-0.35
0.385	0.127	2.183	+10		-6.67	24.0	-5.85
0.385	0.144	2.201	+10	+13	-5.9	21.2	-5.13
0.385	0.118	2.172	+10	-7	-7.14	25.7	-6.29
0.315	0.127	2.518	-10		7.65	27.6	5.81
0.315	0.144	2.525	-10	+13	7.95	28.63	6.03
0.315	0.118	2.512	-10	-7	7.396	26.63	5.63

Nominal guide parameters are  $h = 0.127$  mm,  $b = 0.35$  mm,  $a = 0.5$  mm,  $\epsilon_r = 2.3$ ,  $\epsilon_z = 10$



microwave data in Figs. 2, 8, 9 and 11 for  $E_{11}$ -mode operation with  $\epsilon_{r2} = 10$ ,  $a = 1.1$  mm,  $b = 0.35$  mm. In long linear arrays the aperture distribution will be a very sensitive function of the coupling relationship (see Fig. 11) and empirical corrections to the latter have been attempted.



Fig. 14 90 GHz, 80-element hybrid array

The antenna described in Fig. 15a and Table 1 column (i) was designed using curve (i) of Fig. 11 to achieve a uniform aperture distribution with broadside beam and  $P_{11} = 10\%$  of the available antenna input power eqn. 14. Dimensional and electrical tolerances, and the fact that  $\beta$  is slightly perturbed by the presence of the microstrip resonator, limit the usefulness of experimental iterative methods. The beam squint and sidelobe structure are indicative of the errors in the aperture distribution. It is evident from Fig. 16 that etching errors alone can lead to significant detuning of the microstrip patches, while Table 2 illustrates the sensitivity of the insular guide phase constant, and hence beam shift, to changes in  $h$  and also  $b$ . Variation in  $h$  also causes further detuning of the microstrip patches. The dimensional changes quoted here are not untypical of commercially available substrates and thick-film techniques, but the resulting aperture distribution error is unlikely to be the simple linear phase shift illustrated in Table 2. Further development work will rely much on trial and error, and as an example the improved performance shown in Fig. 15b and Table 1 column (ii) was achieved by reducing the resonator spacing by about  $16\%$  and utilising empirical curve (ii) of Fig. 11.

The power budgets in Table 1 confirm both the reduction in feeder power loss achieved with the hybrid array concept compared to the use of microstrip lines and the order of the launcher loss. A very important property

Table 1: Power budgets of 90 GHz hybrid linear microstrip patch antennas

	(i)	(ii)
Beamwidth, degrees (theory)	2.15	2.5
(measured)	2.0	2.5
Squint angle, degrees (measured)	-16	-5
Sidelobes, dB (measured)	-9.0 & -11.2	-10.8 & -14.8
Crosspolar, dB (measured)	< -25	< -24
Directivity*, dB	24.2	23.6
Gain, dB (measured)	17	18
Launcher loss, dB (theory)	2.0	2.0
Mismatch loss, dB (measured)	0.04	0.04
Feeder loss†, dB (theory)	2.0	2.0
Resonator loss**, dB (measured)	0.97	0.97
Load loss*, dB	2.19	0.59
Element spacing, mm	2.34	1.96
Efficiency‡, % (assuming no launcher or load loss)	50.0	50.0
Efficiency‡ of microstrip array of same physical size, %	24.9	30.0

\* Directivity =  $10 \log (A/\lambda^2) \cos(\text{squint angle})$  dB,  $A$  = aperture area

† Calculated using 0.05 dB  $A_{\text{eff}}$  over 40 wavelengths

\*\* From measurements on patch resonator  $Q$ -factors

\* (i) Load loss =  $24.2 - (17 + 2 + 0.04 + 2 + 0.97) = 2.19$  dB

(ii) Load loss =  $23.6 - (18 + 2 + 0.04 + 2 + 0.97) = 0.59$  dB

‡ (i) Efficiency =  $24.2 - (17 + 2 + 2.19) = 3.01$  dB = 50%

(ii) Efficiency =  $23.6 - (18 + 2 + 0.59) = 3.01$  dB = 50%

‡ Microstrip feeder of same physical length (39 wavelengths),  $\epsilon_{r1} = 2$ ,  $Z_0 = 50 \Omega$ , line loss = 0.13 dB, patch loss = 0.97 dB

observed with all hybrid antennas using microstrip resonators is the low crosspolarisation levels (see Fig. 15a and b) substantiating that the radiation pattern is firmly con-

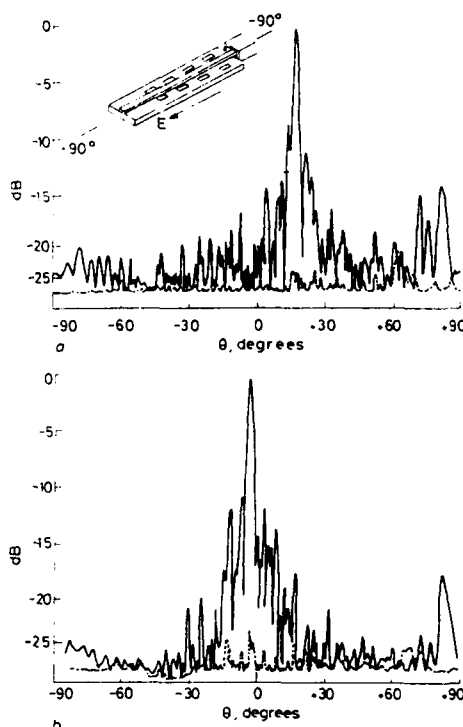


Fig. 15 Radiation pattern of the hybrid antenna at 90 GHz utilising microstrip patch resonators

See Table 1 for power budget

— copolar

- - - crosspolar

a Based on Fig. 11 (i)

b Based on Fig. 11 (ii)

trolled by the microstrip patch radiators. The purity of polarisation confirms that only aperture 2 excitation results in radiation, while radiation due to aperture 1 excitation is largely cancelled by the symmetrical deployment of the microstrip resonators either side of the dielectric slab. Unwanted radiation due to substrate surface-wave generation has not been detected and presumably exists at lower levels than the sidelobes measured. Measurements on other design specifications to date indicate that longer arrays are easier to design and show a greater reduction in feeder loss compared to microstrip feeders.

#### 4 Conclusions

The hybrid microstrip/dielectric antenna concept enables a microstrip linear array to be fed with a low-loss insular guide feeder. The phase constant and losses in the feeder and the microstrip radiator coupling relationship have been computed by various analytical methods to obtain basic antenna design data for the first few modes in the insular guide. Several ways of creating the linear array are considered, but the main interest lies in the use of the  $E_{11}$  dominant insular guide mode coupled to microstrip patch resonator antennas. Some practical results on millimetre linear arrays have been examined, and they demonstrate the feasibility of the hybrid antenna concept, particularly

coupling required to create a given aperture distribution along the linear array. To a first order

$$K_j = \frac{P_j}{P_L + \sum_{i=1}^j P_i} \quad (14)$$

where  $K_j$  and  $P_j$  are, respectively, the fraction of insular guide modal power coupled to the  $j$ th microstrip patch

guide circuits has not yet advanced sufficiently to implement this integration. In the short term, other ways of connecting dielectric guides to conventional waveguides need to be examined, such as gradually coupling over a length of insular guide perhaps through holes in the ground plane [12], but such a launching transition would occupy a relatively large volume.

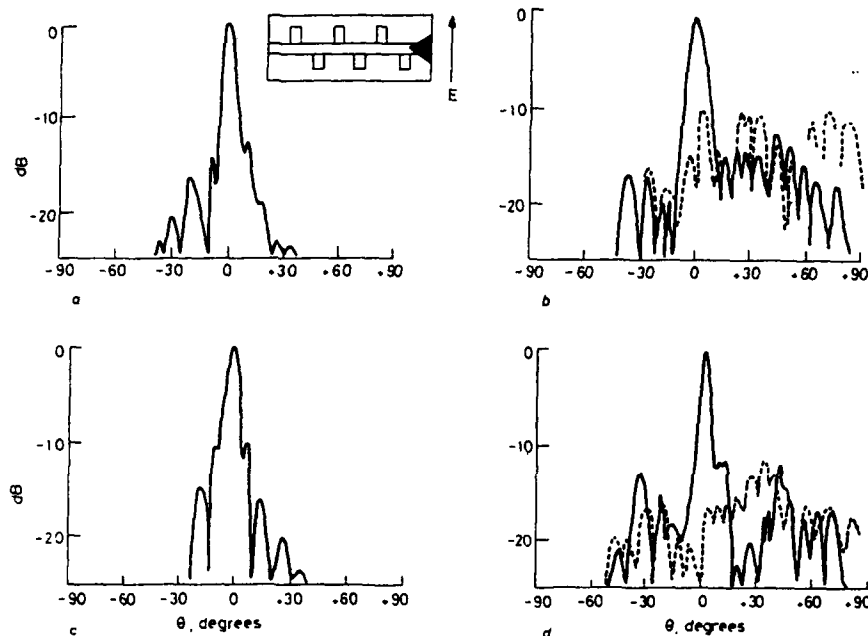


Fig. 13 Radiation patterns of hybrid arrays using narrow lines coupled to  $E_{11}^x$ -mode  
a Travelling-wave array at 14 GHz  
b Resonant array at 14 GHz  
c Travelling-wave array at 70 GHz  
d Resonant array at 70 GHz  
— copolar  
--- crosspolar

and the power radiated by the latter;  $v$  = number of patch elements and  $P_L$  = power absorbed in the load termination for travelling-wave action. The sidelobe level desired determines the relative  $P_j$ -values, and, for a given  $P_L$ ,  $K_j$  is obtained from eqn. 14. The guide loss will slightly modify the distribution. The second-order effects that are not included in the above design are principally dimensional corrections for field fringing on the microstrip patch resonators, perturbation of the insular guide mode by the microstrip patches, a more precise adjustment of  $K_j$  and the polarisation purity of the resulting linear array.

### 3.2 Launcher constraints

The unwanted radiation loss associated with connecting planar microstrip or dielectric linear antennas to the transmit/receive equipment amounts to a field compatibility problem at the transition. The losses have been quantified [8], and a rectangular waveguide to insular guide launching transition could typically have a radiation loss of the order 2 dB. The co- and crosspolarised corruption of the radiation characteristics of the linear antenna can be removed by shielding the launcher with absorbent material, as in the present measurements, but in an operational antenna the launcher loss would negate the lower-loss advantages of the dielectric feeder structure. The ultimate solution is to create the transmit/receive circuits in an insular guide structure which involves the fully integrated antenna concept. However, the design of dielectric

### 3.3 Practical results at millimetre wavelength

Some measured radiation patterns (Fig. 13) for antennas based on the  $E_{11}^x$ -mode and narrow line coupling are briefly noted to illustrate the problems anticipated in Section 2.2. The  $E_{11}^x$ -mode was chosen because the field in the substrate resembled the field underneath a microstrip line and experiments showed that launching from a microstrip stub was feasible at microwaves. At millimetres a waveguide launcher was used. The basic design [13] involved 32 alternating narrow  $\lambda_w/2$  microstrip stubs protruding beneath the dielectric slab. The radiation patterns show a level of crosspolarisation which is presumably due to the perturbation of insular guide fields by the close proximity of the stubs and, possibly, mode conversion. No attempt was made to optimise the aperture distribution in view of the poor manufacturing control brought about by the stubs protruding beneath the dielectric slab. When these narrow microstrip stubs were placed exterior to the slab with  $x_0 > a$ , the coupling levels were far too low to make the linear array design viable.

For  $E_{11}^x$ -mode operation 40 microstrip patches were placed both sides of the dielectric slab as in Fig. 12; the travelling-wave array is shown in Fig. 14. The polarisation of this array is orthogonal to that in Fig. 13. As in the above antenna the substrate  $h = 0.127$  mm,  $\epsilon_r = 2.3$  was chosen from commercially available material to be compatible with efficient microstrip patch radiation. The insular guide dimensions were scaled down from the

mental values. The above results for  $x_0 = a$  show the feasibility of obtaining significant levels of coupling without the microstrip patch protruding under the dielectric slab. A

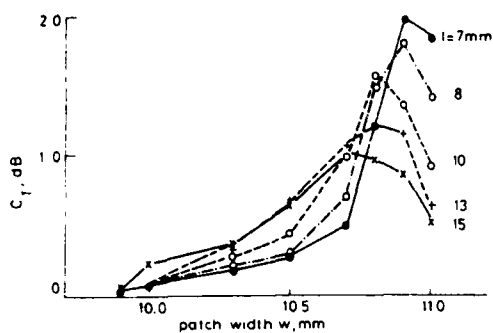


Fig. 10 Measured  $C_T$  around resonance for  $\pm 1, 0$  mode at 8.5 GHz:  $x_0 = a$ ,  $h = 0.79$  mm,  $a = 5$  mm,  $b = 3$  mm,  $\epsilon_{r1} = 2.3$ ,  $\epsilon_{r2} = 10$

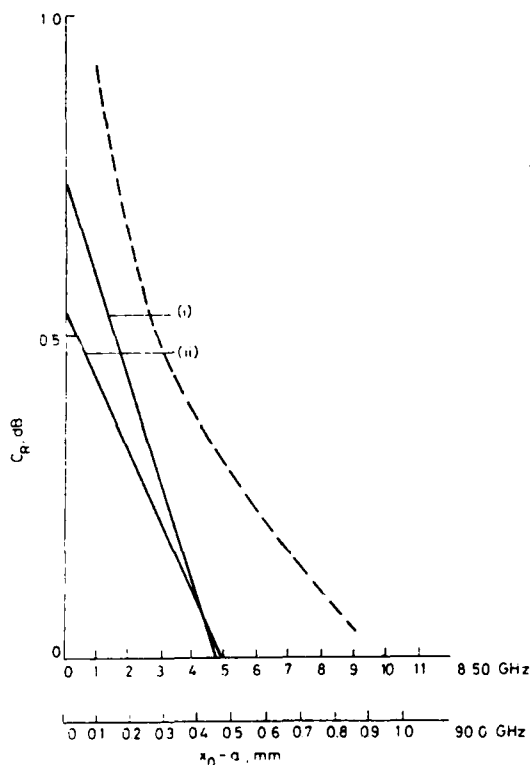


Fig. 11 Computed and empirical curves of  $C_R$  as a function of separation distance  $x_0$

$a = 5$  mm,  $b = 3$  mm,  $w = 11$  mm,  $l = 6$  mm,  $\epsilon_{r1} = 2.3$ ,  $\epsilon_{r2} = 10$   
 $h = 0.79$  mm,  $\epsilon_{r1} = 2.3$ ,  $\epsilon_{r2} = 10$  — computed at 8.5 GHz  
 — empirical curves (i) and (ii) at 9.0 GHz

computed result of  $C_R$  for  $x_0 > a$  is given in Fig. 11, illustrating how various coupling levels from 1.0 to 0.1 dB can be achieved for  $0 < x_0 < 8$  mm for the antenna model at 8.5 GHz.

### 3 Linear antenna array design

The basic design of this hybrid antenna follows the conventional methods for series-fed linear arrays of a

travelling-wave or resonant nature as described elsewhere (see Reference 1, Chap. 5). Consider a long insular guide (see Fig. 12), to which the microstrip patch resonators are coupled. We restrict the design to broadside beams; thus, the coupling process must ensure that the elements radiate with the appropriate cophase relationships. For travelling-wave array action the insular guide is terminated with a load comprising absorbent material in the form of lossy

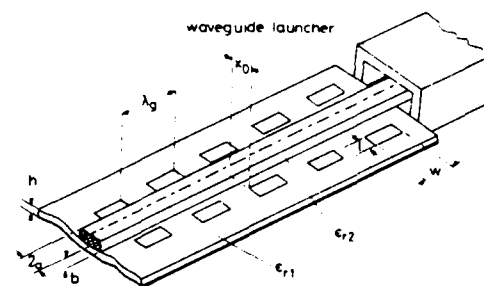


Fig. 12 Layout of hybrid array

paint or thin lossy sheets in contact with the dielectric slab; for resonant array action the insular guide is left unterminated. In practice, it is difficult to achieve either an open-circuit or a short-circuit termination due to radiation loss. For both types of array the insular guide is connected to a waveguide launcher, which in these experiments was an open-ended rectangular waveguide. The radiation loss problems associated with launching have been previously analysed [8], and in the present measurements the launcher is surrounded by absorbent material. There are numerous second-order effects to be considered in an optimised design, particularly if the array is to have low cross-polarisation and/or low sidelobe levels, but our main objective here is to demonstrate the feasibility of the hybrid array concept; details of the main design points are given in the following Sections.

#### 3.1 Control of the aperture distribution

The distance in the  $z$ -direction between the microstrip patch radiators of Fig. 12 is determined by the insular guide wavelength  $\lambda_g$ , which, in turn, is a function of the particular mode selected in Fig. 2. In reality, the use of a higher-order mode invokes difficult mode launching problems and possible mode conversion at each radiating microstrip element.  $E_{11}^y$  has the lowest loss (see Fig. 4) and is free from the above mode purity problems if the insular guide dimensions are such that higher modes are cut off. Some results for the  $E_{11}^y$ -mode are presented below, but we confine our interest to the  $E_{11}^y$ -mode with  $\lambda_g$  selected for single-mode operation (see Fig. 2) and minimum guide loss (see Fig. 4). Otherwise, the coupling mechanism appears to be reasonably tolerant to the choice of dielectric slab dimensions. The next design issue is the microstrip patch spacing for a broadside beam. If the microstrip patch (Appendix 7.4) radiates predominantly from the end regions at  $z = 0$  and  $z = w$  due to aperture 2 excitation, then  $\lambda_g$  spacing of resonators on one or both sides of the guide is appropriate; whereas radiation from the other two patch terminal regions due to aperture 1 excitation would allow  $\lambda_g/2$  spacing in an alternate fashion on either side of the guide. However, for the practical cases considered, the latter spacing is not feasible for wide microstrip resonators and  $\lambda_g$  spacing is chosen. Finally, the  $x_0$ -value for each patch is selected from Fig. 11 for the degree of power

where

$$X_m = C_m \frac{\sin(\bar{k}_{xm}h)}{\bar{k}_{xm}h} \exp[-\bar{k}_{xm}(x_0 - a)]$$

The cavity mode coefficients generated by aperture 2 depend only on  $q$ , and we denote  $B_{pq}$  by  $B_q$ :

$$B_q = \frac{2}{(1 + \delta_{q0})l} k^2 \beta \sum_{m=1}^M \bar{k}_{xm} X_m \frac{-1}{\bar{k}_{xm}^2 + (q\pi/l)^2} \times [1 - (-1)^q \exp(-\bar{k}_{xm}l)] \quad (11)$$

where  $\delta_{ij}$  is the Kronecker delta defined as

$$\delta_{ij} = 0 \quad i \neq j$$

$$\delta_{ij} = 1 \quad i = j$$

The complete form of the modal coefficient is  $B_{pq} = B_p + B_q$ :

$$B_{pq} = -k^2 \beta \sum_{m=1}^M \bar{k}_{xm} X_m \left[ \frac{2}{(1 + \delta_{p0})w} \frac{[1 - (-1)^p \cos(\beta w)]}{(p\pi/w)^2 - \beta^2} + \frac{2}{(1 + \delta_{q0})l} \frac{[1 - (-1)^q \exp(-\bar{k}_{xm}l)]}{(q\pi/l)^2 + \bar{k}_{xm}^2} \right] \quad (12)$$

The patch fields are then obtained by substituting for  $B_{pq}$  from eqn. 12 into eqn. 9. An experiment (see Appendix 7.3) was performed to relate variations in  $w$  and  $l$  while maintaining resonance conditions in the patch, and the results are shown in Fig. 8. Examination of computations of eqn. 12 show that, around resonance, distinct  $p$ - and  $q$ -values dominate the behaviour as may be expected.

The percentage of incident insular guide power coupled to the patch is  $C_T = 100 \times (P_d + P_c + P_R)/P_I$ ; the percentage of incident insular guide power coupled to radiation is  $C_R = 100 \times (P_R/P_I)$ ; and the radiation efficiency of the patch antenna is  $100 \times P_R/(P_d + P_c + P_R)$ , where  $P_d$ ,  $P_c$  and  $P_R$  are the power losses due to patch dielectric loss,

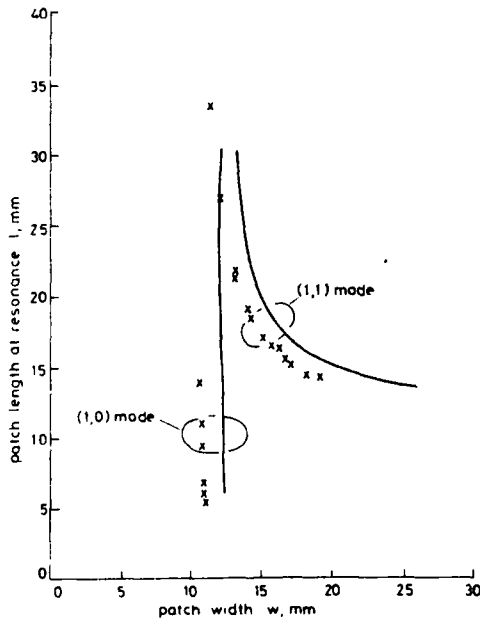


Fig. 8 Relationship between patch length  $l$  and width  $w$  at resonance  
 $\epsilon_0 = \epsilon_1$ ,  $h = 0.79$  mm,  $a = 5$  mm,  $b = 3$  mm,  $\epsilon_1 = 2.3$ ,  $\epsilon_2 = 10$ , frequency = 8.5 GHz  
— theory  
x experiment

patch conduction loss and radiation, respectively. These are given in Appendix 7.4. To embrace these losses within the cavity fields, eqn. 9, the total power loss is equated to a fictitious lossy dielectric substrate having an effective loss tangent  $\tan \delta_{eff}$ . The relative permittivity  $\epsilon_{r1}$  in eqn. 9a is replaced by

$$\epsilon_{r1}(1 - j \tan \delta_{eff})$$

where

$$\tan \delta_{eff} = 1/Q_T = 1/Q_d + 1/Q_c + 1/Q_R$$

$$Q_d = 1/\tan \delta$$

$$Q_c = h(\pi f_r \mu_0 \sigma)^{1/2}$$

$$Q_R = \frac{\pi^2 \delta_{r1}}{2k} \frac{w}{h} \frac{(1 + \delta_{p0})}{2} \frac{(1 + \delta_{q0})}{2} \frac{1}{l(\theta, \phi)}$$

The substrate loss tangent =  $\tan \delta$ ,  $\sigma$  = conductivity of patch copper conductor and  $l(\theta, \phi)$  = integral arising from calculation of radiation power given in Appendix 7.4. For the substrates of interest, radiation is the dominant loss since  $Q_R \ll Q_d, Q_c$ .

Some results for the power coupled into a microstrip patch for various  $w$ - and  $l$ -values (see Fig. 9) show the pro-

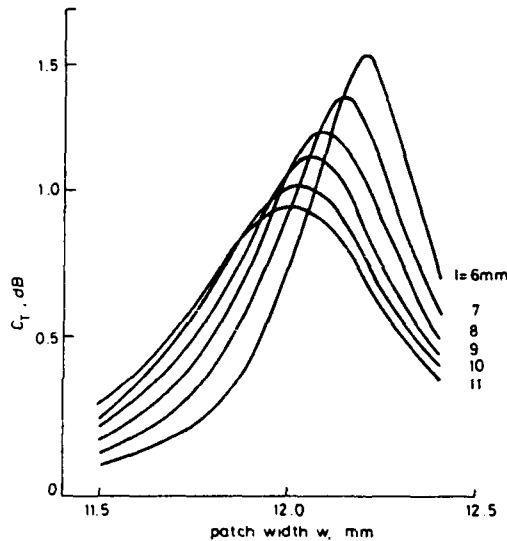


Fig. 9 Computed  $C_T$  around resonance for  $(1,0)$  mode at 8.5 GHz  
 $\epsilon_0 = \epsilon_1$ ,  $h = 0.79$  mm,  $a = 5$  mm,  $b = 3$  mm,  $\epsilon_1 = 2.3$ ,  $\epsilon_2 = 10$

nounced resonance behaviour when  $w$  is somewhat greater than  $\lambda_m/2$  and  $l \approx \lambda_m/4$ , where  $\lambda_m \approx \lambda_0/\sqrt{\epsilon_{r1}}$ , but, as  $l$  tends to  $\lambda_m/2$ , less power is coupled to radiation and the resonance occurs for a slightly smaller  $w$ -value. The superior coupling when  $l \approx \lambda_m/4$  is likely to be due to optimal matching whereby the high impedance radiating aperture at  $x_0 = x + l$ ,  $0 \leq y \leq h$ ,  $0 \leq z \leq w$  transforms by quarter-wave action to a low impedance in aperture 1, compatible with the excitation impedance levels. The computations shown in Fig. 9 are based on the dominant modes at and around the resonant frequency. Experimental results for coupling using the measurement methods outlined in Appendix 7.3 at microwaves are presented in Fig. 10, and they closely resemble the behaviour predicted in Fig. 9. Field fringing around the patch and the proximity effects of the dielectric slab have not been included in the analysis, and the computed results of both Figs. 8 and 9 predict slightly larger patch dimensions than the experi-

The highest bandwidth ratio (M) was obtained with the three layer antenna <sup>11</sup>, Figure 8(q), where M = 16.4 compared to M = 7 for the 5 element antennas of Figures 8(k) and 8(n). For about half the complexity although the vertical parasitic antennas achieved their higher bandwidth at the expense of much greater volume. Vertical parasitic antennas also achieved roughly twice the values of M for a doubling in the complexity compared to multi-element lateral parasitic antennas.

Vertically spaced parasitic antennas have the problem that with an increasing number of parasitic elements the coupling reduces with increasing distance from the driven element and the reflector. In the same way the bandwidth increase (M) for vertical parasitic patches follows a diminishing return law with increasing height and complexity. Indeed this was a problem with the three layer antenna <sup>11</sup> Figure 8(q). The two layer antenna in Figure 8(p) had a square driving resonator, but to achieve sufficient coupling to the third layer in the three layer arrangement, Figure 8(q), the aspect-ratio (w/l) of the driven patch had to be increased by 15% thus increasing its radiation conductance.

---

Footnotes:

NOTE 1

M = Bandwidth ratio

$$= \frac{\left( \begin{array}{l} \text{Bandwidth of antenna employing some device to achieve broadband} \\ \text{operation} \end{array} \right)}{\left( \begin{array}{l} \text{Bandwidth of single or driven element without any broadbanding} \\ \text{device.} \end{array} \right)}$$

NOTE 2

FEGCOMA <sup>19</sup> - Four edge gap coupled open microstrip antenna, Figure 8(k).

FEDCOMA <sup>19</sup> - Four edge direct coupled open microstrip antenna, Figure 8(n).

NEGCOMA <sup>19</sup> - Non-radiating edge gap coupled open microstrip antenna, Figure 8(i).

NOTE 3

C = Degrees of freedom

A single microstrip patch has 3 degrees of freedom, length ( $l$ ), width ( $w$ ) and substrate height ( $h$ ):  $C = 3$ .

A 3-element lateral parasitic element like that in Figures 8(i and j) has 9 degrees of freedom; that is 3 x patch length ( $l$ ) + 3 x patch width ( $w$ ) + substrate height ( $h$ ) + 2 x inter-element gap width:  $C = 9$ .

NOTE 4

$V_p/V$  = Increase in antenna volume.

$$\frac{\left( \begin{array}{l} \text{Volume of antenna employing some device to achieve broadband} \\ \text{operation.} \end{array} \right)}{\left( \begin{array}{l} \text{Volume of single or driven element without any broadbanding} \\ \text{device} \end{array} \right)}$$

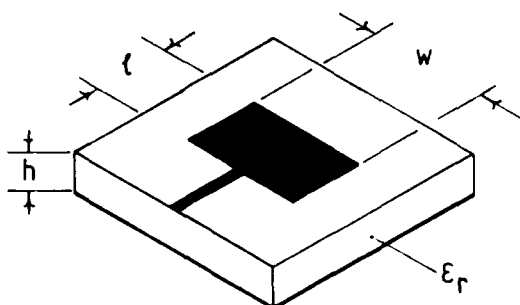


Figure 1: Rectangular microstrip patch radiating element.

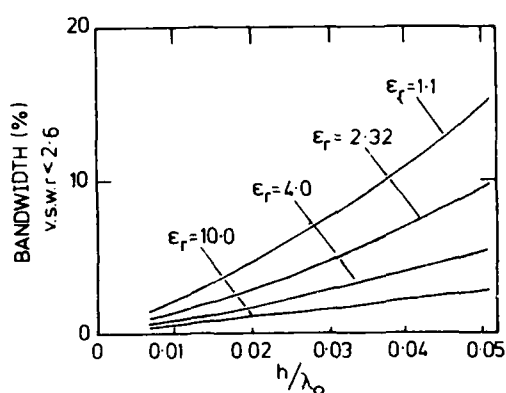
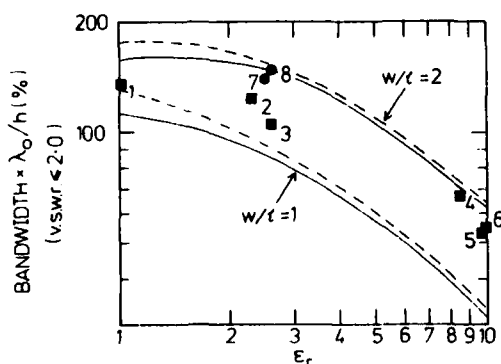


Fig 2(a): Relationship between bandwidth, substrate thickness and substrate dielectric constant (James and Henderson<sup>3</sup>)



- 1 Penard<sup>27</sup>
- 2 Hall<sup>12</sup>
- 3 Howell<sup>10</sup>
- 4 Howell<sup>10</sup>
- 5 Hall<sup>12</sup>
- 6 Howell<sup>10</sup>
- 7 Poddar<sup>14</sup>
- 8 Howell<sup>10</sup>

$w/l = 1$  (measured)  
 $w/l = 2$  (measured)  
 — James<sup>2</sup> (theory)  
 --- Pues<sup>4</sup> (theory)

Figure 2 (b): Relationship between bandwidth, substrate dielectric constant and patch aspect - ratio with experimental results of various workers.

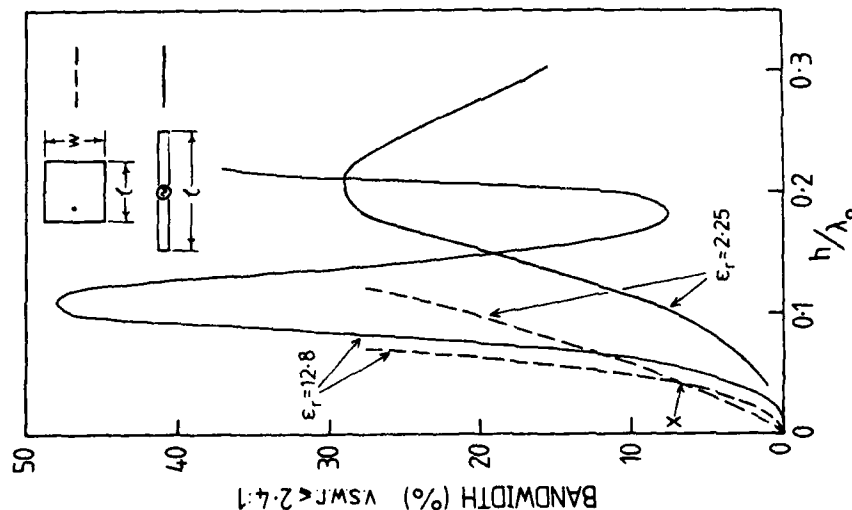


Fig 3: Comparison between the theoretical bandwidths of square microstrip patch and thin dipole elements on thick substrates (Pozar<sup>5</sup>)

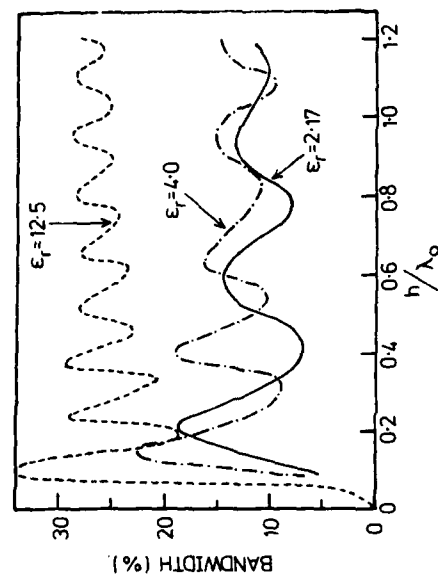


Fig 4(a): The theoretical effect of substrate dielectric constant on the available bandwidth of thin dipole elements on thick substrates (Alexopoulos et al<sup>8,9</sup>)

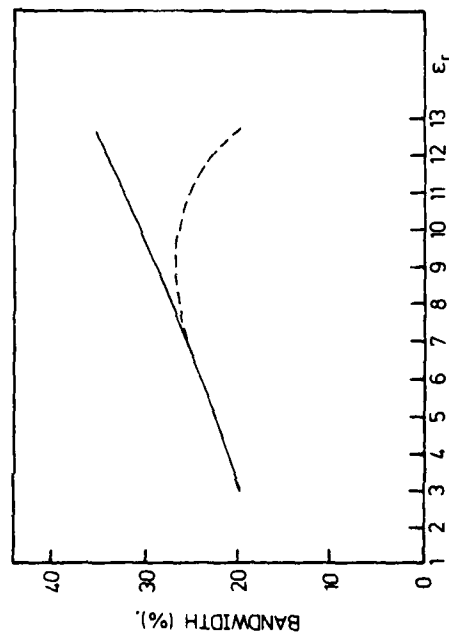


Fig 4(b): Theoretical relationship between maximum bandwidth, bandwidth for maximum radiation efficiency and substrate dielectric constant for thin dipole elements on thick substrates (Alexopoulos et al<sup>9</sup>)



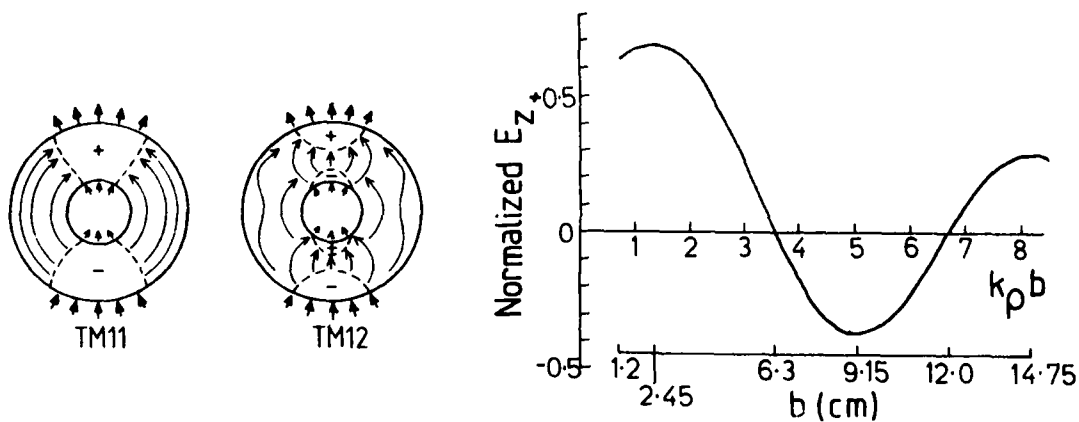


Figure 5 (a): Schematic representations of TM<sub>11</sub>, TM<sub>12</sub> annular-ring modes.

Figure 5 (b): Theoretical variation of  $E_z$  with normalized radial distance  $z/b$  for an annular ring antenna using a specific case;  $a = 1.2$  cm,  $k = 0.5617$  and  $f = 1.8$  GHz (Das and Mathur<sup>23</sup>)

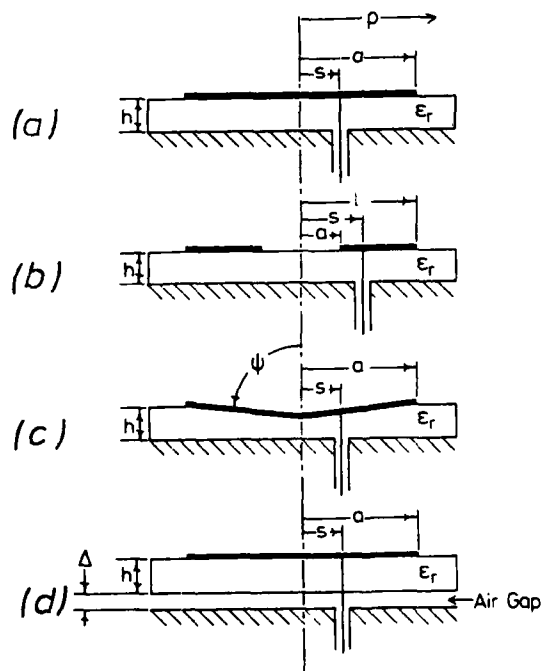


Figure 6: Schematic representations of various disc and annular ring configurations; (a) Disc, (b) Annular-ring, (c) conically depressed disc (Das and Chatterjee<sup>21</sup>) and (d) Air-spaced disc (Lee et al<sup>24</sup> and Ness Young<sup>25</sup>).

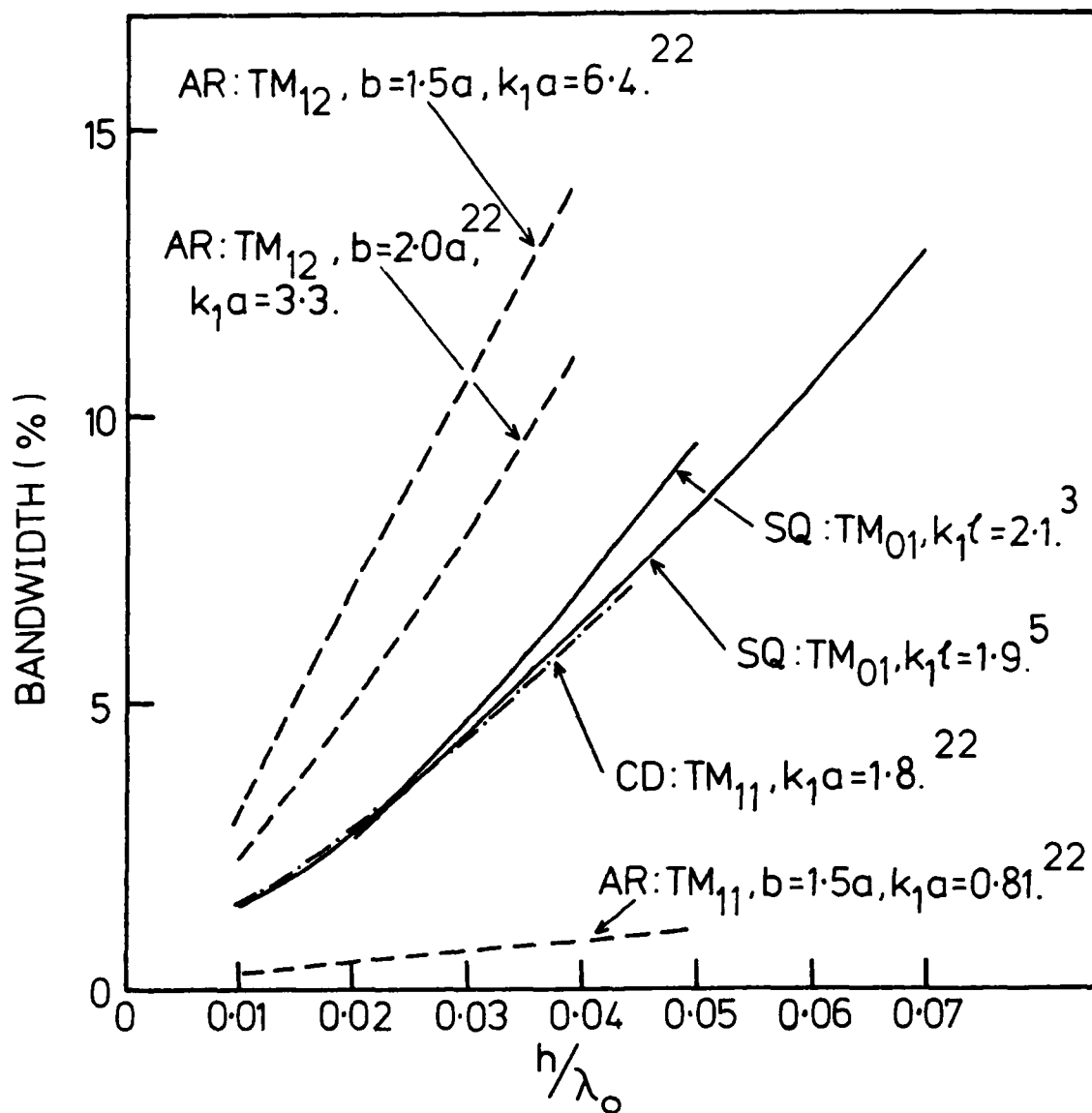


Fig 7: Theoretical comparison of the bandwidth of square (SQ), circular-disc (CD) and annular-ring (AR) radiating elements: various workers.

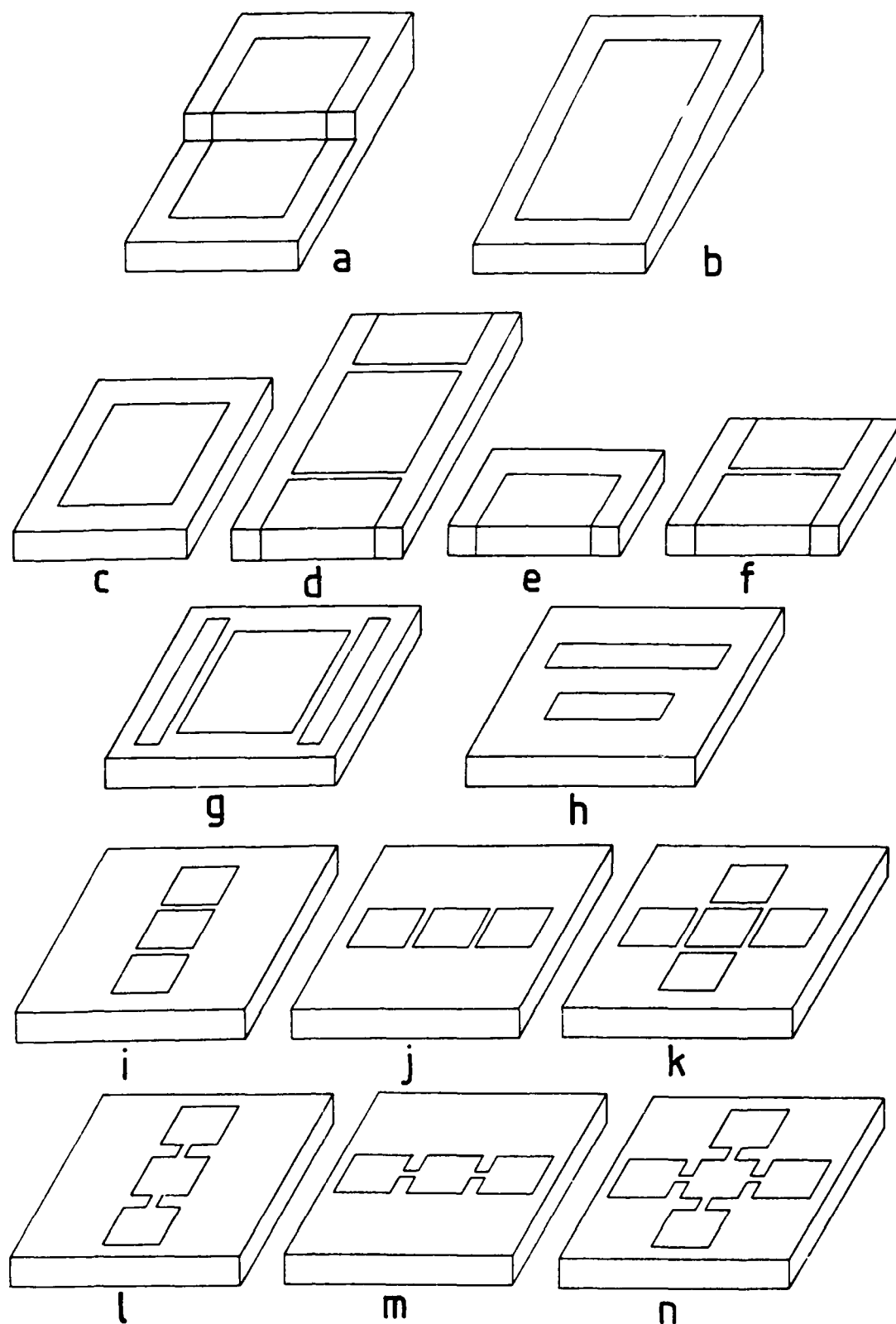


Fig 8: Schematic representations of the various lateral and vertical parasitic element radiating elements considered.

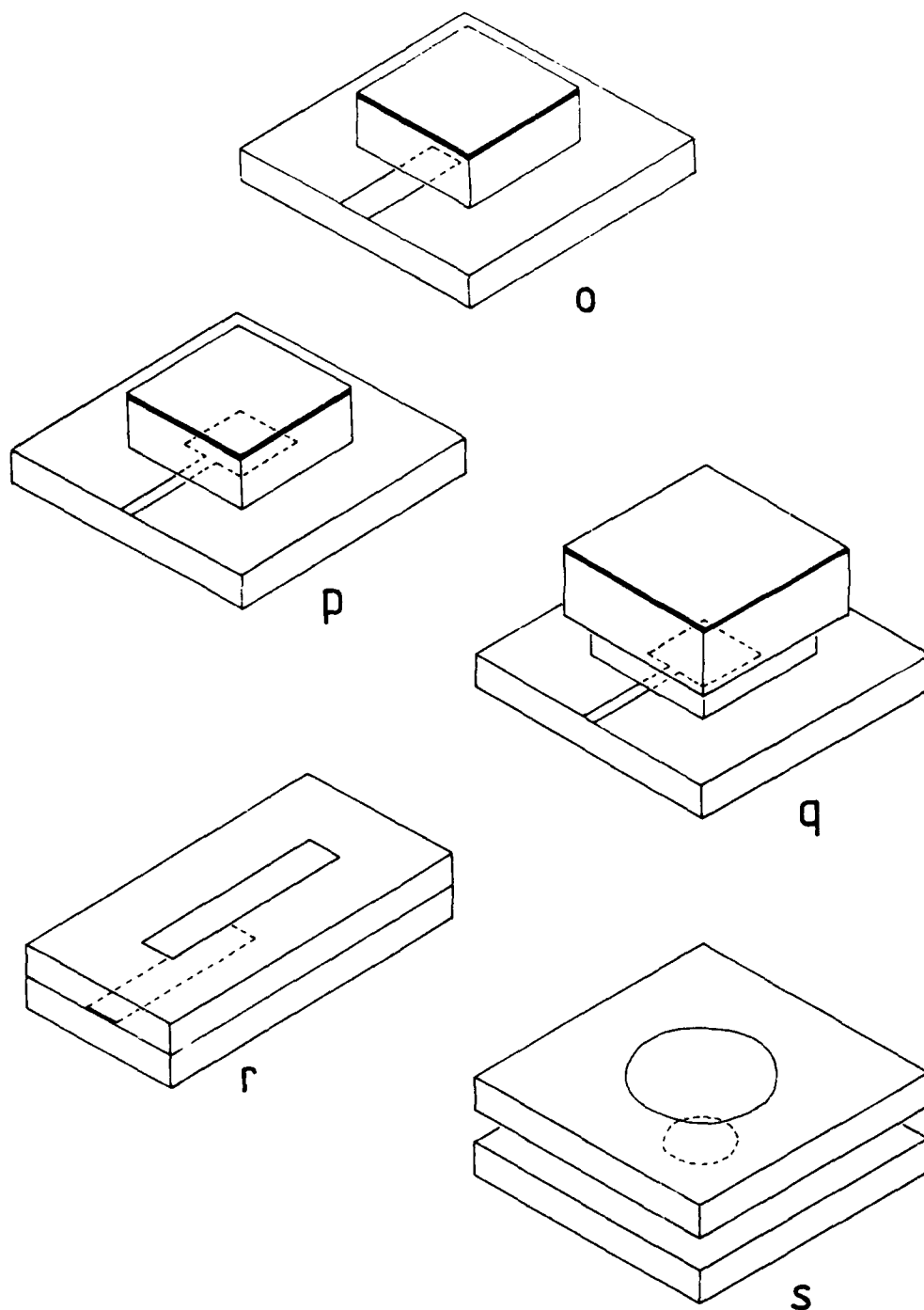


Fig 8: (cont'd)

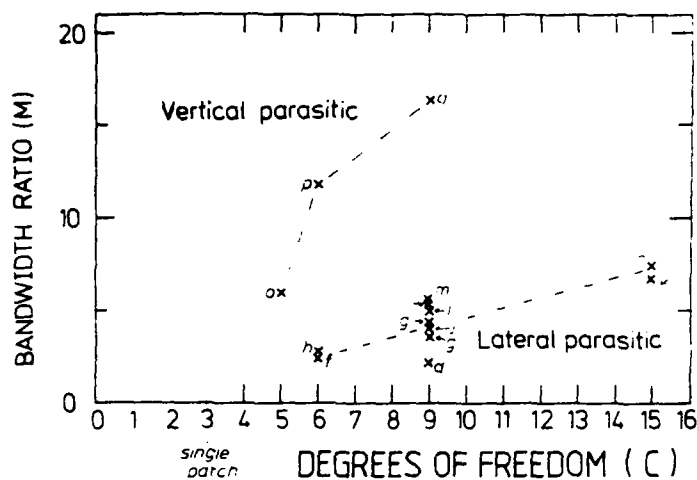


Fig 9: Relationship between increase in bandwidth (M: see note 1) and degrees of freedom (C: see note 3), comparing lateral and vertical parasitic elements. (Letters indicate corresponding elements in Fig 8)

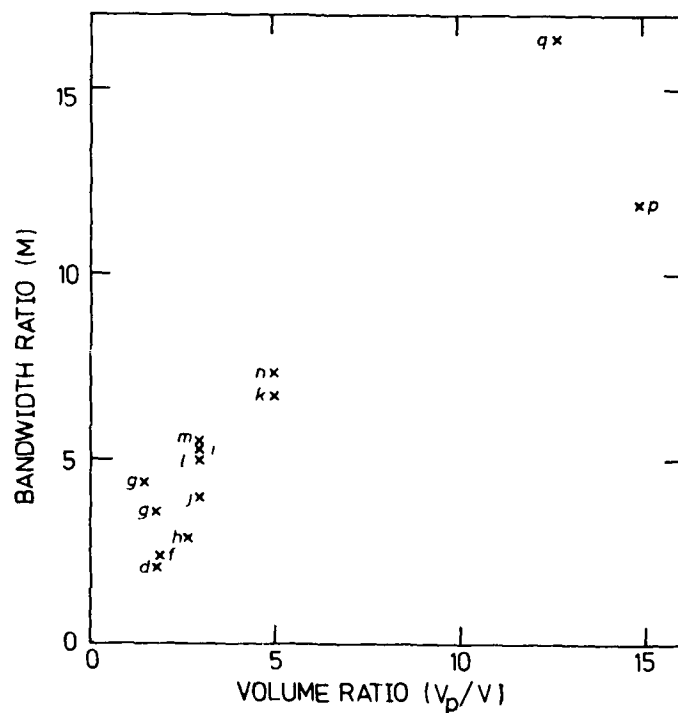


Fig 10: Relationship between increase in bandwidth (M: see note 1) and increase in antenna volume ( $V_p/V$ : see note 4). (Letters indicate corresponding elements in Fig 8).

#### 8.4.5 References relevant to microstrip bandwidth survey

1. Aitken, J. E., 'Swept-frequency microwave Q-factor measurement', Proc. IEE, Vol. 123, Pt.H, No. 9, p. 855-862, Sept. 1976.
2. James, J. R., Hall, P. S. and Wood, C., 'Microstrip antennas, theory and design', Peter Perigrinus Ltd. (IEE, London, England), 1981.
3. James, J. R., Henderson, A. and Hall, P. S., 'Substrate constraints on microstrip antenna performance', Microwave Syst. News, p. 73-84, August 1982.
4. Pues, H, and Van de Capelle, A., 'Functional dependence of the bandwidth and gain of a rectangular microstrip antenna on its structural parameters', Proc.IEEE 1981, Int. Symp. on Antennas and Propag., p. 77-80.
5. Pozar, D. M., 'Considerations for millimetre-wave printed antennas' IEEE Trans., Vol. AP-31, No. 5, p. 740-747, Sept. 1983.
6. Carver K. R. and Mink, J. W., 'Microstrip antenna technology', IEEE Trans., Vol. AP-29, No. 1, p. 2-24, Jan. 1981.
7. Katehi, P. B. and Alexopoulos, N. G., 'On the effect of substrate thickness and permittivity on printed circuit dipole properties', Proc. IEEE, 1981, Int. Symp. on Antennas and Propag., p. 70-73.
8. Alexopoulos, N. G., and Katehi, P. B. and Rutledge, D. B., 'Substrate optimization for integrated circuit antennas', IEEE, 1982, MTT-Symp., Digest, p. 190-192.
9. Alexopoulos, N. G., Katehi, P. B. and Rutledge, D. B., 'Substrate optimization for integrated circuit antennas', IEEE Trans, Vol. MTT-31, No. 7, p. 550-557, July 1983.
10. Howell, J. Q., 'Microstrip antennas', IEEETrans, Vol AP-23, No. 1, p. 90-93, Jan 1975.
11. Hall, P. S., Wood, C. and Garrett, C., 'Wide bandwidth microstrip antennas for circuit integration', Electron. Lett. (GB, Vol. 15, No. 15, p. 458-459, July 1979.
12. Wood, C., 'Improved bandwidth of microstrip antennas using parasitic elements', IEEE Proc., Vol. 127, Pt. H, No. 4, p. 458-459, August 1980.
13. Oltman, H. G. and Heubner, D. A., 'Electromagnetically coupled microstrip dipoles', IEEE Trans., Vol. AP-29, No.1, p. 151-157, Jan. 1981.
14. Poddar, D. R., Chatterjee, J. S. and Chowdhury, S. K., 'On some broadband microstrip resonators', IEEE Trans., Vol. AP-31, No. 1, p. 193-194, Jan 1983.
15. Schaubert, A. and Farrar, F. G., 'Some conformal, printed circuit antenna designs', Proc. Workshop on Printed Antenna Technology, New Mexico State Univ., Las Cruces, New Mexico, Oct. 17-19, 1979, p. 5, 1-21.

16. Derneryd, A. G. and Lind, A. G., 'Cavity model of the rectangular microstrip antenna', op. cit., p.12, 1-11.
17. Dahele, J. S. and Lee, K. F., 'Top-loaded single and coupled microstrip monopoles', Proc. IEEE, 1983, Int. Symp. on Antennas and Propag, Vol. 1, p47-50, Houston, TX., USA, May 23-26, 1983.
18. Sabban, A., 'A new broadband stacked two layer microstrip antenna', op. cit., p. 63-66.
19. Kumar, G. and Gupta, K. C., 'Broadband microstrip antennas using coupled resonators', op. cit., p. 67-70.
20. Griffin, J. M. and Forrest, J. R., 'Broadband circular disc microstrip antenna', Electron. Lett. (GB), Vol. 18, No. 6, p. 266-269, 18 March 1982.
21. Das, N. and Chatterjee, J. S., 'Conically depressed microstrip patch antenna', IEEE Proc., Vol 130, Pt. H, p.193-196, April 1983.
22. Chew, W. C., 'A broadband annular ring microstrip antenna', IEEE Trans, Vol. AP-30, No. 5, p. 918-922, Sept. 1982.
23. Das, A., Das, S. K. and Mathur, S. P., 'Radiation characteristics of higher-order modes in microstrip ring antenna', IEEE Proc., Vol. AP-131, Pt. H, No.2, p. 102-106, April 1984.
24. Lee, K. F., Ho, K. Y. and Dahele, J. S., 'Circular-disc microstrip antenna with air gap', IEEE Trans., Vol. AP-32, No. 8, p. 880-883, August 1984.
25. Lier, E., 'Comments on "On some broadband microstrip resonators" and reply', IEEE Trans., AP-32, No. 8, p.890-891, August 1984.
26. Ness, J. and Young, R., 'Two-layer circularly polarised microstrip antenna', Electron. Lett. (GB), Vol. 20, No. 4, p. 181, 182, 16 Feb. 1984.
27. Penard, E. and Daniel, J. P., 'Open and hybrid microstrip antennas', IEEE Proc., Vol. 131, Pt-H, No. 1, p. 38-44, Feb. 1984.

Appendix 8.5

Crosspolarization Behaviour of Series-Fed  
Microstrip Linear Arrays <sup>15</sup>



# Crosspolarisation behaviour of series-fed microstrip linear arrays

P.S. Hall, B.Eng., M.Eng., Ph.D., C.Eng., M.I.E.E., and Prof. J.R. James, B.Sc., Ph.D., D.Sc., F.I.M.A., C.Eng., F.I.E.R.E., F.I.E.E.

Indexing terms: Antennas; Microwave systems

**Abstract:** Crosspolarisation effects in microstrip antenna arrays have received little attention to date, and the purpose of this paper is to identify sources of crosspolarisation and quantify design parameters for a wide variety of radiating structures suitable for use in series-fed arrays. Surface wave effects and radiation from connectors and feed transitions are included as additional factors. Chain, rampart, comb, serpent-line and patch array antennas are some of the types examined, and it is concluded that a magnetic source radiation model having two degrees of positional freedom allows generation of useful first-order design data for all structures. To obtain a more accurate assessment, second-order effects pertaining to the specific radiating structure must be included, and this is illustrated for the comb-line antenna. The constraints imposed by the two degrees of positional freedom and the necessity to trade the overall comb-line antenna performance in order to optimise the crosspolarisation characteristics are particular conclusions which are likely to hold for all types of microstrip antenna.

## List of principal symbols

$a, b$	= coaxial line inner and outer radius, respectively
$c, c_1$	= contour round microstrip and tangent to contour, respectively
$C_p, C_s$	= peak cross- to broadside reference polarisation ratios for one array period and for the complete array, respectively
$E_x, E_y, E_{z_{\text{rad}}}, E_{x_{\text{ref}}}, E_{y_{\text{ref}}}$	= electric fields
$F(\theta, \phi)$	= array factor
$G$	= array power gain
$G_p, G_r, G_i$	= radiation conductances for single period region, microstrip open end and input transition, respectively
$G_s$	= surface wave generation conductance
$h, h_a, h_d$	= substrate height, actual and effective dielectric constant, respectively
$k_0, k_{\text{ms}}, k_{x1}, k_{x2}$	= free-space, waveguide mode and surface wave numbers, respectively
$K$	= $e^{-j k_0 R} / 4_0 R$
$l, l_1, l_2, d_1, d_2, d_3, p, \rho, x, s$	= parameters defining array geometry (see Figs. 1A and B and 3)
$l_0, l_m$	= free-space and microstrip wavelength, respectively
$M, M_d$	= magnetic current
$\hat{n}$	= unit vector
$N$	= number of radiating periods in array
$P_L, P_R$	= ratio of power lost in load to array input power and array element radiated power to incident power on element, respectively
$\Phi$	= reference linear polarisation direction

## Q

$(R, \theta, \phi)$	= spherical co-ordinates
$(\hat{R}, \hat{\theta}, \hat{\phi})$	= unit vectors
$r, \psi, \dots$	= parameters defining dipole position and orientation (see Figs. 2A and B)
$S_p, S_s$	= ratio of surface wave generation to radiation for single radiating element and for complete array, respectively
$T$	= ratio of transition to open-circuit end radiation conductances
$\tau_{mn}$	= modal transmission coefficients
$V$	= microstrip-line voltage
$w, w_1, w_2$	= microstrip-line widths
$w_{\text{eff}}, w_{x1}, w_{x2}$	= effective microstrip-line widths
$w_{\text{eff}}$	= effective triplate-line width
$(x, y, z)$	= Cartesian co-ordinates
$Z_m, Z_t, Z_0$	= microstrip line, triplate line and free-space impedances, respectively

= number of radiating elements in array  
 = spherical co-ordinates  
 = unit vectors  
 = parameters defining dipole position and orientation (see Figs. 2A and B)  
 = ratio of surface wave generation to radiation for single radiating element and for complete array, respectively  
 = ratio of transition to open-circuit end radiation conductances  
 = modal transmission coefficients  
 = microstrip-line voltage  
 = microstrip-line widths  
 = effective microstrip-line widths  
 = effective triplate-line width  
 = Cartesian co-ordinates  
 = microstrip line, triplate line and free-space impedances, respectively

## 1 Introduction

The control of crosspolarisation in well established antennas is generally difficult because it is dependent on many design parameters that have already been determined to optimise other aspects of antenna performance such as bandwidth and sidelobe level. Clearly compromises [1] may have to be made in the overall performance if crosspolarisation is a consideration. It is then important to understand thoroughly and quantify how crosspolarisation relates to the other performance factors. The crosspolarisation behaviour of microstrip antennas is now becoming an important issue, and some performance relationships have been quantified for the rectangular microstrip patch antenna [2]. The aim of this paper is to identify, and, where possible, quantify the factors affecting crosspolarisation in series-fed microstrip array antennas, and to illustrate the findings with results from one particular antenna: the comb-line array. A sketch of the main features of a series-fed array is given in Fig. 1A. The array may be terminated in a matched load as shown to form a travelling-wave array or left open-circuited to produce a resonant array. The wide variety of geometries that can be

Paper 1274H (E11-E12), received 9th January 1984.

The authors are with the Department of Electrical and Electronic Engineering, Royal Military College of Science, Shrivenham, Swindon SN6 8LA, England.  
 \* Controller HMSO, London, 1984.

IEE PROCEEDINGS, Vol. 131, Pt. H, No. 1, AUGUST 1984

247

used for the radiating structure are illustrated in Fig. 1B. Whilst two-dimensional arrangements of these or other linear configurations may give improved crosspolarisation performance, this paper is confined to the linear arrays of Figs. 1A and B only.

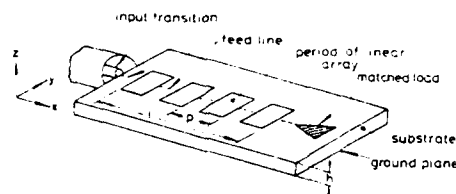


Fig. 1A Schematic of travelling-wave series-fed linear microstrip array and salient design parameters

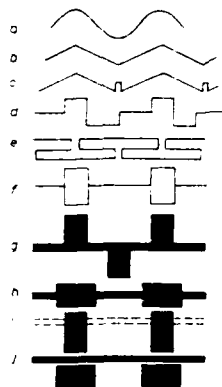


Fig. 1B Forms of array structure

- a Serpentine line [3]
- b Triangle line [4]
- c Circularly polarised chain antenna [5]
- d Rampart line [6]
- e Franklin antenna [7]
- f Linearly polarised chain antenna [8]
- g Comb line [9]
- h Series-connected patch array [10]
- i Overlaid patch array [11]
- j Parasitic patch array [12]

Radiation in microstrip occurs at any discontinuity in the line, such as smooth or abrupt bends, step changes in width and open or short circuits [13]. These generic radiator types are the basis of the various forms of array structures illustrated in Fig. 1B. Crosspolarisation, and, to a lesser extent, sidelobe level, efficiency and bandwidth of series-fed antennas, are dependent on a radiating structure geometry which is constrained within the surface of the substrate to two geometrical degrees of freedom, namely the  $x$  and  $y$  directions (see Fig. 1A). Crosspolarisation is also affected by unwanted radiation from the input feed transition, feed-line termination and substrate surface wave scattering [2]. All of these aspects are determined to some extent by the substrate relative permittivity  $\epsilon_r$  and thickness  $h$ . Additional details are summarised in Table 1 to illustrate the interrelationships between the various design parameters. The scope of the present text is limited to those parameters that relate directly to crosspolarisation, although some brief mention of the other performance factors is made.

The sequence of the text is as follows: the sources of crosspolarisation due to geometry, transition and surface wave effects are identified in Section 2. Geometrical effects are then critically examined in Section 3, with respect to the various types of series-fed antennas of interest, to produce a first-order assessment of their crosspolarisation performance. Detailed analytic and measured results for the comb-line array in Section 4 show how further refinements to the calculation of crosspolarisation performance can be obtained by analysing a specific structure. In Section 5, some final conclusions are drawn, and an Appendix containing supporting details then follows.

Table 1: Main design parameters associated with the performance of series-fed microstrip arrays

Performance aspect	Design parameter
Crosspolarisation	Radiating structure geometry
	Unwanted radiation from <ul style="list-style-type: none"> <li>(a) feed transitions and terminations [13, 14]</li> <li>(b) surface wave scattering [15]</li> </ul>
Sidelobe level	Amplitude taper [16]
	$l$ [16] $p$ [16] Radiating structure geometry [17]
Efficiency	Unwanted radiation from <ul style="list-style-type: none"> <li>(a) and (b) above</li> </ul>
	$l$ [16] $p$ [16] $\epsilon_r$ and $h$ [2, 18] $Z_{in}$ [9] $G_{\Sigma}$ (= function of radiating structure geometry) [16]
Bandwidth	$l$ [9] $p$ [9] $\epsilon_r$ and $h$ [2, 9] $Z_{in}$ [9] Radiating structure geometry [17]

$l$  = array length (see Fig. 1A)

$p$  = period length

$\epsilon_r$ ,  $h$  = substrate dielectric constant and height, respectively

$Z_{in}$  = microstrip feed-line impedance

$G_{\Sigma}$  = radiation conductance representing total radiation from the discontinuities in a single-period region

## 2 Sources of crosspolarisation

### 2.1 Polarisation characteristics of array structures

Radiation from microstrip structures may be analysed in terms of a current source distribution at the substrate surface, where the equivalence principle [19] indicates that the source is in this case a magnetic current distribution given by

$$\mathbf{M} = \mathbf{E}_t \times \hat{\mathbf{n}} \quad (1)$$

where  $\mathbf{E}_t$  is the surface electric field,  $\hat{\mathbf{n}}$  is a unit vector normal to the surface and  $h/\lambda_0 \ll 1$ , where  $\lambda_0$  is the free-space wavelength. Since  $\mathbf{E}_t$  is only significant over a filamentary area close to the edge of the strip,  $\mathbf{M}$  reduces to a magnetic line current. The radiated field  $\mathbf{E}_{rad}$  is then given by [20]

$$\mathbf{E}_{rad} = jhK \left[ \hat{\mathbf{R}} \times \int_{-\infty}^{\infty} \mathbf{M} e^{jk_0 \mathbf{r} \cdot \mathbf{c}} dc \right] \quad (2)$$

where  $r$ ,  $w$  and  $c$  are defined in Fig. 2A,  $\hat{\mathbf{R}}$  is a unit vector in the direction to the far-field point,  $k_0$  is the free-space wave number,  $K = e^{-j\pi/4}/\lambda_0 R$ , and it is assumed that  $\mathbf{E}_t = \tau \hat{\mathbf{c}}$ , where  $\tau$  is the voltage at the conductor edge. This method has been applied to patch antennas [21, 22] and to radiation from curved lines [23], and can thus be applied to the arrays shown in Fig. 1B. Further simplifica-

AD-A158 313

INVESTIGATIONS AND COMPARISONS OF NEW TYPES OF  
MILLIMETRE-WAVE PLANAR ARR. (U) ROYAL MILITARY COLL OF  
SCIENCE SHRIVENHAM (ENGLAND) J R JAMES ET AL. APR 85

2/2

UNCLASSIFIED

DAJA45-83-C-0054

F/G 9/1

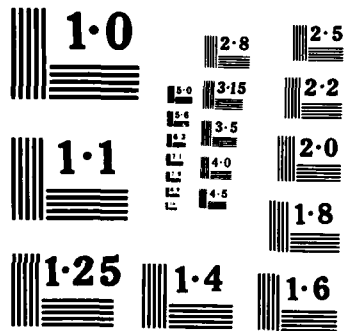
NL



END

FILMED

DTIC



NATIONAL BUREAU OF STANDARDS  
MICROCOPY RESOLUTION TEST CHART

tion is, however, possible if the magnetic line current is discretised into small magnetic dipoles located on  $c$ , as shown in Fig. 2B. This is particularly appropriate to arrays

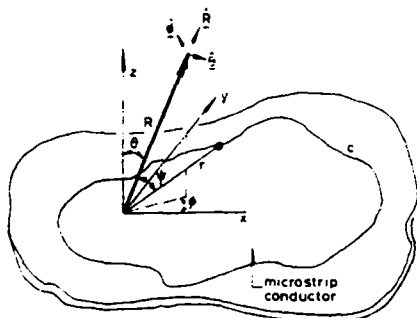


Fig. 2A Co-ordinate system for radiation calculation

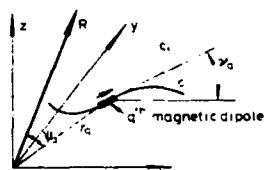


Fig. 2B Parameters specifying  $q$ th magnetic dipole  
 $c_t$  is a tangent to the contour  $c$

formed from sharp bends, such as the rampart line, where radiation is predominantly localised to the bends. The integral in eqn. 2 is thus replaced by a summation over  $Q$  small magnetic dipoles:

$$E_{rad} = jhK \sum_{q=1}^Q M_q e^{jkh r_q \cos \theta_q} \sin(\phi - \gamma_q) \cos \theta \cos(\phi - \gamma_q \phi) \quad (3)$$

where  $\gamma_q$  is the angle between the  $x$ -axis and a tangent  $c_t$  to the contour  $c$  at the  $q$ th dipole (Fig. 2B), and the amplitude and phase of the magnetic dipole strength  $M_q$  at that point is determined by the line voltage and, hence, by the structure used.  $Q$  will, in general, be much larger than  $N$ , the number of periods in the array, as each period will be modelled by several small dipoles. The  $(Q+1)$ th and  $(Q+2)$ th terms may be added to account for transition and termination radiation as described in Section 2.3. Assuming Ludwig's third definition of crosspolarisation [24], suitable for broadside pointing antennas, the required polarisation,  $E_{ref}$ , and the crosspolarisation,  $E_{cross}$ , are, for linear polarisation,

$$E_{ref} = E_{rad} \cos(\phi - \Phi) \sin(\phi - \Phi) \quad (4)$$

$$E_{cross} = E_{rad} \sin(\phi - \Phi) \cos(\phi - \Phi) \quad (5)$$

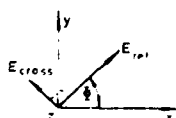


Fig. 2C Definition of linear reference polarisation direction

IEE PROCEEDINGS, Vol. 131, Pt. II, No. 4, AUGUST 1984

where  $\Phi$  is the angle of the reference polarisation vector of the antenna defined for  $\theta = 0$  [24] as shown in Fig. 2C. Although not dealt with explicitly in this paper, the magnitude of the reference and orthogonal hand of circular polarisation may be obtained from eqn. 3. Substitution of eqn. 3 into eqns. 4 and 5 gives, for linear polarisation and  $\theta = \phi = 0$ ,

$$E_{ref} = jhK \sum_{q=1}^Q M_q e^{jkh r_q \cos \theta_q} \sin(\Phi - \gamma_q) \quad (6)$$

$$E_{cross} = jhK \sum_{q=1}^Q M_q e^{jkh r_q \cos \theta_q} \cos(\Phi - \gamma_q) \quad (7)$$

Eqns. 6 and 7 indicate that the maximum reference field is obtained in the broadside direction when  $\Phi$  is given by

$$\Phi = 90 + \gamma_q \quad (8)$$

i.e. when the dipole orientation is orthogonal to the reference polarisation, and in this case  $E_{cross} = 0$ .

The microstrip-line edge voltage  $v$  is determined both by the conductor geometry and the substrate dielectric constant  $\epsilon_r$ . Thus, eqn. 2 includes dependence on both geometrical and material effects. However, assuming constant  $h$  and  $\epsilon_r$  across the array means that the dependence of  $M_q$  on  $r_q$  and  $h$  is similar for all  $q$ ; hence, the ratio of  $E_{cross}$  to  $E_{ref}$  will depend on the array geometry only. This means that specification of the distribution and orientation of  $M_q$  will allow first-order estimates of crosspolarisation to be deduced. Illustrative examples of such distributions are given in the following Section. These are then critically assessed in Section 3.

## 2.2 Illustrative examples of source distributions

On applying the equivalence principle (eqn. 1) to the specific microstrip array types of Fig. 1B the source distributions for the analysis of Section 2.1 can be deduced. In some cases these are calculated explicitly, whilst in others appropriate References are indicated. It is assumed throughout that  $w/\lambda_0 \ll 1$ , where  $w$  is the feed-line width and that no higher-order modes are excited in the feed line at the radiating discontinuities. The thin-feed-line assumption means that the magnetic current at either side of the feed line can be replaced by a single equivalent magnetic current at the line centre localised to regions of curvature in the line. Thus, for types composed of bends in the feed line, the source distribution is confined to the line bends, and for patch arrays no radiation occurs from the straight feed lines. In the latter case, the resonant action of the patch element gives rise to a magnetic current distribution at the patch edge. This assumption results in the source distribution shown in Fig. 3, where the continuous distributions in the serpent line and patch arrays have been discretised so that all types can be analysed by use of eqn. 3. In the serpent line (Fig. 3a) the dipoles are oriented tangentially to the line. For lines with right-angle bends Fig. 3d and 3f the dipoles are oriented at  $45^\circ$  to the input line [6], and where two closely spaced bends occur the resultant of the two dipoles is taken, as in Fig. 3e and the T-junctions of Fig. 3f. Analysis using electric currents [5] leads to results equivalent to magnetic dipoles oriented as in Fig. 3c for the circularly polarised chain antenna, where the presence of the phasing loop shown in Fig. 1Bc accounts for the dipole oriented at  $\gamma = 90^\circ$ . It follows then that, as the triangle line (Fig. 3b) has no such loops, both dipoles are oriented at  $\gamma = 0^\circ$ . In the patch arrays the dipoles are located at the patch edges and appropriately oriented [21].

The polarisation characteristics of these distributions can be obtained from eqn. 3.  $M_q$  is a function of the substrate height, dielectric constant and the line voltage at the  $q$ th dipole. In addition, it is also dependent on the local radius of curvature  $\rho_q$  [23] in the case of Fig. 3a, or the angle subtended at the bend  $\alpha_q$  [5, 6] in the case of Figs. 3b-f, where  $\alpha_q = 90^\circ$  for Figs. 3d, e and f. The line voltage is subject to a progressive reduction down the array due to radiation. This can be approximately deduced by integrating the radiated power in the far field and hence

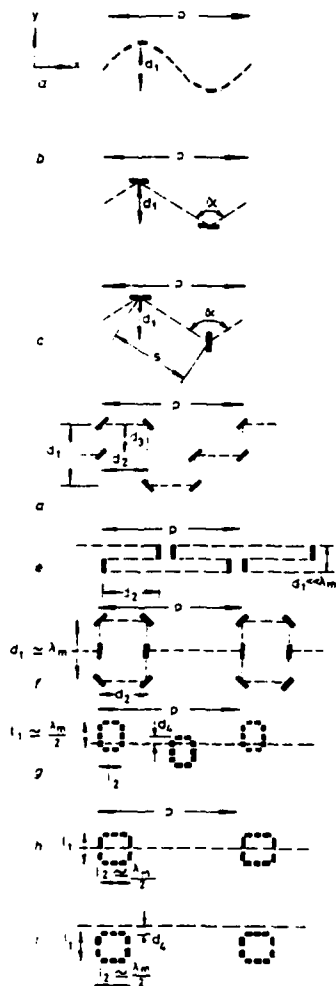


Fig. 3 Magnetic dipole source distributions in microstrip array types of Fig. 1B

— small dipoles  
--- feed lines  
Co-ordinate system shown in Fig. 3a, fundamental mode patch operation assumed  
a Serpentine line  
b Triangle line  
c Circularly polarised chain antenna  
d Rampart line  
e Franklin array  
f Linearly polarised chain antenna  
g Comb-line and overlaid patch array  
h Series-connected patch array  
i Parasitic patch array

obtaining the ratio of the power incident on the  $q$  and  $(q-1)$ th elements, although in the first-order analysis described below this is not done. In the patch arrays the voltage at each dipole is determined by the resonant mode field value at the patch edge.  $r_q$  and  $\psi_q$  of eqn. 3 are determined from Fig. 2A, and the geometrical array parameters given in Figs. 3a-d, and  $\gamma_q$  is given by inspection of Figs. 3a-d.

In Section 8.1 a first-order analysis based on eqn. 3 is done for the sinusoidal serpent line (Fig. 3a). For the circularly polarised chain line (Fig. 3b), expressions for  $E_{rad}$  are derived using an electric current analysis in Reference 5; this allows deduction of  $M_q$ . Removal of the element phasing due to the small loops then allows similar expressions to be derived for the triangle line Fig. 3c.  $M_q$  for use in the arrays of Figs. 3d, e and f is given in Reference 6, and the magnetic current analysis described there may also be used for the arrays of Figs. 3b and c.  $M_q$  may be derived for the patch arrays (Figs. 3g, h and i) and eqn. 3 solved, although  $E_{rad}$  derived using eqn. 2 is given for this case in Reference 25.

In calculating the ratio  $C_p$  of peak cross- to broadside reference polarisation level per period in Table 2, it is necessary to know only the relative magnitude and phases of  $M_q$ , rather than the full functional dependence, in addition to  $\gamma_q$ ,  $r_q$  and  $\psi_q$ . This simplifies the calculation, particularly for the arrays of Figs. 3b, c, e and f. For the other arrays, the analysis given in Section 8.1 and the References quoted above are used.

### 2.3 Radiation from feed transitions and array terminations

Estimations of the radiation loss from microstrip antenna feed transitions shown in Figs. 4a-c have been made pre-

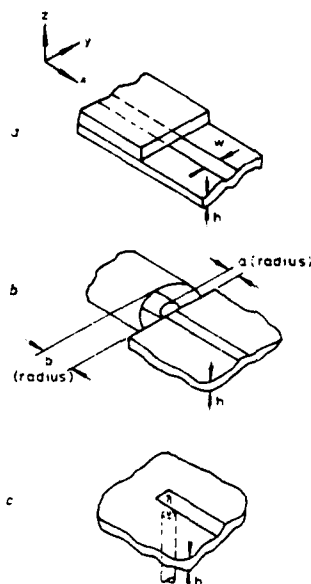


Fig. 4 Microstrip transitions

a Triplate in-line type, showing co-ordinate system common to analysis of all types  
b Coaxial in-line type  
c Coaxial through the substrate type

viously [14], and the results are summarised here to enable the effect on crosspolarisation to be assessed. For the purpose of this study it is convenient to compare the magnitude of the power radiated by the various transitions to that radiated from a microstrip open end.

The magnitude of the radiation from a microstrip to triplate transition (Fig. 4a) compared with a microstrip open circuit placed at the same point is given, at low frequencies, by

$$T = \frac{G_t}{G_o} = \frac{3\epsilon_r^2 Z_0 \sqrt{\epsilon_r}}{90\lambda_0^2} \left( \frac{w_{tr}}{w_{om}} \right)^2 \quad (9)$$

where  $G_t$  and  $G_o$  are the radiation conductances of the transition [14] and open-circuit end [26], respectively; the triplate [27] and microstrip [28] equivalent widths  $w_{tr}$  and  $w_{om}$ , respectively, are given by

$$w_{tr} = \frac{60\pi h}{\sqrt{\epsilon_r} Z_0} \quad (10)$$

and

$$w_{om} = \frac{120\pi h}{\sqrt{\epsilon_r} Z_0} \quad (11)$$

where  $h$  is defined in Fig. 4a,  $\epsilon_r$  is the microstrip and triplate dielectric constant,  $Z_0$  and  $Z_t$  are the microstrip and triplate impedances, respectively, and  $\epsilon_r$  is given by [29]

$$\epsilon_r = \left\{ (\epsilon_r + 1) + (\epsilon_r - 1) \left( 1 + \frac{10h}{w} \right)^{-1.2} \right\} / 2 \quad (12)$$

where  $w$  is defined in Fig. 4a. Eqn. 9 assumes the transition is matched. For  $\epsilon_r = 2.32$ ,  $T = 0.21$ , which means that the triplate to microstrip transition radiates about one-fifth of the power radiated by the line open end. The feed radiation is, of course, a much smaller proportion of the total radiation from a microstrip array containing many open-circuit radiators.

For an in-line coaxial to microstrip matched transition (Fig. 4b) at low frequencies [14]:

$$T = \frac{4(b-a)^2 a^2}{w_{om}^2 h^2} \quad (13)$$

where  $a$  and  $b$  are defined in Fig. 4b and  $w_{om}$  and  $h$  are as above. For a commercially available connector having  $b = 2.07$  mm,  $a = 0.64$  mm and for  $\epsilon_r = 2.32$  and  $h = 0.793$  mm,  $T = 0.29$ . Henderson and James [14] do not give the radiation pattern of these two transitions, but indicate that as they are small radiators they will have low directivity and behave like small dipoles. Since current is being intercepted in the above cases, the dipoles will be predominantly of the magnetic type oriented across the current flow, i.e. with  $\gamma = 90^\circ$  (Fig. 2B) assuming the feed line is in the  $x$  direction (Fig. 4a).

For a 'through the substrate' coaxial to microstrip transition (Fig. 4c) at low frequencies [13]:

$$T = \frac{1 - \frac{\epsilon_r - 1}{2\sqrt{\epsilon_r}} \log \frac{\sqrt{\epsilon_r} + 1}{\sqrt{\epsilon_r} - 1}}{\frac{\epsilon_r - 1}{\epsilon_r} - \frac{(\epsilon_r - 1)^2}{2\epsilon_r \sqrt{\epsilon_r}} \log \frac{\sqrt{\epsilon_r} + 1}{\sqrt{\epsilon_r} - 1}} \quad (14)$$

For  $\epsilon_r = 2.32$ ,  $T = 0.3$ . The radiation pattern is similar to that of a magnetic dipole placed across the strip end with

$\gamma = 90^\circ$ , although the lobes along the ground plane are of unequal size.

The effect of radiation from these transitions can be approximately modelled by including a  $(Q+1)$ th term in eqn. 3 representing a magnetic dipole located at the transition, assumed to be the origin of co-ordinates so that  $r_{Q+1} = 0$  and oriented with  $\gamma_{Q+1} = 90^\circ$ . The relative magnitude of the dipole is specified as

$$M_{Q+1} = Z_0 \sqrt{\frac{2T}{\epsilon_r}} \quad (15)$$

where  $Z_0$  is the free-space impedance. The crosspolarised field due to the transition in the broadside direction is thus given by eqns. 7 and 15:

$$E_{cross} = jhKZ_0 \sqrt{\frac{2T}{\epsilon_r}} \cos(\Phi - 90^\circ) \quad (16)$$

which indicates that  $|E_{cross}|$  will be maximum when  $\Phi = 90^\circ$ .

If the array is terminated in a matched load, to form a travelling-wave antenna, then typically only a few percent of the array input power is dissipated in the load [16]. In this case radiation from the termination can be neglected. However, in the case of resonant arrays, radiation from an open-circuit termination may be significant, in which case it can be modelled by including a  $(Q+2)$ th term in eqn. 3 representing a magnetic dipole across the feed line at the position of the open-circuit termination and thus oriented with  $\gamma = 90^\circ$ . A short-circuit termination will radiate less [13], but is practically more difficult to implement.

## 2.4 Scattering of substrate surface waves

Substrate surface waves will be excited in microstrip at any discontinuity. These waves will be partially reflected and radiated at discontinuities within their paths, such as at the edge of the substrate, and can also provide an additional coupling mechanism between the radiating elements of the array. This unwanted radiation will increase both the reference and crosspolarisation sidelobe levels. The calculation of the total effect of the surface waves in a finite linear array is a formidable task, and here we give only an estimate of the resulting crosspolarisation level based on equations from a previous analysis [15].

The ratio,  $S_L$ , of surface wave generation to radiation from a microstrip open-circuit end can be determined from:

$$S_L = \frac{G_s}{G_o} = \frac{\cos^2(k_{y1}h)\epsilon_r k_{x1}^2}{\cos^2(k_{y1}h)\epsilon_r k_{x2}^2 + k_{x1}^2 h k_{y2}} \quad (17)$$

where  $G_s$  and  $G_o$  are the conductances associated with surface-wave generation and radiation, respectively, and  $k_{y1}$  and  $k_{x2}$  are surface wave propagation coefficients determined from the equations

$$k_{x1}^2 + k_{y2}^2 = k_0^2(\epsilon_r - 1) \quad (18)$$

$$\tan(k_{y1}h) = \epsilon_r k_{y2} k_{x1} \quad (19)$$

When  $h/\lambda_0 \ll 1$ ,  $k_{x1}$  can be more easily found by

$$k_{x1}^2 = (1 - \epsilon_r^2 + \epsilon_r \sqrt{\epsilon_r^2 + 4k_0^2 h^2 (\epsilon_r - 1)}) / 2h^2 \quad (20)$$

which is accurate provided that  $\tan(k_{y1}h) \approx k_{y1}h$ .

$S_L$  is a pessimistic estimate of the crosspolarised radiation and assumes that all contributions from the surface wave are scattered coherently in some direction. This may thus relate to peak crosspolarisation values. An estimate relating to average levels is obtained by assuming that, in general, incoherent scattering of the surface wave takes

place, whilst  $E_{\text{sw}}$ , due to direct radiation adds coherently to give the array power gain  $G$ . The level of crosspolarisation due to surface waves,  $S_L$ , referred to the peak gain is then given by

$$S_L = S_L G \quad (21)$$

$S_L$  and  $S_L$  depend on the substrate type and thickness in addition to antenna gain, and some guidelines for choice of substrate can be determined. Such deductions have been made for microstrip patches [2], and while some are applicable here the array series feeding technique needs to be taken into account. The array is represented by a periodically loaded transmission line (Fig. 5) with conductance  $G_m$  representing radiation from the  $n$ th period

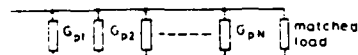


Fig. 5 Periodically loaded transmission line model of array

region and terminated in a matched load as shown or an open or short circuit. The period radiation conductance can be determined from an integration over the far field of the total Poynting vector due to all the small magnetic dipoles in a single period. However, useful first-order information can be extracted by assuming that  $G_p$  is equivalent to the conductance  $G_o$  of an isolated open-circuit end in a line of impedance  $Z_m$ . This case is approximately equivalent to a comb-line array with  $\lambda_m$  stub spacing [9].  $G_o$  is given by [26]:

$$G_o = w_{em}^2 90 \lambda_o^2 \quad \text{for } w_{em} < 0.35 \lambda_o \quad (22)$$

$$= w_{em} 120 \lambda_o - \frac{1}{60 \pi^2} \quad \text{for } 0.35 \lambda_o \leq w_{em} < 2 \lambda_o \quad (23)$$

where  $w_{em}$  is given by eqns. 11 and 12. The ratio  $P_R$  of power radiated per period to the power incident on the period is given by [30]

$$P_R = G_o Z_m \quad (24)$$

where  $Z_m$  is the feed-line impedance. Figs. 6a and b shows  $P_R$  and  $S_L$  against  $h/\lambda_o$  and  $\epsilon_r$ , respectively, where  $P_R$  is given by eqn. 24 with eqns. 22 or 23 and  $S_L$  by eqn. 17 with eqns. 18 and 19. It can be seen from Fig. 6a that the use of a thin substrate results in both low crosspolarisation due to surface wave generation and low radiation, whereas Fig. 6b indicates that both low crosspolarisation and high radiation are obtained when  $\epsilon_r < 2$ .  $\epsilon_r > 2$  results in both low crosspolarisation and low radiation. Thus, use of very low  $\epsilon_r$  is suggested, whilst choice of  $h$  alone results in a compromise between surface wave excitation and efficiency.

The amount of power lost in a matched load termination is determined by  $P_R$ . For a given aperture distribution on the array, the ratio,  $P_L$ , of power lost in the load to array input power is related to the power radiated by the period at the peak of the distribution  $P_{R \text{ peak}}$  and the number of radiating periods in the array  $N$  as shown in Fig. 7, where  $NP_{R \text{ peak}}$  is shown for Taylor distributions [16] for -25 and -35 dB sidelobe levels. It can be seen that for given  $N$  it is necessary to maximise  $P_{R \text{ peak}}$  to minimise  $P_L$ , and unless  $\epsilon_r < 2$  this will result in increased crosspolarisation due to surface wave generation. For a given  $P_L$ , an array of more elements will require lower  $P_{R \text{ peak}}$  and hence incur less crosspolarisation. In addition, the array gain  $G$  will also be larger, until line losses dominate, and this will further suppress  $S_L$  as indicated in eqn. 21.

In a resonant array terminated in an open circuit, most of the power incident on the termination is reflected back

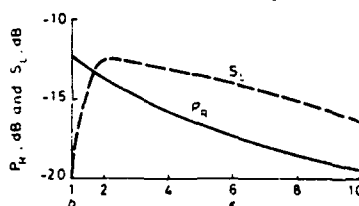
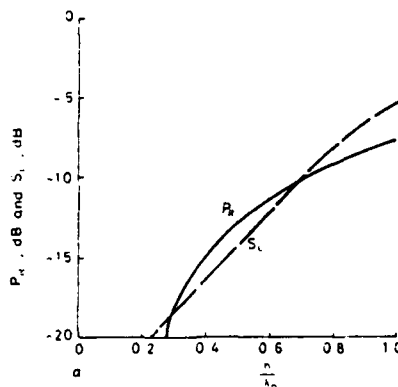


Fig. 6  $P_R$  and  $S_L$  for various substrate parameters for array of Fig. 5 with open-circuit microstrip lines as radiating elements

$N = 30$   
 $a/\lambda_o = 2.32$   
 $h/\lambda_o = 0.04$

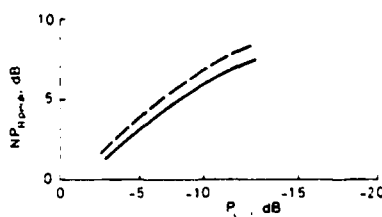


Fig. 7 Element radiation at the peak of the aperture distribution,  $P_{R \text{ peak}}$  against ratio  $P_L$  of power lost in load to input power for array of  $N$  elements

— -25 dB sidelobe level  
--- -35 dB sidelobe level

into the array and subsequently radiated while a small amount will be directly radiated at the termination, as described in Section 2.3. Due to the increased signal path length this resonant action has been found to significantly increase the line losses in short arrays [9], where substantial power is incident on the termination. In long arrays where little power is incident, the increase is found to be small [10]. It has been shown in Fig. 7 that the power incident on the termination is related to  $P_{R \text{ peak}}$  for an array with a matched load termination. The above results suggest that similar relationships between array line losses and crosspolarisation due to surface wave generation may be derived for resonant arrays.



Series-fed microstrip arrays							
Radiating element	Array type	$\Phi$ , degrees	Design degrees of freedom			$C_u$	
			Control of period length $p$	Control of $P_u$	Others (reported)	$\phi = 0$	$\phi = 45$
Bends	Serpent line	90	yes	yes <sup>++</sup>	none	3.83 (for $d, p = 1$ )	
	Triangle line	90	yes	yes <sup>++</sup>	none	0.0	0.5 (for $\sigma = 90$ )
	Rampart line	$0 < \Phi < 180$ (and circ. pol.)	yes	yes <sup>++</sup>	control of $\Phi$ and $E_{cross}$	$> 5.0$	
	Chain antenna linearly polarised	0	yes	yes <sup>+</sup>	none	0.0 (for $d, \sigma = 0.5\lambda_m$ )	0.32
	circularly polarised		yes	yes <sup>++</sup>	none	0.91 (for $\sigma = 120$ )	
	Franklin line	0	yes	yes <sup>+</sup>	none	0.0	0.43
Straps and open circuits	Comb line	90	yes	yes <sup>*</sup>	none	0.0	0.04
	Series connected patch array	0	yes	yes <sup>*</sup>	none	0.0	0.04
	Overlaid patch array	90	yes	yes <sup>*</sup>	none	0.0	0.04
	Parasitic patch array	0	yes	yes <sup>*</sup>	none	0.0	0.04

+  $P_z$  controlled by line width

### 3.1 Design degrees of freedom

### 3.2 Assessment of crosspolarisation

$E_{xx}(\theta=0)$  and  $E_{cross}^{peak}$  are given by eqns. 4 and 5, respectively, for linear polarisation. For circular polarisation they refer to broadside reference hand and peak orthogonal hand, respectively, and in this case are derived from eqn. 3.  $C_p$  will be suppressed to a large extent within the array by the array factor  $F(\theta, \phi)$  so that the array crosspolarisation  $C_A$  is given by

$$C_A = C_p F(\theta, \phi) \quad (26)$$

Estimates of  $C_F$  in the  $\phi = 0^\circ$  plane are shown in Table 2 for the magnetic dipole configurations of Fig. 3. Where zero levels occur, results in the  $\phi = 45^\circ$  plane are given. For the sinusoidal serpent line the analysis of Section 8.1 indicates that  $E_{\text{cross}}^{\text{rank}}$  occurs at  $\theta = -90^\circ$ , and in this case eqn. 46 reduces to

$$C_p \approx \frac{3.83d_i}{n} \quad (27)$$

For  $d_1, p = 1.0$ , for example,  $C_p = 3.83$  ( $= 11.7$  dB). For  $F(\theta, p) = -30$  dB eqn. 26 gives  $C_1 = -18.3$  dB for this case. Measured results [3] show that  $C_1 = -14$  dB for an array designed for  $-30$  dB sidelobe levels. High measured crosspolarisation in the  $\theta = 0^\circ$  plane also occurs in the rampart line for most  $\Phi$  for linear polarisation and also for circular polarisation [6]. The cross polarisation behaviour of the serpent and rampart line is analogous to waveguide slot arrays due to similarities in the magnetic dipole configurations. In particular, high  $C_p$  is noted in the waveguide I-slot [31] and the narrow-wall inclined slot [32] where  $C_1 = -20$  dB has been measured.

For the triangle line, linearly polarised chain antenna with  $d_1 = 0.5\lambda_m$ , where  $\lambda_m$  is the microstrip wavelength, and the Franklin antenna with  $d_1 \ll \lambda_m$ ,  $C_F = 0$  in the

$\phi = 0^\circ$  plane.  $C_p$  is significant for all these types in the  $\phi = 45^\circ$  plane.

The radiated field of the circularly polarised chain antenna in the  $\phi = 0^\circ$  plane is given by [5]

$$E_{rad} = j \sin \frac{\alpha}{2} \cos \left\{ k_0 s \left( 1 - \sin \frac{\alpha}{2} \sin \theta \right) \right\} \hat{\theta} - \cos \frac{\alpha}{2} \sin \left\{ k_0 s \left( 1 - \sin \frac{\alpha}{2} \sin \theta \right) \right\} \hat{\phi} \quad (28)$$

where  $s$  and  $\alpha$  are defined in Fig. 3c. For circular polarisation in the broadside direction,  $\alpha = k_0 s$ ; hence,  $|E_{rad}|_{\theta=0} = \sin \frac{\alpha}{2} \cos \frac{\alpha}{2}$ . The maximum orthogonal hand of polarisation occurs in the  $\theta = 90^\circ$  direction; hence

$$C_p = \cos \left\{ \frac{\alpha}{2} \left( 1 - \sin \frac{\alpha}{2} \right) \right\} - \cot \frac{\alpha}{2} \sin \left\{ \frac{\alpha}{2} \left( 1 - \sin \frac{\alpha}{2} \right) \right\} \cdot 2 \cos \frac{\alpha}{2} \quad (29)$$

For  $\alpha = 120^\circ$ ,  $C_p \approx 0.91$ . Arrays formed from patch elements have  $C_p = 0$  in the  $\phi = 0^\circ$  plane and low  $C_p$  in the  $\phi = 45^\circ$  plane [2].

It should be noted that these results have been obtained assuming that there is no higher-order mode generation either in the feed line at bends or at steps. Second-order crosspolarisation effects in both the rampart line [6] and in the comb-line array as described in the following Section have been shown to be due to these sources. Thus, although such first-order analysis allows a qualitative first estimate, each type requires a detailed examination to establish its ultimate performance.

#### 4 Application to comb-line arrays

##### 4.1 Analysis of comb structure

The comb-line array [9] configured for  $\lambda_m$ ,  $\lambda_m/2$  and  $\lambda_m/4$  spacing, where  $\lambda_m$  is the microstrip wavelength, is shown in Fig. 8. A complete analysis of such structures would require inclusion of radiation from the whole comb structure including the input connector and also scattering from the substrate surface wave. Such an approach is possible [33], but the computational difficulties are severe. A simplified approach is used here, based on the analysis of Section 2.1, in which radiation from a single stub and associated feed line is estimated using the magnetic current method. Overall array action is obtained by the application of appropriate array factors. Radiation from the input

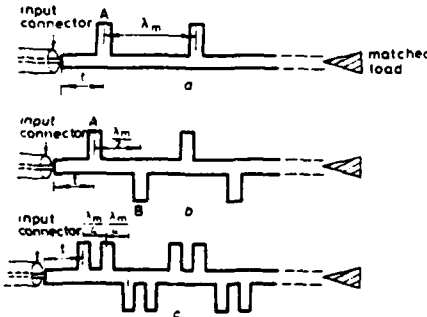


Fig. 8 Microstrip comb-line arrays

a Wavelength spacing  
b Half-wavelength spacing  
c Quarter-wavelength spacing

254

connector is subsequently added and substrate surface wave effects are estimated. Mutual coupling within the structure is not accounted for.

$E_{rad}$  is calculated from eqns. 1 and 2, where the integration contour, indicated by the broken line in Fig. 9, is

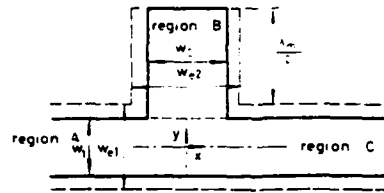


Fig. 9 Geometry of single stub of comb-line array

located at the equivalent widths,  $w_{e1}$  and  $w_{e2}$ , of the line sections. The feed lines are assumed to stretch to infinity. The voltage at the conductor edge,  $v$ , is approximated by

$$v = E_z h \quad (30)$$

where  $E_z$  is the  $z$  directed field at the edge of an equivalent closed waveguide model of the structure [34]. Analysis of the waveguide model is described in Section 8.2. The reference polarisation direction is  $\Phi = 90^\circ$ , so that eqns. 4 and 5 give

$$E_{ref} = E_{rad} \{ \sin \phi \cdot \hat{\theta} + \cos \phi \cdot \hat{\phi} \} \quad (31)$$

$$E_{cross} = E_{rad} \{ -\cos \phi \cdot \hat{\theta} + \sin \phi \cdot \hat{\phi} \} \quad (32)$$

The radiated fields in the  $\phi = 0^\circ$  plane are then given by

$$E_{ref} = -8jk\tau_{20}h \sin \left\{ \frac{k_0 w_{e2}}{2} \sin \theta \right\} k_0 \tan \theta \quad (33)$$

$$E_{cross} = - \sum_{s \text{ odd}} 4k\tau_{2s}h \cos \left\{ \frac{k_0 w_{e2}}{2} \sin \theta \right\} \times \{ 1 - e^{-\mu_{2s}(\lambda_m/2)} \} / k_{2s} - \sum_{s \text{ even}} 4jk\tau_{2s}h \sin \left\{ \frac{k_0 w_{e2}}{2} \sin \theta \right\} \times \{ 1 - e^{-\mu_{2s}(\lambda_m/2)} \} / k_{2s} \quad (34)$$

where  $w_{e2}$  is defined in Fig. 9 and  $\tau_{2s}$  and  $k_{2s}$  are the amplitude and wave number, respectively, of the higher-order modes excited by the T-junction in the stub. When  $\tau_{2s} = 0$  for  $s > 0$ ,  $E_{cross} = 0$ , confirming the result given in Table 2. For the comb-line array specified in Fig. 10a, for which  $|\tau_{20}| = 0.67$  and  $|\tau_{21}| = 0.57$ ,  $C_p = 0.50$  for  $\theta = 90^\circ$  and  $\phi = 0^\circ$  assuming that only the fundamental and first higher-order modes are present in the stub. This value is comparable to those found for arrays formed from bends as shown in Table 2.

The radiated field in the  $\phi = 0^\circ$  plane  $E_{rad}^T$  due to an array of  $N$  periods is given by

$$E_{rad}^T = (E_{ref} + E_{ref}^* e^{j\epsilon}) \{ 1 + \delta e^{j\epsilon/2} \} \frac{\sin N\epsilon/2}{\sin \epsilon/2} \quad (35)$$

where

$$E_{rad} = E_{ref} \hat{\phi} + E_{cross} \hat{\theta} \quad (36)$$

In eqn. 35  $*$  denotes complex conjugate, and

$$\epsilon = \frac{k_0 \lambda_m}{2} \{ \sin \theta - \sqrt{\epsilon_{eff}} \} \quad (37)$$

where  $\epsilon_{eff}$  is the effective dielectric constant in the feed line and

$$\delta = 1 \text{ for } \frac{\lambda_m}{4} \text{ spacing} \\ = 0 \text{ for } \frac{\lambda_m}{2} \text{ spacing} \quad (38)$$

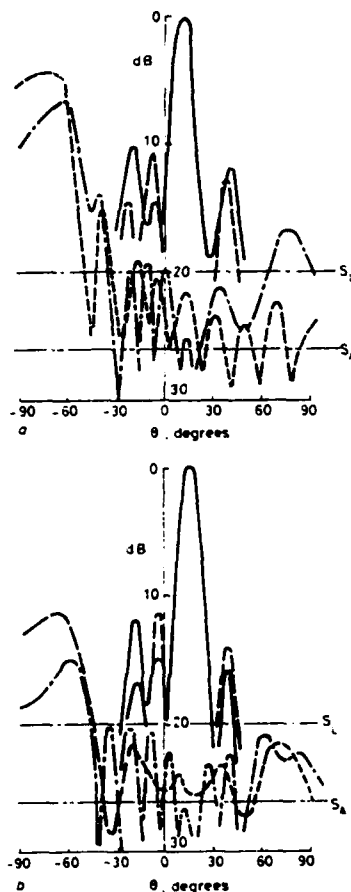


Fig. 10 Radiation patterns in  $\phi = 0^\circ$  plane of comb-line array with ten stubs having  $\approx \lambda_m/2$  spacing  
Frequency = 4.3 GHz,  $\epsilon_r = 2.52$ ,  $h = 1.59$  mm,  $a_1 = 5$  mm  
Input connector coaxial in-line type (Fig. 4b)  
 $a_2 = 16$  mm  
 $b = 8$  mm  
 $E_{\theta}$  ——— measured ——— theory  
 $E_{\phi}$  ——— measured ——— theory

#### 4.2 Feed and surface wave effects

For an assumed unity field amplitude in the feed line, the magnitude of the  $(Q + 1)$ th magnitude dipole representing the feed radiation is obtained from eqn. 15. As  $\phi_{Q+1} = 90^\circ$  and  $\phi = 90^\circ$ , the field due to this source will be cross-polarised in the  $\phi = 0^\circ$  plane. This term is added directly to eqn. 35.

No directional information is obtained from the analysis of the surface wave scattering, and it cannot be added into eqn. 35.  $S_A$  and  $S_L$  are thus simply superimposed on the presented results.

#### 4.3 Experimental and theoretical results

Figs. 10a and b show results for a ten-stub array with  $\approx \lambda_m/2$  spacing; it can be seen that the measured cross-polarisation level lies between  $-6$  dB and  $-15$  dB. Good agreement between the theoretical and measured [35] results, particularly in the high crosspolarised lobe at  $\theta = -70^\circ$ , is noted. Putting  $\tau_{21} = 0$  in eqn. 34 of the analysis of the array of Fig. 10a resulted in a reduction of the cross-polarisation to  $-28$  dB, indicating that this high lobe is due almost entirely to the first higher-order mode in the stub. Comparison of Fig. 10a and b show that reducing  $w_2$  results, particularly in the high crosspolarised lobe at  $\theta = -70^\circ$ , indicate that this will be accompanied by a reduction in  $P_R$  and, hence, reduced efficiency, and this is confirmed by measurements [35]. Transition radiation is included in the analysis and the effect of removing it in Fig. 10a is to reduce the crosspolarisation outside the high lobe, which remains unchanged, by about 2 dB. This can be implemented in practice by covering the transition with radar-absorbent material. Figs. 10a and b also show that both  $S_A$  and  $S_L$  are, in this case, small in comparison to the measured crosspolarisation.

Figs. 11a and b show results for 38-stub arrays with  $\approx \lambda_m/4$  spacing and screened transitions. The array main beam is now scanned to a backfire direction with  $\theta = -10^\circ$  and narrow stubs are used. In Fig. 11a the maximum crosspolarisation level is  $-16$  dB at  $\theta = 80^\circ$  which is not well predicted theoretically. However, it can be seen that the peak crosspolarisation is within 3 dB of  $S_L$  and the average value is around  $S_A$ . In Fig. 11b the substrate height has been halved, resulting in a reduction in  $S_L$  and  $S_A$  of approximately 6 dB. The crosspolarisation is reduced by a similar amount, indicating that in these arrays it is primarily determined by the surface-wave scattering. The reduction in substrate height also gives rise to a 1.5 dB increase in power lost in the load.

#### 5 Conclusions

Crosspolarisation in linear series-fed microstrip arrays has been shown to be largely dependent on their configuration. Using a simplified magnetic current analysis, useful first-order information has been extracted from geometrical considerations. Whilst not completely quantifying the crosspolarisation behaviour, such an approach, coupled with existing analytical results for transition and surface wave effects, can be used as a guiding tool in the initial design stage. From this some important initial conclusions can be drawn concerning the relationships between the various sources of crosspolarisation and the antenna configuration:

(a) Examination of the conductor geometry suggests that, in general, increased radiation per period in the reference polarisation is accompanied by increased crosspolarisation. In longer arrays the radiation per period is proportionally less and the crosspolarisation is likely to be reduced with respect to the desired reference polarisation.

(b) Little control of radiation from the feed transition is possible apart from screening with absorbent material. Integration of the microwave circuitry with the antenna will remove the need for a transition, although it is not clear whether the radiation from the circuitry will be less than from the transition. Thus, if crosspolarisation from

the other sources is reduced to a small level, this may become a limiting factor.

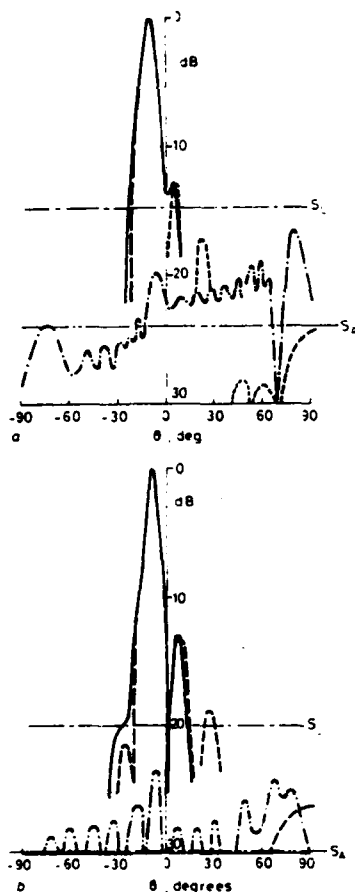


Fig. 11 Radiation patterns in  $\phi = 0^\circ$  plane of comb-line array with 38 stubs having  $\lambda/4$  spacing

Frequency = 17 GHz,  $\epsilon_r = 2.32$ ,  $\epsilon_1 = 1.0$  mm,  $\epsilon_2 = 1.5$  mm  
Input connector coaxial in-line type (Fig. 4b)

$a = 0.793$  mm  
 $b = 0.397$  mm  
 $E_{\theta}$  ——— measured ——— theory  
 $E_{\phi}$  ——— measured ——— theory

(c) The effect of surface wave scattering is reduced for  $\epsilon_r < 2$  or by the use of thin substrates. The latter incurs reduced efficiency, although this will be less significant in longer arrays.

A detailed case has been studied to illustrate the considerations and depth required to bring second-order effects into account. The results for the comb-line array support many of the above generalised conclusions. A lowest level of crosspolarisation of  $-25$  dB has been achieved to date, although reductions may be possible with thinner substrates and longer arrays.

Faced with the numerous types of series-fed printed

arrays that are now known, a designer will find the first-order generalised data presented here a useful starting point and helpful in narrowing down the choice of structure to suit a particular system requirement.

## 6 Acknowledgments

This work was partly supported by the Procurement Executive MOD. Thanks are also due to Dr. W. Menzel for the use of his computer program for modal analysis of the microstrip T-junction.

## 7 References

1. RUDGE, A.W., MILNE, K., OLVER, A.D. and KNIGHT, P.: 'Handbook of antenna design: Vol. 2' (Peter Peregrinus, London, 1983), pp. 79-96.
2. JAMES, J.R., HENDERSON, A. and HALL, P.S.: 'Microwave antenna performance is determined by substrate constraints', *Microwave Syst. News*, 1982, 12, (8), pp. 73-84.
3. SKIDMORE, D.J. and MORRIS, G.: 'Design and performance of covered microstrip serpent antennas', *IEE 3rd International Conference on Antennas and propagation*, Norwich, Apr. 1983, pp. 295-299.
4. TRENTINI, V.G.: 'Flachantenne mit Periodisch Gebogenem Leiter', *Frequenz*, 1960, 14, pp. 230-243.
5. HENRIKSSON, J., MARKUS, K. and TIURI, M.: 'Circularly polarised travelling wave chain antenna', *Proc. 9th European Microwave Conference*, Sept. 1979, pp. 174-178.
6. HALL, P.S.: 'Microstrip linear array with polarisation control', *IEE Proc. H, Microwaves, Opt. & Antennas*, 1983, 130, (3), pp. 215-224.
7. NISHIMURA, S., NAKANO, K. and MAKIMOTO, T.: 'Franklin-type microstrip line antenna', *International Symposium Dig. on Antennas and propagation*, Seattle, 1979, Vol. 1, pp. 134-137.
8. TIURI, M., HENRIKSSON, J. and TALLQVIST, S.: 'Printed circuit radio link antenna', *Proc. 9th European Microwave Conference*, Sept. 1979, pp. 280-282.
9. JAMES, J.R. and HALL, P.S.: 'Microstrip antennas and arrays: Pt. 2—New array-design technique', *IEE J. Microwaves, Opt. & Acoust.*, 1977, 1, pp. 175-181.
10. METZLER, T.: 'Microstrip series array', *IEEE Trans.*, 1981, AP-29, pp. 174-175.
11. HALL, P.S.: 'New wideband microstrip antenna using log-periodic technique', *Electron. Lett.*, 1980, 16, pp. 127-128.
12. OWENS, R.P.: 'Design and manufacture of serpent arrays and parasitic patch arrays', *IEE Colloq. Dig.*, 1982, 19, 'Advances in printed antenna design and manufacture', Feb. 1982, pp. 4-1-4-3.
13. LEWIN, L.: 'Radiation from discontinuities in strip-line', *Proc. IEE*, 1960, 107C, pp. 163-170.
14. HENDERSON, A. and JAMES, J.R.: 'Design of microstrip antenna feeds. Part 1: Estimation of radiation loss and design implications', *IEE Proc. H, Microwaves, Opt. & Antennas*, 1981, 128, (1), pp. 19-25.
15. JAMES, J.R. and HENDERSON, A.: 'High-frequency behaviour of microstrip open-circuit terminations', *IEE J. Microwaves, Opt. & Acoust.*, 1979, 3, pp. 205-218.
16. TAYLOR, T.T.: 'Design of line-source antennas for narrow beamwidth and low sidelobes', *IRE Trans.*, 1955, AP-3, pp. 16-25.
17. JAMES, J.R., HALL, P.S. and WOOD, C.: 'Microstrip antenna theory and design' (Peter Peregrinus, London, 1981), pp. 112-130.
18. HALL, P.S., GARRETT, C. and JAMES, J.R.: 'Feasibility of designing millimetre wave microstrip planar arrays', *AGARD Conference on Millimetre and submillimetre wave propagation and circuits*, Conf. Proc. 245, Munich, Sept. 1978, pp. 31-1-31-9.
19. HARRINGTON, R.F.: 'Time harmonic electromagnetic fields' (McGraw-Hill, New York, 1961), p. 108.
20. JAMES, J.R., HALL, P.S. and WOOD, C.: 'Microstrip antenna theory and design' (Peter Peregrinus, London, 1981), pp. 44, 74.
21. RICHARDS, W.F., LO, Y.T. and HARRISON, D.D.: 'An improved theory for microstrip antennas and applications', *IEEE Trans.*, 1981, AP-29, pp. 38-46.
22. HAMMER, P., VAN BOUCHAUTE, D., VERSCHRAEVEN, D. and VAN CAPELLE, A.: 'A model for calculating the radiation field of microstrip antennas', *ibid.*, 1979, AP-27, pp. 267-270.
23. WOOD, C.: 'Curved microstrip lines as compact wideband circularly polarised antennas', *IEE J. Microwaves, Opt. & Acoust.*, 1979, 3, (1), pp. 5-13.
24. LUDWIG, A.C.: 'The definition of cross polarisation', *IEEE Trans.*, 1973, AP-21, pp. 116-119.
25. JAMES, J.R., HALL, P.S. and WOOD, C.: 'Microstrip antenna theory and design' (Peter Peregrinus, London, 1981), pp. 78-79.

IEE PROCEEDINGS, Vol. 131, Pt. H, No. 4, AUGUST 1984

- 26 JAMES, J.R., HALL, P.S. and WOOD, C.: 'Microstrip antenna theory and design' (Peter Peregrinus, London, 1981), p. 38
- 27 ALTSCHULER, H.M. and OLIVER, A.A.: 'Discontinuities in the centre conductor of symmetrical strip transmission line', *IRE Trans.*, 1960, MTT-7, pp. 328-338
- 28 WHEELER, H.A.: 'Transmission line properties of parallel wide strips separated by a dielectric sheet', *IEEE Trans.*, 1965, MTT-13, pp. 172-185
- 29 SCHNEIDER, M.V.: 'Microstrip lines for microwave integrated circuits', *Bell Syst. Tech. J.*, 1969, 48, pp. 1421-1444
- 30 STARR, A.T.: 'Radio and radar technique' (Pitman, London, 1953), pp. 266-267
- 31 CHIGNELL, R.J. and ROBERTS, J.: 'Compact resonant slot for waveguide arrays', *Proc. IEE*, 1978, 125, (11), pp. 1213-1216
- 32 SILVER, S.: 'Microwave antenna theory and design' (Dover, New York, 1965), p. 299
- 33 BROWN, A.K.: 'The analysis of microstrip travelling wave arrays by use of the moment method', 3rd IEE International Conference on Antennas and Propagation, Norwich, 1983, pp. 32-34
- 34 WOLFF, I., KOMPA, G. and MEHRAN, R.: 'Calculation method for microstrip discontinuities and T-junctions', *Electron. Lett.*, 8, 1972, pp. 177-179
- 35 BROWN, A.K.: 'Crosspolarisation characteristics of linear comb-line microstrip antennas', *ibid.*, 1980, 16, pp. 743-744
- 36 KORN, G.A. and KORN, T.M.: 'Mathematical handbook for scientists and engineers' (McGraw-Hill, New York, 1961), p. 500
- 37 MEHRAN, R.: 'Frequency dependent scattering matrix of microstrip right-angle bends, T-junctions and crossings', *Arch. Elektron. & Übertragungstech.*, 1975, 29, pp. 454-460

## 8 Appendix

### 8.1 First-order analysis of the serpent-line array

For a curved microstrip line [23] the equivalent magnetic current at the line centre is given by

$$M = v w_m \left\{ \frac{1}{\rho} + \frac{2\pi}{\lambda_0} j \sin \phi \sin \theta \right\} \quad (39)$$

where  $\rho$  is the radius of curvature,  $v$  is the line voltage and the line is oriented in the  $x$  direction. For the sinusoidal serpent line, Fig. 12, assuming that  $d_1$  is small, eqn. 39

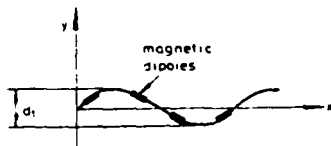


Fig. 12 Magnetic dipole positions for sinusoidal serpent line with  $Q = 4$  in eqn. 3

reduces, in the  $\phi = 0$  plane, to:

$$M = \frac{v w_m}{\rho} \quad (40)$$

The radius of curvature is given by [36]

$$\begin{aligned} \frac{1}{\rho} &= \frac{d^2 y}{dx^2} \sqrt{1 + \left(\frac{dy}{dx}\right)^2} \\ &= -\frac{2\pi^2 d_1}{p^2} \sin\left(\frac{2\pi x}{p}\right) \sqrt{1 + \left(\frac{\pi d_1}{p}\right)^2 \cos^2\left(\frac{2\pi x}{p}\right)} \end{aligned} \quad (41)$$

Assuming that little attenuation of the travelling wave takes place over one period of the array and the wave has unity electric field magnitude, then

$$E = h e^{-j(2\pi x/p)} \quad (42)$$

Substituting eqns. 41 and 42 into 40, and splitting the line into  $Q$  equal length sections with a small magnetic dipole placed at its centre, gives

$$\begin{aligned} M_q &= -\frac{2\pi^2 d_1 h w}{p^2} \sin\left\{\frac{2\pi}{Q}(q - \frac{1}{2})\right\} \\ &\times \exp\left\{-j\frac{2\pi}{Q}(q - \frac{1}{2})\right\} \sqrt{1 + \left(\frac{\pi d_1}{p}\right)^2 \cos^2\left\{\frac{2\pi}{Q}(q - \frac{1}{2})\right\}} \end{aligned} \quad (43)$$

The dipole orientation  $\gamma_q$  is given by

$$\gamma_q = \tan^{-1} \frac{dy}{dx} \bigg|_{q \text{th dipole}} = \tan^{-1} \left[ \frac{\pi d_1}{p} \cos\left\{\frac{2\pi}{Q}(q - \frac{1}{2})\right\} \right] \quad (44)$$

Eqn. 3 with eqns. 4 and 5 for  $\Phi = 90^\circ$  and  $\phi = 0^\circ$  give

$$\frac{E_{\text{refl}}}{E_{\text{ref}}} = \frac{|\sum_{q=1}^Q M_q e^{j(2\pi x/Q) \sin \theta + j(2\pi q/Q) \sin \theta}|}{|\sum_{q=1}^Q M_q \cos \gamma_q|} \quad (45)$$

For  $Q = 4$ , the configuration of dipoles indicated in Fig. 12 results, and eqns. 45 and 25 give

$$\begin{aligned} C_F &= \frac{\pi d_1}{0.7p} \sin\left\{\frac{\pi}{4}\left(1 - \frac{\lambda_m}{\lambda_0} \sin \theta\right)\right\} \\ &\times \cos\left\{\frac{\pi}{2}\left(1 - \frac{\lambda_m}{\lambda_0} \sin \theta\right)\right\} \cos \theta \end{aligned} \quad (46)$$

### 8.2 Analysis of waveguide model of comb array

The waveguide model of the comb array is shown in Fig. 9. Mode matching is performed at the T-junction [37] assuming infinite length feed lines and a fundamental TEM-mode incident from region A. Thus the fundamental mode reflected from the stub end and incident on the junction from region B is ignored in this part of the calculation. Using physical reasoning based on experience with a transmission line model of the array [9], the reflected wave is subsequently included by superimposing a sinusoidal distribution on the fundamental mode in the stub. In addition, as the stub radiates only a small fraction of the power in the feed line, a fundamental mode of unity amplitude is assumed in region C. Thus, for an assumed unity field incident wave, the electric field  $E_z$  in the various regions are:

$$E_{1z} = E_{3z} = e^{-jk_{10}x} \quad (47)$$

$$\begin{aligned} E_{2z} &= \tau_{20} \cos\left\{\frac{2\pi}{\lambda_m}\left(x - \frac{w_{c1}}{2}\right)\right\} \\ &+ \sum_{s=1}^{\infty} \tau_{2s} e^{-k_{2s}x} \cos\left\{\frac{s\pi}{w_{s2}}\left(x - \frac{w_{s2}}{2}\right)\right\} \end{aligned} \quad (48)$$

where  $\tau_{2s}$  and  $k_{2s}$  are the modal transmission and propagation coefficient, respectively. The edge fields required for eqn. 30 are obtained by putting  $x = \pm w_{s2}/2$  into eqn. 48. Typically, the series is truncated after  $s = 8$  to ensure accuracies of the order of a few percent.

Appendix 8.6

Microstrip Patch Arrays with Spherical  
Dielectric Overlays <sup>9</sup>.

Microstrip Planar Arrays with Dielectric  
Sphere Overlays <sup>18</sup>,

and

Dielectric Reflector Feed with Microstrip  
Excitation <sup>19</sup>.

## MICROSTRIP PATCH ARRAYS WITH SPHERICAL DIELECTRIC OVERLAYS

Chris. M. Hall, J.R. James and G. Andrasic.

Royal Military College of Science, Shrivenham, UK.

### INTRODUCTION

Recently, ways of incorporating dielectric feeders into microstrip arrays, to reduce losses at millimetre wavelengths, have been studied (1,2,3) but difficulties are then encountered concerning the connection of such feeders to conventional metal waveguide which is commonly in use. In this present investigation we consider alternative ways of utilising dielectric material to enhance the performance of microstrip arrays whereby dielectric spheres are overlaid on top of a patch array. Clearly the new structure, like the sandwiched substrate technique, is constructionally more complicated but it will be seen to offer enhancement at the expense of some increased depth and loss. The use of dielectric spheres in conjunction with waveguide apertures at microwaves has previously been studied but the incorporation of microstrip patches is novel, particularly as the sphere is exposed to the patch nearfields. Furthermore a selection of dielectric spheres can be readily purchased offering many new possibilities for constructing low-cost light weight arrays at millimetres. In this paper we describe initial results, mainly from experiments, to establish this novel technique and useful recommendations are given.

### THEORY

Previous modal analyses of dielectric spheres, used as antennas, have been mainly concerned with waveguide apertures (4-6) where the excitation field extends over a large region. In the present case the patch fields are concentrated at the microstrip edges, introducing near field effects. As such, the modal technique, based upon spherical wave functions, is likely to require accurate representations of the local patch fields.

In our analysis the microstrip resonant patch is modelled as two magnetic Hertzian dipoles, at opposite ends of the resonator (7). The fields on the surface of the sphere are calculated and are converted to fictitious sources from which the far-field radiation pattern is obtained by the Equivalence Principle. Allowance is made for attenuation in the ray paths due to dielectric losses and hence the gain of the sphere/patch combination can be estimated. The performance of an array of such elements is obtained by invoking the array factor.

### ANTENNAS CONSTRUCTED AND MEASURED

The basic structure considered was that of a PTFE sphere ( $\epsilon_r = 2.2$ ,  $\tan \delta = 0.001$ ) placed over and in contact with a small radiating aperture such as a microstrip patch: Fig 1. Measurements at microwaves and at millimetres using complete and truncated spheres led to the establishment of gain limitations and to estimates of the optimum size of sphere for best gain enhancement and pattern quality.

Comparisons were made between the basic parallel-fed microstrip patch array, Fig 2a, and the same structure loaded with dielectric spheres, Fig 2b, based upon pattern quality and gain. The efficiency of these antennas was calculated from the measured gain and beamwidth, from which effective aperture size was estimated and hence the gain in the absence of dielectric loss. These initial results led to the design of a large array operating at 90 GHz which used an overlay of dielectric spheres to yield improved gain and pattern quality.

### EXPERIMENTAL AND THEORETICAL RESULTS

The basic action of an overlaid sphere upon a patch was demonstrated using a 50 mm diameter sphere of low loss dielectric material (Eccostock HT0003),  $\epsilon_r = 2.2$ , placed upon a square microstrip patch on a substrate  $\epsilon_r = 2.3$  and height  $h = 0.789$  mm. On placing the sphere upon the patch a lowering of the resonant frequency by 1.7% from 15.64 GHz to 15.37 GHz was noticed. At this frequency the sphere was 2.56 free space wavelengths in diameter. Measured and computed radiation patterns were found to be in good agreement in the H-plane and illustrated the good beam shape and sidelobe levels that are achieved with an overlaid sphere, Fig 3. The cross-polarisation level was less than -20 dB. Feed radiation was evident in the E-plane co-polar pattern but resulted in a spurious radiation level of less than -15 dB. This in itself is an improvement over the conventional microstrip patch configuration. The gain of the above example was 15.2 dBi.

This and other examples are plotted in Fig 4 showing the correspondence between measured gain and the effective aperture diameter  $D'$  assessed from the half-power beamwidth. It is found that  $D'$  is consistently greater than the real diameter of the sphere  $D$ , indicating the additional directivity created by the sphere volume. The efficiency loci drawn in Fig 4 relate the gain with  $D'/\lambda_0$  (where  $\lambda_0$  = free space wavelength) and losses, based upon the assumption that the aperture is uniform.

Gain limitation due to dielectric losses in the sphere was investigated using a range of PTFE spheres with diameters ranging from  $3.3 \lambda_0$  to  $5.8 \lambda_0$  placed in front of a circular waveguide aperture at 78 GHz. A gain limitation of about 19.5 dBi was found with only a 1 dB increase in gain over the range. At the same frequency the range of spheres were placed over a square microstrip patch and here the measured gains (accounting for a waveguide launcher transition loss of 2 dB) were about 2 dB lower than for the circular waveguide source, with a measured gain limit of about 16.5 dBi. The trend for smaller spheres of diameters less than  $3 \lambda_0$  was investigated at microwaves in the region of 15 GHz. In these experiments an error of

$\pm 1$  dB at millimetre wavelengths and  $\pm 0.5$  dB at microwaves was assessed.

Our present calculations indicate that the loss due to the dielectric material alone ranges from -0.88 dB to -0.11 dB for sphere diameters of respectively 2 and 1 mm. This is indeed a small effect which implies that the gain limitations evident in Fig 4 are due to the departure of the aperture fields from a uniform distribution. The gain limitation is not apparent for the smaller spheres in Fig 4 and waveguide excitation of the larger spheres gives a consistently higher gain than microstrip patch excitation at millimetres. These effects are currently being studied but the inference at present is that there is no point making the dielectric spheres too large.

The improvement in the radiation patterns of an array due to an overlay of dielectric spheres is well illustrated in Figs 5 and 6. The E and H-plane patterns of a 2x2 square array of 4 microstrip patches are shown in Figs 5a and 5b respectively. The measurement frequency was 13.42 GHz and the sidelobe level in the E-plane is characteristic of microstrip patches for an element separation of  $d = 0.99 \lambda_0$ . When loaded with a dielectric sphere of diameter  $D = 0.99 \lambda_0$  ( $r = 2.3$  and  $\tan \delta = 0.001$ ), a detuning of 0.75% from 13.42 GHz to 13.32 GHz resulted, together with an increase of 1.4 dB in the measured gain. Significantly lower sidelobe levels were noticed in both planes and lower cross-polar radiation was measured in the H-plane. Agreement between the theoretical model and measurements is good but predictions of cross-polar radiation were not made as they would have necessitated modelling the feed radiation mechanism. Inspection of the H-plane cross-polar in Figs 5(a) and 6(a) suggests that unwanted feed radiation is collimated in some way, and has less corrupting effects. Another important property of the overlay is that the E and H beamwidths are equalised.

If the sphere is truncated, a reduction of the gain is obtained as shown in Fig 7, where  $h'$  is the truncated height of the sphere. In these measurements the original sphere diameter was 12.7 mm, with  $r_p = 2.3$  and  $\tan \delta = 0.001$ . The gain of the single sphere/patch combination was about 16.4 dB for the truncated sphere at 13 GHz. The measured gains are lower than those predicted but both follow the same trend of decreasing gain with reducing  $h'$ . Beamwidth also increased with reducing  $h'$  and this is well predicted by theory.

In the case of the 2x2 array, previously discussed, the increase in gain with 0.99  $\lambda_0$  diameter spheres was large because of the increased directivity imparted to the array by the spheres. For much larger arrays using similarly sized spheres the increase in directivity would be less but one would still expect useful increases in gain. This was demonstrated at 90 GHz by constructing a large 256 element, uniform parallel-fed patch array with an inter-element spacing equal to the sphere diameter, of 0.95  $\lambda_0$ . The measured gain increased from 24 to 27 dB and the radiation pattern quality was improved in both E and H-planes. The H-plane sidelobes decreased from -12 dB and -15 dB to -14 dB and -15 dB while the E-plane sidelobes improved from -10.0 dB and -10.5 dB to -13.0 dB and -10.0 dB on

application of the spheres. Boresight cross-polar radiation was at -10 dB in both cases with the cross-polar lobe in the H-plane due to feed radiation being reduced by 1 dB to -16 dB. The beamwidth in both planes was 2 degrees; see Fig 8.

#### CONCLUSIONS

The placing of dielectric spheres in contact with a microstrip patch antenna uses their lens behaviour to bring about increased gain, lower sidelobes and lower cross-polar radiation despite the proximity of the patch near fields. Present analytical results are accurate enough to model the improvement in pattern quality but the feed contribution to cross-polarisation is more difficult to account for.

Loss due to the dielectric material does not seem a problem but further investigation is currently underway. The new antenna configuration has many interesting applications at both microwaves and millimetre wavelengths where a small increase in depth is not a problem. However, by moulding the overlay of spheres as one piece, a combined lens system and weather shield could be made and this would partially obviate the depth problem.

#### ACKNOWLEDGEMENTS

This research was partially funded by the US Army, European Research Office, London and SERC, UK.

#### REFERENCES

1. James, J.R., Henderson, A., Hall, C.M. and Andrasic, G., 1984, "Conformal planar millimetre arrays - A systems appraisal", *Proc Military Microwaves Conf*, 518-521.
2. James, J.R., John, G. and Hall, C.M., 1984, *Proc IEE Pt-H*, 131, 341-350.
3. James, J.R. and Henderson, A., 1985, "Millimetre components and techniques, Part IV. Planar millimetre-wave antenna arrays", Academic Press, New York, USA, (to be published).
4. Crosswell, W.F., Chatterjee, J.S., Mason, V.B. and Tai, C.T., 1974, "Aperture excited dielectric antennas", NASA Tech Note, TN D-7342.
5. Narasimhan, M.S. and Ravishankar, S., 1982, *IEEE Trans. Antennas and Propag*, 30, 1237-1240.
6. Chatterjee, R., 1973, *Jour. Indian Inst. of Science*, 55, 16-31.
7. James, J.R., Hall, P.S. and Wood, C., 1981, "Microstrip antenna theory and design", Peter Perigrinus Ltd, London, England.



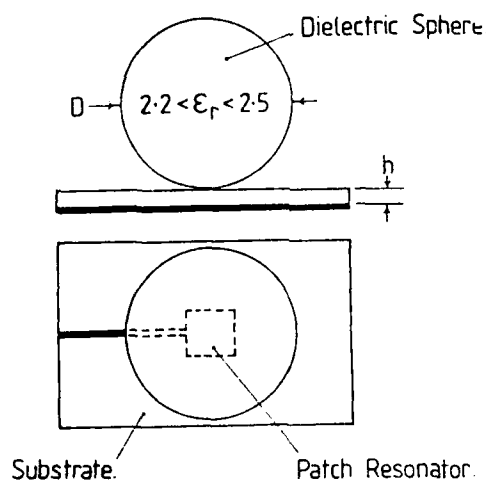
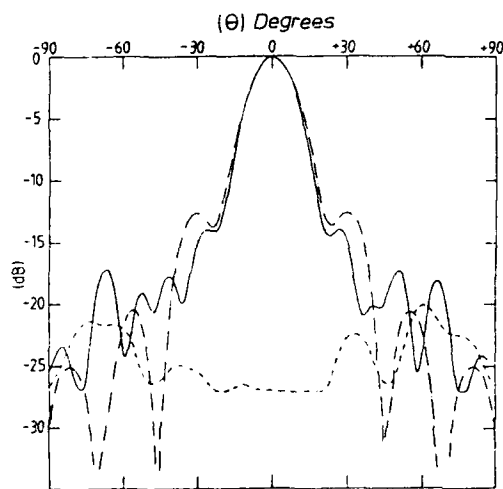


Figure 1 Sketch showing the position of a dielectric sphere overlaid upon a microstrip patch antenna.



$D = 50.0\text{mm}$ ,  $\epsilon_r = 2.3$ ,  $f = 15.4\text{GHz}$ .

— Co-polar (measured)  
 --- Co-polar (theory)  
 ..... Cross-polar (measured)

Figure 3 H-plane radiation pattern of a patch element with a dielectric sphere overlay.

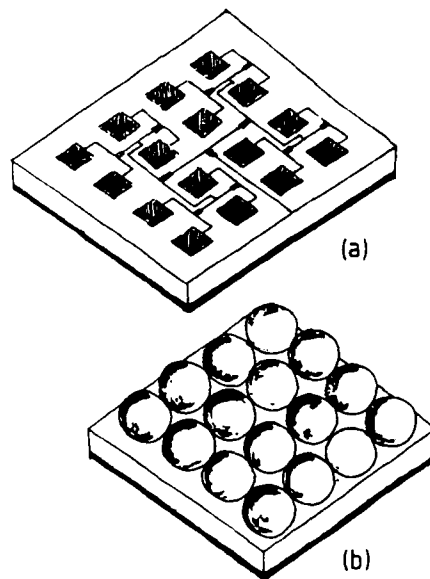
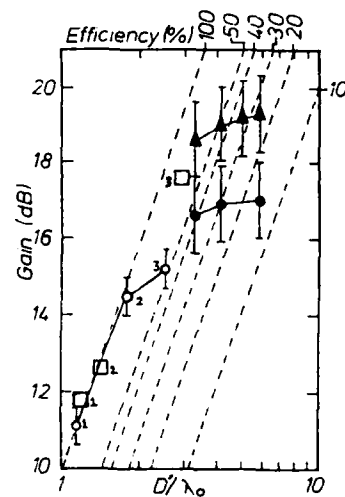


Figure 2 Sketch of microstrip patch arrays, (a) without overlay and (b) with overlay.



▲ PTFE spheres over  $TE_{11}$  circular aperture : 78 GHz.  
 ● PTFE spheres over microstrip patch : 78GHz.  
 ○ PTFE spheres over microstrip patch,  
 1  $D = 22.23\text{mm}$ ,  $\tan\delta = 0.001$ ,  $\epsilon_r = 2.3$ ,  $f = 15.6\text{GHz}$ .  
 2  $D = 25.0\text{mm}$ ,  $\tan\delta = 0.0003$ ,  $\epsilon_r = 2.2$ ,  $f = 15.5\text{GHz}$ .  
 3  $D = 50.0\text{mm}$ ,  $\tan\delta = 0.0003$ ,  $\epsilon_r = 2.2$ ,  $f = 15.4\text{GHz}$ .  
 □ Theory for corresponding numbers.

Figure 4 Gain of patch element with a dielectric sphere overlay plotted against the effective aperture diameter  $D'$  for various efficiencies.

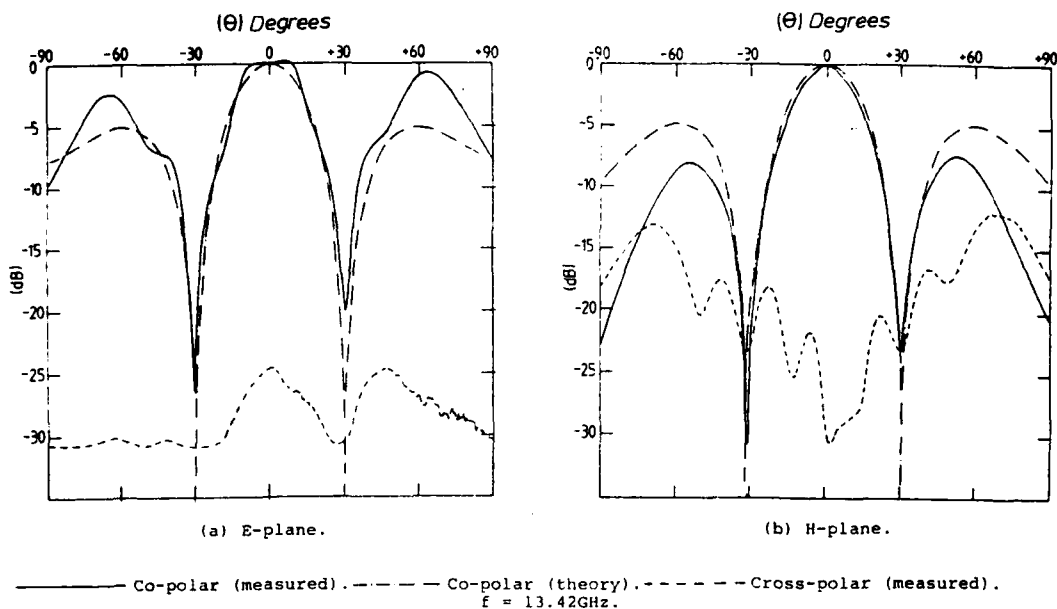


Figure 5 Radiation patterns of four patch elements in a  $2 \times 2$  square array.

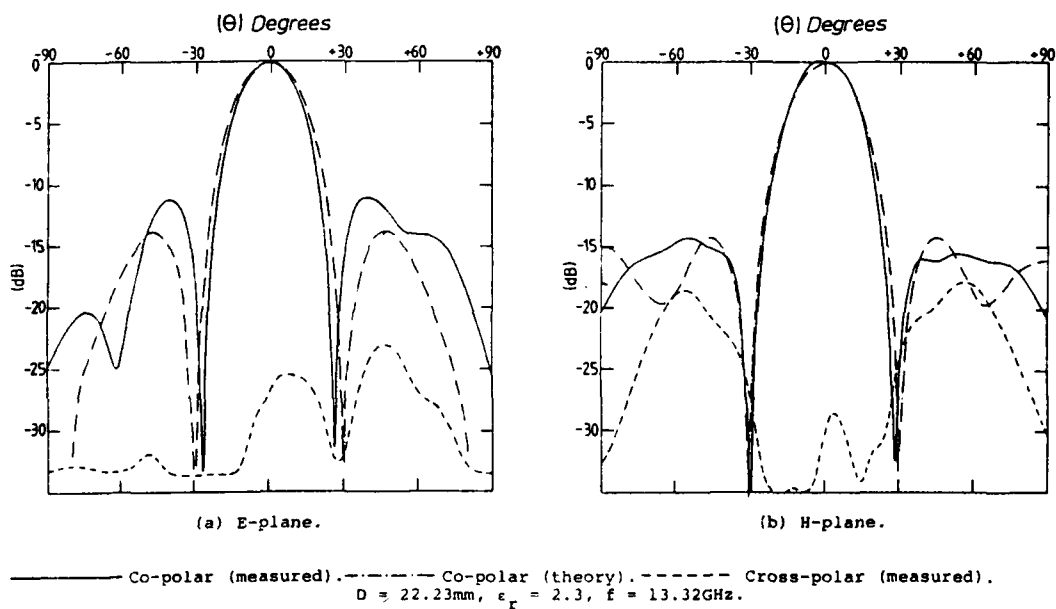


Figure 6 Radiation patterns of four patch elements in a  $2 \times 2$  square array with overlaid dielectric spheres.

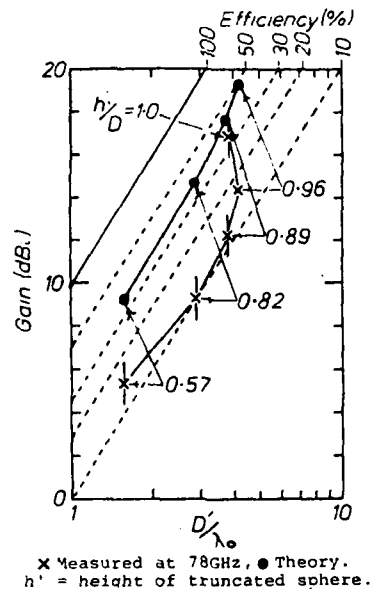


Figure 7 Gain of patch element with truncated dielectric sphere overlay plotted against effective aperture  $D'$ , for various efficiencies.

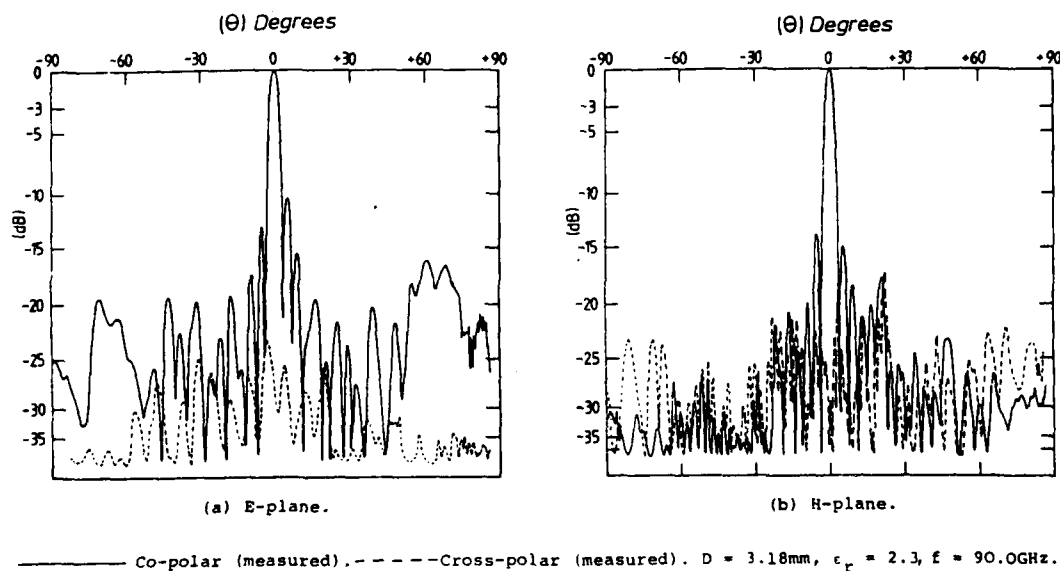


Figure 8 Radiation patterns of a 256 (16x16) element square patch array with overlaid dielectric spheres.

For E/D ring oscillators, the gate delay showed a strong dependence on drain bias. The minimum gate delay time was 41 ps/gate with a 4.1 mW/gate power dissipation. In addition, a very low speed-power product of 12.5 fJ was obtained at  $V_{DD} = 1.0$  V, which corresponds to a minimum power dissipation of 0.24 mW/gate with a 53 ps/gate delay time.

**Conclusions:** A newly developed DDS process has been successfully implemented on 3 in GaAs wafers to fabricate self-aligned MESFET circuits. In comparing the DDS process with other previously reported processes with similar device structures, the DDS process is less complicated and appears more manufacturable. The reported transconductance value of 280 mS/mm is the highest value ever published for 1  $\mu$ m-gate enhancement-mode GaAs MESFETs.<sup>1-5</sup> The ring oscillator performance and yield results show the potential of the DDS process to achieve a wide range of performance characteristics of high speed, 22 ps/gate with 1.5 mW/gate and very low power, 0.37 mW/gate with 12.5 fJ power-speed product.

**Acknowledgments:** The authors would like to thank all members of the GaAs Integrated Circuit Fabrication and Engineering Groups for their support.

M. F. CHANG  
F. J. RYAN  
R. P. VAHRENKAMP  
C. G. KIRKPATRICK

Rockwell International Corporation  
Microelectronics Research & Development Center  
Thousand Oaks, CA 91360, USA

26th February 1985

#### References

1. YAMASAKI, K., ASAI, K., MIZUTANI, T., and KURUMADA, K.: 'Self-align implantation for  $n^+$ -layer technology (SAINT) for high-speed GaAs ICs', *Electron. Lett.*, 1982, 18, pp. 119-121
2. YAMASAKI, K., YAMANE, Y., and KURUMADA, K.: 'Below 20 ps/gate operation with GaAs SAINT FETs at room temperature', *ibid.*, 1982, 18, pp. 592-593
3. ONODERA, H., YOKOYAMA, N., KAWATA, H., NISHI, H., and SHIBATANI, A.: 'High-transconductance self-aligned GaAs MESFET using implantation through an AlN layer', *ibid.*, 1984, 20, pp. 45-47
4. YOKOYAMA, N., OHNISHI, T., ONODERA, H., SHINOKI, T., SHIBATANI, A., and ISHIKAWA, H.: 'A GaAs 1K static RAM using tungsten-silicide gate self-alignment technology', *ISSCC, Digest of Technical Papers*, 1983, pp. 44-45
5. LEVY, H. and LEE, R. E.: 'Self-aligned submicron gate digital GaAs integrated circuits', *IEEE Electron Device Lett.*, 1983, EDL-4, pp. 102-104

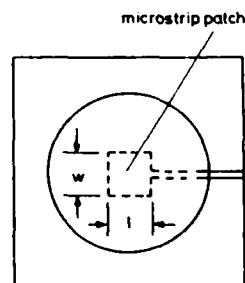
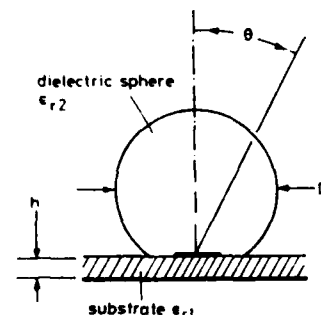
## MICROSTRIP PLANAR ARRAYS WITH DIELECTRIC SPHERE OVERLAYS

*Indexing terms: Antennas, Antenna arrays, Microstrip*

A novel combination of a microstrip patch and dielectric sphere is described. Measurements and analysis illustrate the basic action and the use of this new element in a millimetre-wave array. Improved radiation pattern control and sparse deployment of elements, at a cost of some increase in antenna depth and constructional detail, are the main features identified.

**Introduction:** The use of dielectric feeders with microstrip patch elements, as a means of reducing feeder losses, has been recently investigated.<sup>1</sup> In this letter we report other ways of advantageously combining dielectric and microstrip structures, and the action of a dielectric sphere excited by a rectangular microstrip patch is described. When arrays of this new element are deployed, improved radiation pattern control and provision of additional space for circuit elements are some of the benefits obtained, at a cost of some increased depth and constructional detail. In the practical arrangement the spheres

are slightly flattened so that no airspace exists between the sphere and patch (Fig. 1). The patch can be fed with a backed probe or coplanar line as sketched in Fig. 1.



03571

Fig. 1 Diagram of microstrip patch/dielectric sphere radiating element

**Theory:** The excitation of dielectric spheres by waveguides<sup>2</sup> and the probe excitation of a dielectric hemisphere<sup>3</sup> have previously been addressed. In the present case the near fields of the patch can be a significant factor in the excitation process and are modelled approximately as dipole line sources at the patch extremities. The fields on the sphere surface are then transformed into equivalent fictitious sources from which the far-field radiation pattern is readily obtained. This analysis in its present form is useful to predict the copolar patterns but is incomplete as regards the inclusion of crosspolar contributions that can arise from the patch feeder system. Dielectric losses are allowed for, thus enabling gain calculations to be made. Arrays of the sphere/patch elements are calculated by compounding the array and element factors.

**Measured and calculated results:** Fig. 2 shows the H-plane radiation pattern of a square microstrip patch with and without an overlaid dielectric sphere of relative permittivity  $\epsilon_{r2} = 2.2$  and  $D = 50$  mm. When the sphere was brought into contact with a square patch of  $w = l = 5.95$  mm, the resonant frequency of the input impedance was reduced from 15.64 GHz to 15.37 GHz. The microstrip substrate had a relative permittivity  $\epsilon_{r1} = 2.3$  and thickness  $h = 0.79$  mm. The measured gain and calculated gain corrected for losses in the dielectric material are given in Table 1, together with data for a smaller sphere. The difference between the theoretical and measured gains increases with sphere size and is mainly due to the accuracy of the theoretical model. Experiments on a range

Table 1 MEASURED AND CALCULATED GAINS OF PATCH/SPHERE ELEMENTS

Material		D	Freq.	Measured gain	Calculated gain
$\epsilon_{r2}$	$\tan \delta$	mm	GHz	dBi	dBi
2.2	0.001	22.2	15.6	11.1	11.7
2.2	0.0003	50.0	15.37	15.2	17.5

of different size spheres indicated that increasing the sphere diameter beyond about  $D = 3\lambda_0$  ( $\lambda_0$  = free-space wavelength) yields little increase in gain. This is attributed to the inability of the patch to create an optimal field distribution. Shaping of the spherical surface and using different shapes of patch resonators are some of the many variations that offer additional pattern control. Truncation of the sphere to increase the area in contact with the substrate has also been investigated.<sup>4</sup> In general the presence of the sphere brings about improved equality of *E* and *H* beamshapes, a reduction of sidelobes and some reduction in crosspolarisation levels.

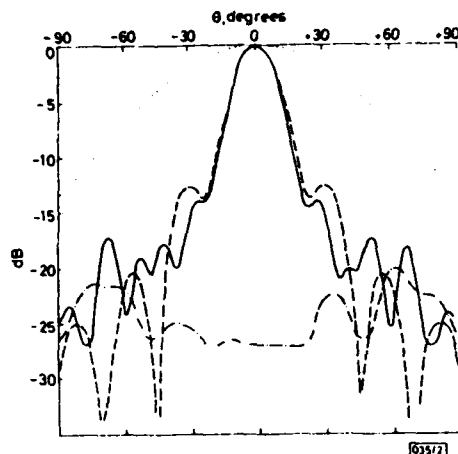


Fig. 2 H-plane radiation pattern of a microstrip patch element with an overlaid dielectric sphere

$D = 50.0$  mm,  $\epsilon_r = 2.2$ ,  $\tan \delta = 0.0003$ ,  $\epsilon_1 = 2.3$ ,  $h = 0.79$  mm,  $f = 15.37$  GHz

— copolar (measured)  
--- copolar (theory)  
- - - crosspolar (measured)  
..... theoretical copolar pattern of microstrip patch without overlaid sphere

The use of spheres to effect pattern control is most marked when considering arrays of these elements as in Fig. 3. Without the spheres the patch spacing  $d$  was made too great for conventional array operation and hence the pattern was dominated by grating lobes. With the spheres in place a well structured beam with sidelobes commensurate with a uniform array distribution was achieved which is in very good agreement with theory. Crosspolarisation levels were lower than

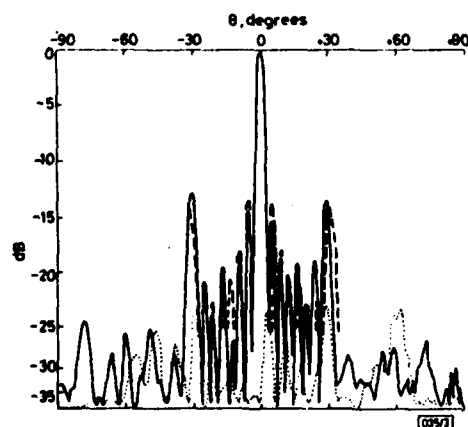


Fig. 3 E-plane radiation pattern of a 64-element patch array at 90 GHz:  $d = D = 1.9\lambda_0$ ,  $\epsilon_r = 2.2-2.5$ ,  $\tan \delta = 0.001$ ,  $\epsilon_1 = 2.3$ ,  $h = 0.127$  mm,  $f = 90.0$  GHz

— copolar (measured)  
--- copolar (theory)  
- - - crosspolar (measured)

those usually obtained from microstrip arrays, where feed radiation is a problem. Further details on this array and another version with closer patch spacing are summarised in Table 2 and further illustrate the properties of the new element.

Table 2 SUMMARY OF MILLIMETRIC ARRAY RADIATION PATTERN MEASUREMENTS AT 90 GHz

	256 elements		64 elements	
	Without spheres	With spheres	Without spheres	With spheres
$d/\lambda_0 = D/\lambda_0$	0.95	0.95	1.90	1.90
Gain, dBi	24	27	14	26
<b>E-plane</b>				
Sidelobes, dB	-10, -10.5	-13, -10	-11, -12	-14, -15
Grating lobes, dB	—	—	0, 0	-12.5, -13
Spurious, dB	< -11.5	< -17	< -18	< -23
Crosspolar, dB	< -25	< -23	< -15	< -24
<b>H-plane</b>				
Sidelobes, dB	-12, -15	-14, -15	-12, -12	-12.5, -13.5
Grating lobes, dB	—	—	-1, -1.5	-15, -14.5
Spurious, dB	< -20	< -17	< -17	< -20
Crosspolar, dB	< -15	< -16	< -12.5	< -20

**Conclusions:** A new type of array element consisting of a dielectric sphere excited by a microstrip patch has been described. The new structure offers additional degrees of freedom in pattern control at the expense of increased depth and constructional detail. Many variations in patch and sphere geometry are suggested offering improved pattern control, and we are currently developing a circularly polarised feed for a reflector antenna with switched beams, using these principles. When applied to arrays, fewer elements are required which leads to an immediate reduction in co- and crosspolarised radiation from feeder networks. The sparse feed network also makes additional space available for circuit elements such as phase shifters.

These issues are particularly advantageous at millimetres<sup>3</sup> where the provision for electronic beam scanning circuits is a requirement. Calculations indicate that with smaller spheres some beam scanning facilities could be incorporated. Finally the physical deployment of the dielectric spheres on the substrate can be approached by moulding the spheres as a matrix which after fixing to the array beneath with adhesive would also form a protective dielectric panel. This would be particularly attractive at millimetre wavelengths.

**Acknowledgments:** This work was supported by the United States Army and Air Force through the European Research Office, London, and by the UK Science & Engineering Research Council.

C. M. HALL  
G. ANDRASIC  
J. R. JAMES

19th February 1985

School of Electrical Engineering & Science  
Royal Military College of Science  
Shrivenham, Swindon, Wilts. SN6 8LA, United Kingdom

#### References

- JAMES, J. R., JOHN, G., and HALL, C. M.: 'Millimetre-wave hybrid dielectric-microstrip antenna array', *IEE Proc. H, Microwaves, Opt & Antennas*, 1984, 131, pp. 341-350
- CROSSWELL, W. F., CHATTERJEE, J. S., MASON, V. B., and TAL, C. T.: 'Aperture excited dielectric antennas', NASA tech. note, 1974, TN D-7342
- MCALLISTER, M. W., and LONG, S. A.: 'Resonant hemispherical dielectric antenna', *Electron. Lett.*, 1984, 20, pp. 657-659
- HALL, C. M., JAMES, J. R., and ANDRASIC, G.: 'Microstrip patch arrays with spherical dielectric overlays', *Proc. int. conf. on antennas and propagation*, Warwick University, UK, 16-19 April 1985 (to be published)
- MAITTIK, R. J.: 'Phased array theory and technology', *Proc. IEEE*, 1982, 70, pp. 246-291

## DIELECTRIC SPHERE REFLECTOR FEED WITH MICROSTRIP EXCITATION

J.R. James, C.M. Hall, P.S. Hall and C.J. Prior

School of Electrical Engineering and Science  
Royal Military College of Science  
Shrivenham, Swindon, Wilts, SN6-8LA, England

### INTRODUCTION

The application of a spherical dielectric lens in direct contact with a single microstrip patch radiating element Fig.1, creates a new type of antenna element with a greater degree of design freedom than a conventional microstrip patch array. The technique has already been applied to arrays of microstrip patches where the sparse deployment of radiating elements and a consequent reduction in feed radiation has been achieved<sup>1</sup>.

In this present paper we consider how this technique may be applied to the design of a new type of reflector antenna feed offering continuous design control of beamwidth in applications where the beamwidth of a patch alone would be too broad and an array of patches would have too narrow a beamwidth.

The following discussion covers the choice of lens diameter  $D$ , truncated height,  $h'$ , (both of which control the beamwidth) substrate dielectric constant,  $\epsilon_r$ , and thickness,  $h$ , in the design of a feed antenna for a parabolic reflector. For illustrative purposes we consider the following requirement: diameter of reflector=1.0m and focal length=0.588m, operating within the following basic specification, (1) Frequency band, 11.7 to 12.5GHz, (2) Gain >35.5 dBi, (3) Sidelobes better than for uniform distribution and (4) Cross-Polarisation <-25dB (including circular polarisation).

### CHOICE OF SUBSTRATE AND LENS

During measurements of the radiation patterns of a TM<sub>11</sub> circular disc antenna on a substrate of height  $h=1.59\text{mm}$  it was found that the maximum H-plane Cross-Polar ( $\text{HCP}_{\text{max}}$ ) was much greater than in the E-plane<sup>2</sup>, within  $\theta=\pm 50^\circ$ . In this case  $\text{HCP}_{\text{max}}$  was measured at -14.5 dB, see Fig.2. Further investigation showed  $\text{HCP}_{\text{max}}$  to be a function of both  $h$  and  $\epsilon_r$ , and indicated that  $\text{HCP}_{\text{max}}$  must be traded against bandwidth with  $\text{HCP}_{\text{max}}$  being a stronger function of  $\epsilon_r$ ; see Fig.3. A substrate height of  $0.79\text{mm}$  and  $\epsilon_r=2.3$  was chosen resulting in a bandwidth ( $\text{VSWR}<2.6$ ) of 5.9% and  $\text{HCP}_{\text{max}}=-18\text{dB}$ .

A commercially available PTFE sphere of  $\epsilon_r=2.2-2.5$  and diameter 22.2mm was chosen but required truncation to meet the required beamwidth of about 100 degrees in both principal planes. The second reason for choosing a substrate of height  $h/\lambda_0=0.033$  and  $\text{HCP}_{\text{max}}=-18\text{dB}$  was that  $\text{HCP}_{\text{max}}$  increased to -15dB when the untruncated sphere ( $h=0$ ) was placed in contact with the patch. For  $h/\lambda_0=0.060$ ,  $\text{HCP}_{\text{max}}$  increased to -11.3dB. Other effects of the sphere were a small detuning of 1%, and an increase in bandwidth ( $\text{VSWR}<2.6$ ) from 5.9% to 6.4%.

## RESULTS WITH OVERLAID TRUNCATED SPHERE

Truncation of the sphere to a height  $h/D=0.92$  resulted in an increase in the H- and E-plane beamwidths to  $96.5^\circ$  and  $88.0^\circ$  respectively. Additionally, there was a larger detuning of 5.3% to the centre frequency of 11.98GHz, and a further increase in bandwidth to 6.7%.

The radiation patterns of the chosen feed antenna were measured both in amplitude and phase; see Figs.4(a and b), about the phase centre of the antenna, (see Fig.1), which was chosen as the point about which the Co-polar phase deviation is a minimum in both principal planes between  $\theta=\pm 50^\circ$ , and was measured at  $z=+7\text{mm}$  from the groundplane. Amplitude measurements showed little change in  $\text{HCP}_{\text{max}}$  at -15.2dB and a reduction in  $\text{ECP}_{\text{max}}$  to -25dB. However both  $\text{ECP}_{\text{max}}$  and, more importantly,  $\text{HCP}_{\text{max}}$  are functions of frequency with  $\text{HCP}_{\text{max}}$  rising towards the band edges. Variations, of  $\text{HCP}_{\text{max}}$  may emerge as an important factor in an evaluation of bandwidth.

## PREDICTIONS FOR REFLECTOR ANTENNA

The radiation patterns of the complete reflector antenna were calculated using the physical optics approximation with the measured feed data. Figures 5(a) and 5(b) show the H- and E-plane radiation patterns for linear polarisation and are summarized in Table 1.

Calculations of the performance of reflector antenna considered with a circularly polarised feed assumed that two identical orthogonal modes are excited in the feed and are appropriately phased, each having identical characteristics to the linearly polarised antenna.

The calculated aperture efficiency includes spillover loss, aperture taper loss and feed losses.

## CONCLUSIONS

It has been shown that a spherical (or truncated spherical) dielectric lens placed in contact with a microstrip patch allows an efficient reflector feed to be made offering continuous design control of beamwidth. The control of H-plane cross-polarised radiation has emerged as an important issue, the variation of which could prove to be an important bandwidth criteria.

Other possibilities under development include the use of multiple patches for switched or simultaneous beams and the use of specially shaped non-spherical lenses.

## ACKNOWLEDGEMENTS

This work was supported by the United States Army and Air Force through the European Research Office, London and by the United Kingdom Science and Engineering Research Council.

## REFERENCES

1. HALL, C.M., JAMES, J.R. and ANDRASIC, G.: "Microstrip patch arrays with spherical dielectric overlays", Proc. Int. Conf. on Antennas and Propag., Warwick Univ., U.K., 16-19 April 1985. (To be published).
2. HUANG, J.: "The finite groundplane effect on the microstrip antenna radiation patterns", IEE Trans., Vol. AP-31, No.4, July 1983, pp.649-655.

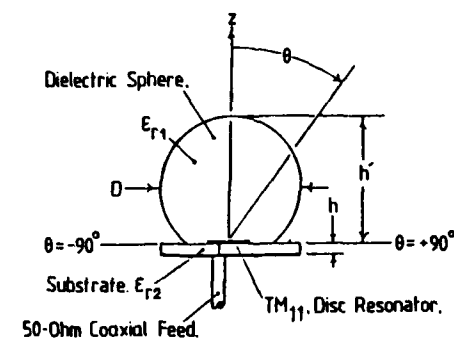
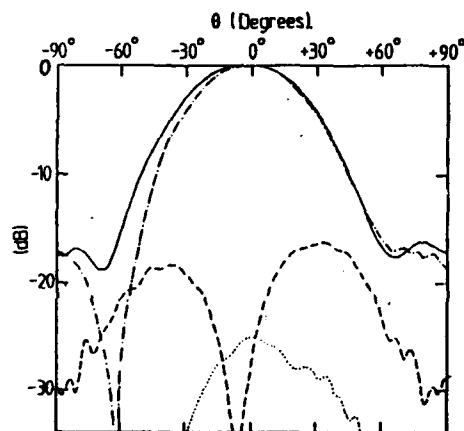
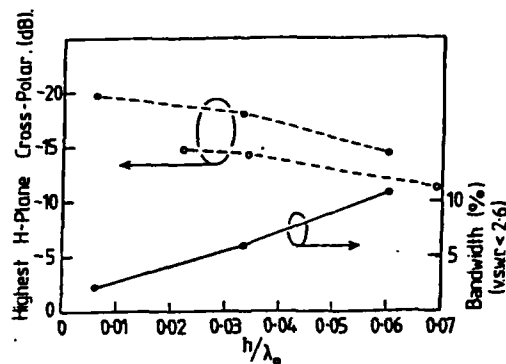


Fig 1: Diagram of feed antenna with truncated sphere.



4(a)

4(b)

Fig 4: Radiation patterns of reflector feed antenna with a truncated spherical lens. (a) Amplitude, (b) Phase.  
 $\epsilon_{r2}=2.3$ ,  $h=0.79\text{mm}$ ,  $f=11.98\text{GHz}$ ,  $h/\lambda_0=0.032$ ,  $\epsilon_{r1}=2.2-2.5$ ,  $D=22.23\text{mm}$ ,  $h'/D=0.92$   
 Phase centre at  $Z=+7\text{mm}$ , Measured gain  $10.8\text{dBi}$ .  
 — H-plane Co-polar      - - - E-plane Co-polar  
 - - - H-plane Cross-polar      ..... E-plane Cross-polar

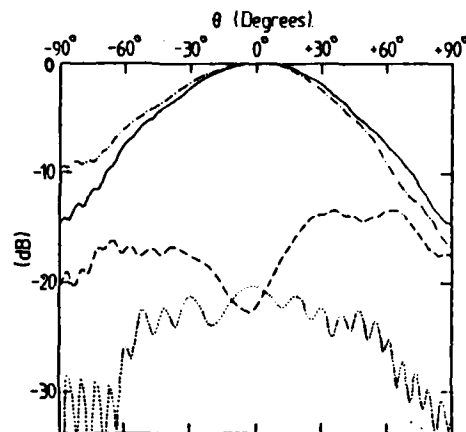
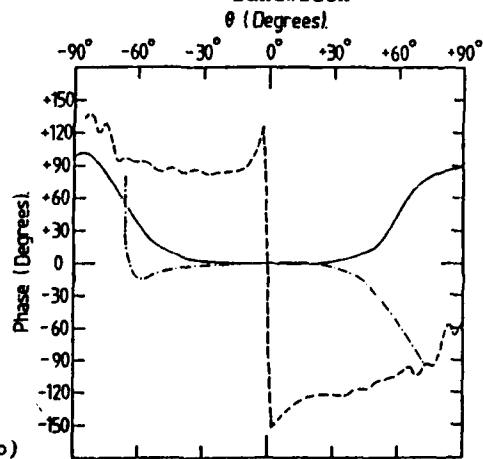


Fig 2: Radiation pattern of a  $TM_{11}$  circular disc element,  $f=11.90\text{GHz}$ ,  $h/\lambda_0=0.06$ .

— H-plane Co-polar  
 - - - H-plane Cross-polar  
 - . - . E-plane Co-polar  
 ..... E-plane Cross-polar

Fig 3: Variation of Maximum H-plane Cross-polar level and bandwidth with  $h/\lambda_0$ .

•  $\epsilon_{r2}=2.3$ , •  $\epsilon_{r2}=1.0$   
 - - - Maximum H-plane Cross-polar  
 — Bandwidth





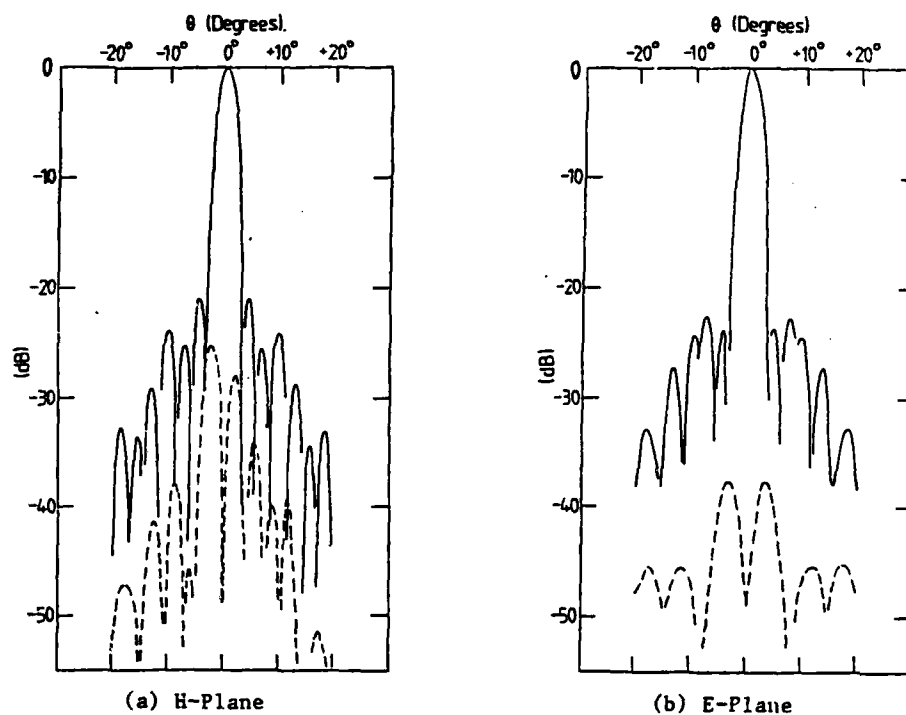


Fig 5: Predicted radiation patterns from reflector antenna.  
Frequency 11.98GHz, Dish diameter 1.0m, Focal length 0.588m.

———— Co-polar      - - - - - Cross-polar.

	Linear Polarisation		Circular Polarisation	
	H-plane	E-plane	H-plane	E-plane
Sidelobes (dB)	<-21	<-22.5	<-25.2	<-25.7
Highest Cross-Polar (dB)	<-25.3	<-37.5	<-27.3	<-24.8
Boresight Cross-Polar (dB)	-49.1	-49.1	-77.9	-77.9

Aperture efficiency 66%, Gain 40.2 dBi: for linear polarisation.  
Beamwidth (-3dB) 2.5°

Table 1: Summary of predicted reflector radiation patterns.

**END**

**FILMED**

**10-85**

**DTIC**